

---

Theses and Dissertations

---

Summer 2010

# Microscopic dynamics in two-dimensional strongly-coupled dusty plasmas

Yan Feng

*University of Iowa*

Copyright 2010 Yan Feng

This dissertation is available at Iowa Research Online: <http://ir.uiowa.edu/etd/665>

---

## Recommended Citation

Feng, Yan. "Microscopic dynamics in two-dimensional strongly-coupled dusty plasmas." PhD (Doctor of Philosophy) thesis, University of Iowa, 2010.  
<http://ir.uiowa.edu/etd/665>.

---

Follow this and additional works at: <http://ir.uiowa.edu/etd>



Part of the [Physics Commons](#)

MICROSCOPIC DYNAMICS IN TWO-DIMENSIONAL  
STRONGLY-COUPLED DUSTY PLASMAS

by

Yan Feng

An Abstract

Of a thesis submitted in partial fulfillment of the  
requirements for the Doctor of Philosophy  
degree in Physics in the  
Graduate College of The  
University of Iowa

July 2010

Thesis Supervisor: Professor John Goree

## ABSTRACT

A strongly-coupled plasma is a collection of free charged particles that interact with a Coulomb repulsion that is so strong that nearby particles do not easily move past one another. Unlike weakly-coupled plasmas, strongly-coupled plasmas exhibit a self-organization of particles into an arrangement like a solid crystalline lattice or a liquid.

Dusty plasmas consist of micron-size particles of solid matter that are immersed in a plasma of electrons and ions. The dust particles gain a large electric charge and become strongly coupled. The motion of discrete particles can be tracked using a video microscopy diagnostic. Dusty plasma experiments allow a study of strongly-coupled plasma physics and an experimental simulation of condensed matter physics. Experiments are reported using a single layer of particles in the plasma to study two-dimensional (2D) physics.

It is demonstrated experimentally that in addition to the solid and liquid states, a strongly-coupled dusty plasma can exist in an exotic state called a superheated solid. A 2D dusty plasma, initially self-organized in a crystalline lattice, is heated rapidly by rastered laser beams. The suspension remains in a solid lattice at a temperature well above the melting point.

Shear-induced melting is studied in a 2D dusty plasma by applying shear to a crystalline lattice using a pair of oppositely-directed laser beams. Unexpectedly, coherent longitudinal waves are also excited in the resulting shear flow. In the first experiment of its kind, a suddenly-applied shear is found to produce a melting front that spreads at the transverse sound speed.

The viscoelasticity of strongly-coupled plasmas in a liquid state is quantified. In the first experiment for any kind of physical system, the wavenumber-dependent

viscosity,  $\eta(k)$ , is computed from measurements of the random motion of particles. It is found that  $\eta(k)$  diminishes with increasing  $k$ , indicating that viscous behavior is gradually replaced by elastic behavior as the scale length is reduced.

As a tool for studying transport at a microscopic level, the self-intermediate scattering function (self-ISF) is used in numerical simulations of 2D dusty plasmas. Two physical processes are studied using the self-ISF: relaxation of random motion, and melting. The wavenumber-dependence of the relaxation time in a liquid-phase strongly-coupled plasma is shown to be useful for distinguishing normal and anomalous diffusion. The self-ISF is also demonstrated to be a sensitive indicator of the melting transition.

An improved image-analysis method is developed for calculating particle positions with minimal measurement errors. This development also provides an understanding of sources of error and the dependence on parameters that the experimenter can control.

Abstract Approved: \_\_\_\_\_  
Thesis Supervisor

\_\_\_\_\_  
Title and Department

\_\_\_\_\_  
Date

MICROSCOPIC DYNAMICS IN TWO-DIMENSIONAL  
STRONGLY-COUPLED DUSTY PLASMAS

by

Yan Feng

A thesis submitted in partial fulfillment of the  
requirements for the Doctor of Philosophy  
degree in Physics in the  
Graduate College of The  
University of Iowa

July 2010

Thesis Supervisor: Professor John Goree

Copyright by  
YAN FENG  
2010  
All Rights Reserved

Graduate College  
The University of Iowa  
Iowa City, Iowa

CERTIFICATE OF APPROVAL

---

PH.D. THESIS

---

This is to certify that the Ph.D. thesis of

Yan Feng

has been approved by the Examining Committee  
for the thesis requirement for the Doctor of  
Philosophy degree in Physics at the July 2010  
graduation.

Thesis Committee: \_\_\_\_\_  
John A. Goree, Thesis Supervisor

\_\_\_\_\_  
Christoph Beckermann

\_\_\_\_\_  
Robert L. Merlino

\_\_\_\_\_  
Frederick N. Skiff

\_\_\_\_\_  
Gregory G. Howes

To my parents and my wife

## ACKNOWLEDGMENTS

In the first place, I would like to give my special thanks to my advisor Prof. J. Goree for his supervision, advice, guidance and long-lasting financial support. He was patient in teaching me everything in our lab: designing apparatus, performing experiments, writing codes, writing proposals, giving seminar talks, and writing papers. All of these enriched my growth from a student to a researcher. I am very grateful for the freedom he gave me in choosing research topics.

I also gratefully acknowledge Dr. B. Liu for his plentiful advice and suggestions, and allowing me to adapt his particle simulation code. I would like to thank him for discussions about not only my thesis projects but also many other technical concepts.

I would like to thank Prof. R. Merlino, Prof. F. Skiff, Prof. S. Spangler, Prof. G. Howes for their comments and helpful discussions during my seminar talks.

I thank Dr. V. Nosenko for teaching me data analysis methods during my first few months in the lab. I also thank my lab mate Mr. T. Flanagan for not only sharing codes but also his cooperation in the maintenance, repair, and operation of our equipment.

I also thank Dr. U. Konopka and Dr. O. Arp for allowing me to test their data analysis codes.

I thank my committee members for their comments and the time they devoted to this thesis and my comprehensive exam.

## ABSTRACT

A strongly-coupled plasma is a collection of free charged particles that interact with a Coulomb repulsion that is so strong that nearby particles do not easily move past one another. Unlike weakly-coupled plasmas, strongly-coupled plasmas exhibit a self-organization of particles into an arrangement like a solid crystalline lattice or a liquid.

Dusty plasmas consist of micron-size particles of solid matter that are immersed in a plasma of electrons and ions. The dust particles gain a large electric charge and become strongly coupled. The motion of discrete particles can be tracked using a video microscopy diagnostic. Dusty plasma experiments allow a study of strongly-coupled plasma physics and an experimental simulation of condensed matter physics. Experiments are reported using a single layer of particles in the plasma to study two-dimensional (2D) physics.

It is demonstrated experimentally that in addition to the solid and liquid states, a strongly-coupled dusty plasma can exist in an exotic state called a superheated solid. A 2D dusty plasma, initially self-organized in a crystalline lattice, is heated rapidly by rastered laser beams. The suspension remains in a solid lattice at a temperature well above the melting point.

Shear-induced melting is studied in a 2D dusty plasma by applying shear to a crystalline lattice using a pair of oppositely-directed laser beams. Unexpectedly, coherent longitudinal waves are also excited in the resulting shear flow. In the first experiment of its kind, a suddenly-applied shear is found to produce a melting front that spreads at the transverse sound speed.

The viscoelasticity of strongly-coupled plasmas in a liquid state is quantified. In the first experiment for any kind of physical system, the wavenumber-dependent

viscosity,  $\eta(k)$ , is computed from measurements of the random motion of particles. It is found that  $\eta(k)$  diminishes with increasing  $k$ , indicating that viscous behavior is gradually replaced by elastic behavior as the scale length is reduced.

As a tool for studying transport at a microscopic level, the self-intermediate scattering function (self-ISF) is used in numerical simulations of 2D dusty plasmas. Two physical processes are studied using the self-ISF: relaxation of random motion, and melting. The wavenumber-dependence of the relaxation time in a liquid-phase strongly-coupled plasma is shown to be useful for distinguishing normal and anomalous diffusion. The self-ISF is also demonstrated to be a sensitive indicator of the melting transition.

An improved image-analysis method is developed for calculating particle positions with minimal measurement errors. This development also provides an understanding of sources of error and the dependence on parameters that the experimenter can control.

# TABLE OF CONTENTS

LIST OF FIGURES . . . . .	ix
CHAPTER	
1 INTRODUCTION . . . . .	1
1.1 Review of dusty plasma concepts . . . . .	1
1.1.1 Dusty plasma . . . . .	1
1.1.2 Strongly-coupled plasma . . . . .	3
1.1.3 Yukawa interaction . . . . .	5
1.1.4 Forces acting on dust particles . . . . .	6
1.1.5 Two dimensionality . . . . .	7
1.1.6 Manipulation . . . . .	8
1.2 Dusty plasma as a model system . . . . .	9
1.2.1 Studying liquids and solids at an atomistic scale . . . . .	9
1.2.2 Comparison to other model systems . . . . .	10
1.3 Topics in strongly-coupled plasmas and condensed matter physics . . . . .	11
1.3.1 Solid-liquid transition and solid superheating . . . . .	11
1.3.2 Shear-induced melting . . . . .	12
1.3.3 Viscoelasticity . . . . .	12
1.3.4 Intermediate scattering function in 2D dusty plasmas . . . . .	14
1.4 Organization of this thesis . . . . .	14
2 EXPERIMENTAL SYSTEM . . . . .	16
2.1 Experimental setup . . . . .	16
2.1.1 Plasma chamber . . . . .	16
2.1.2 Dust particles . . . . .	18
2.1.3 Suspension . . . . .	18
2.1.4 Laser manipulation . . . . .	20
2.1.5 Data recording and laser illumination . . . . .	21
2.2 Data analysis method . . . . .	23
2.2.1 Particle tracking velocimetry . . . . .	23
2.2.2 Kinetic temperature . . . . .	24
2.2.3 Structural analysis . . . . .	24
2.2.4 Dynamical analysis . . . . .	26
3 SOLID SUPERHEATING IN DUSTY PLASMA . . . . .	28
3.1 Introduction . . . . .	29
3.2 Dusty plasma experiment . . . . .	30
3.3 Results . . . . .	33
3.4 Conclusion . . . . .	40

4	EVOLUTION OF SHEAR-INDUCED MELTING IN DUSTY PLASMA	41
4.1	Introduction	42
4.2	Dusty plasma	43
4.3	Experiment	44
4.4	Data analysis	45
4.5	Results	45
4.6	Conclusion	51
5	VISCOELASTICITY OF 2D LIQUIDS QUANTIFIED IN A DUSTY PLASMA EXPERIMENT	52
5.1	Introduction to viscoelasticity	53
5.2	Wavenumber-dependent viscosity	54
5.3	Dusty plasma	55
5.4	Experiment	56
5.5	Simulation	58
5.6	Results	58
5.7	Conclusion	63
6	DUSTY PLASMA RELAXATION AND MELTING STUDIED USING THE INTERMEDIATE SCATTERING FUNCTION	64
6.1	Introduction	65
6.2	Self-intermediate scattering function	67
6.3	Simulation	70
6.3.1	Parameters	70
6.3.2	Langevin MD simulations	71
6.3.3	Frictionless equilibrium MD simulations	71
6.4	Results and discussions	72
6.4.1	Relaxation and scaling	72
6.4.2	Phase transition	77
7	ACCURATE PARTICLE POSITION MEASUREMENT FROM IMAGES	85
7.1	Introduction	86
7.2	Pixel locking	89
7.3	Moment method	92
7.4	Method	93
7.4.1	Synthetic images	93
7.4.2	Errors in calculated particle positions	96
7.4.3	Parameters	97
7.5	Results	98
7.5.1	Threshold	98
7.5.2	Spot radius	101
7.5.3	Intensity	103
7.5.4	Baseline	104

7.6	Practical procedure . . . . .	109
7.7	Experimental demonstration . . . . .	110
8	CONCLUSION . . . . .	115

APPENDIX

A	DERIVATION OF WAVENUMBER-DEPENDENT VISOCOSITY $\eta(k)$ . . . . .	117
B	ERRORS IN OTHER QUANTITIES . . . . .	119
	REFERENCES . . . . .	121

## LIST OF FIGURES

1.1	Scanning electron microscopy image of melamine-formaldehyde microspheres. These microspheres, which are referred to as “dust particles” or “particles” in this thesis, are introduced into a plasma, where they are dispersed and do not touch one another as shown here. The particles I used were 4.83 $\mu\text{m}$ and 8.09 $\mu\text{m}$ , slightly smaller than those shown here. This image is reproduced courtesy of Dr. Karl-Heinz Lerche, microParticles GmbH, Berlin, Germany. . . . .	1
1.2	View of my single-layer suspension of dust particles, confined in a glow discharge plasma. Viewed from a side port window of the vacuum chamber (as discussed in Sec. 2.1.1), the suspension is illuminated by a horizontal 577-nm yellow-green laser sheet (as discussed in Sec. 2.1.5) that enters the chamber from a port window on the right. Another circular side port window is seen on the far side. The interior of the stainless-steel vacuum chamber appears to be a violet color due to glow emission from the argon glow-discharge plasma. The lower electrode is seen in the bottom half of the image. A negative dc self-bias voltage on the lower electrode provides a dc electric field that levitates the negatively-charged dust particles against the downward force of gravity (as discussed in Sec. 2.1.1 and 2.1.3). The lower electrode also has a cylindrical depression of 3 mm depth (as discussed in Sec. 2.1.3), to promote horizontal confinement. The dust particles, shown magnified in the inset, are dispersed with approximately 0.5 mm spacing between particles. . . . .	2
1.3	Video microscopy images of 2D particle suspension with typical solid (a) and liquid (b) structures, from the experiment reported in Chapter 5. . . . .	5
2.1	Plasma chamber used for the experiments. The vacuum chamber is a modified version of the GEC Reference Cell, with a large window on the top flange replacing the original GEC upper electrode, and a 22.2 cm diameter lower electrode. The lower electrode in Chapter 3 was flat, while in Chapters 4 and 5 it had a shallow cylindrical depression of diameter 9.6 cm and a depth of 0.3 cm. Photograph courtesy of John A. Goree. . . . .	17
2.2	Sketch of particle levitation and confinement. A dc electric field in the lower sheath levitates particles against the downward force of gravity. A slight curvature of the sheath, not shown here, provides radial confinement. The dc electric fields are much stronger in the sheath than in the main plasma (glow region), as indicated by the electric potential sketched on the right. . . . .	19

2.3	Particle imaging and manipulation. A vacuum chamber, shown in Fig. 2.1, encloses the lower electrode. The primary diagnostic is video microscopy using a top-view camera with an illumination laser. Another laser, used to manipulate particles, is directed from two sides using scanning mirrors. . . . .	21
2.4	Experimental bitmap images of a single-layer suspension of microspheres in a dusty plasma. Each bright spot corresponds to one particle. Here, (a) is $\approx 1/12$ of the original image from a narrow FOV camera (Phantom v5.2), and (b) is a magnified view, showing that a bright spot fills several pixels. Spot size depends on such factors as camera type and focusing. A particles position is calculated as the bright spots center. . . . .	22
2.5	Video microscopy image (a), and the corresponding particle positions (b) and Voronoi diagram (c). The suspension has the structure of an ordered solid lattice in the top half of each panel, but a disordered liquid in the bottom half. Defects in a lattice are identified in a Voronoi diagram as non-six-sided polygons, which are shown in color. The original video microscopy image was much larger than the portion shown in panel (a). These data are from an experiment reported in Chapter 4. . . . .	25
3.1	Temporal development of temperature and structure. (a) Time series of particle kinetic temperature $T(t)$ , when laser heating was switched on and then off. Times marked b-g correspond to panels below. (b)-(g) Voronoi diagrams, showing defects in color. Polygons indicate the number of nearest neighbors of a particle: red (5), white (6), blue (7), and green (others). . . . .	33
3.2	Time series of structure indicators and temperature. (a) Defect fraction (the area of defective polygons, as a fraction of total area, in Voronoi diagrams as in Fig. 3.1). (b) Height of the first peak of the pair correlation function $g(r)$ . This is an indicator of short-range translational order. (c) $G_\theta$ [72], an indicator of short-range orientational order. This can vary from zero for a gas to unity for a perfect crystal. (d) Time series for the three structure indicators and temperature, rescaled to vary from zero (for a solid before heating) to unity (for a liquid during heating). Data are smoothed over 3 frames. . . . .	35

3.3	Hysteresis diagram made by combining data from Figs. 3.1 and 3.2. The time interval between data points is 0.018 s. Initially, I had a solid, lower left corner. Then rapid heating was applied, causing a temperature increase across the melting point without much change in structure, the lower horizontal line of data points. This is a signature of solid superheating. Next, the superheated solid melted, as shown by the nearly vertical line of data points on the right. The resulting liquid in the upper right corner had a high defect fraction. Later, during rapid cooling, defect fraction dropped dramatically as the temperature declined. Finally, the suspension slowly recrystallized. . . . .	36
4.1	Temporal development of kinetic energy (KE), flow, and transverse velocity. (a) Time series of the average KE. Shear was applied suddenly by applying 0.95W of laser power starting at $t = 0$ . The KE rose about two orders of magnitude until a steady state was reached at $\approx 1$ s. (b) Spatiotemporal evolution of the flow velocity $\langle v_x \rangle_x$ . Two counter-propagating flow regions broaden to a width $\Delta Y_f$ (defined as FWHM of the velocity profile). Length scales, including the thickness $\Delta Y_l$ and spacing $L$ of the laser sheets, are ordered as $\Delta Y_l \approx a < \Delta Y_f < L$ . (c) Coherent longitudinal waves, generated near the flow region and propagating outward. This is revealed by the repeated pattern of wavefronts in this plot of $\langle v_y \rangle_x$ . For comparison, the longitudinal sound speed $C_l$ is indicated by the straight lines. The observed wave period is $\approx 4\pi\omega_{pd}^{-1}$ . . . . .	46
4.2	Two melting stages, due to the spatial development. (a) Phase diagram, showing the proliferation of defects as the KE increases, recorded at 0.018 s intervals, for three laser powers. A transition between two stages is revealed. The quantity plotted is the defect area fraction; this measure of structure is the area of a Voronoi diagram that is occupied by defects [86], divided by the total area. (b) Time series for KE and defects, counted separately inside and outside the flow regions of width $\Delta Y_f$ . The timing indicates that defects proliferate outside only after they saturate inside the flow regions. (The inset shows about 1/4 of the Voronoi diagram, for the run at 0.95 W at $t = 0.16$ s.) . . . . .	48
4.3	Spatiotemporal evolution of orientational order, $ \phi_6 $ , which is defined to have a maximum of unity for a perfectly crystalline region [42, 44, 91]. Lines are drawn with the slopes $C_t$ and $C_l$ , starting at $t = 0$ . The transverse sound speed, $C_t$ , coincides with the melting front propagation. The resolution of my data along the $Y$ axis is $1.9 a$ . . . . .	50

5.1	Particle trajectories in a 2D liquid, with color representing time. To illustrate the random particle motion, (a) shows $\approx 10\%$ of the spatial region I analyzed, for a duration $60 \omega_{pd}^{-1}$ which is about $\approx 10\%$ of one movie, i.e., one run in the experiment, while (b) is a part of a Langevin MD simulation, shown over the same time interval. . . .	57
5.2	Transverse current autocorrelation function (TCAF) in the 2D liquid computed using Eq. (5.1) for (a) the experiment at $kb = 3.26$ , and (b) the Langevin MD simulation at $kb = 3.28$ . At short times, the TCAF decays due to viscous effects, while at longer times (after its first positive zero crossing, $t_I$ ) it oscillates due to elastic effects. The frequency spectrum for each TCAF, shown in the insets, reveals a peak that is a signature of the elastic contribution to viscoelasticity. These results are different from the pure monotonic decay of TCAF and its spectrum that would be observed in a purely viscous regime. (Here, $b$ is the lattice constant measured before melting.) . . . . .	59
5.3	The wavenumber-dependent viscosity $\eta(k)$ of the 2D liquid, computed using Eq. (5.2) for (a) the experiment and (b) simulations of two sizes. I find that $\eta(k)$ diminishes with $k$ , which is a signature of viscoelastic effects. The size of the smaller simulation mimics the size of the experiment; comparing them reveals that the scatter of the experimental data (a) arises from the data size. In (b), the Green-Kubo (static) viscosity $\eta$ is indicated by a star symbol. Here, the kinematic viscosity $\eta(k)/\rho$ and wavenumber $k$ are normalized to be dimensionless. . . . .	61
6.1	A typical example of the self-intermediate scattering function (self-ISF) for a normal liquid. Relaxation happens in two steps: early-time caging motion, and long-time diffusive motion. The self-ISF curve is often modeled by Eq. (6.5). . . . .	69
6.2	Time dependence of the self-ISF for various wavenumbers ( $k$ ) for the Langevin molecular dynamics (MD) simulation in the liquid regime: $\Gamma = 200$ , $\kappa = 2$ and $\nu/\omega_{pd} = 0.027$ . The solid lines are the corresponding fits to Eq. (6.5). . . . .	73
6.3	The fitting parameters, relaxation time $\tau$ in (a) and exponent $\beta$ in (b), as a function of $k$ . These cross symbols are from fitting the data in Fig. 6.2 for the Langevin MD simulation, and the circle symbols are for the frictionless MD simulation for the same $\Gamma = 200$ , $\kappa = 2$ . . . . .	76
6.4	The self-ISF for the length scale corresponding to the lattice constant, $k = 2\pi/b$ . Results shown are for the Langevin MD simulations with constant values of $\kappa = 1.2$ and $\nu/\omega_{pd} = 0.027$ , and varying $\Gamma$ . A transition near $\Gamma = 200$ is indicated by a change in the curve's shape, and by larger gaps between curves for solids, $\Gamma > 200$ . . . . .	78

6.5	The self-ISF at $k = 2\pi/b$ , as in Fig. 6.4 but with varying $\kappa$ . The simulations here are all Langevin MD simulations with constant values of $\Gamma = 200$ and $\nu/\omega_{pd} = 0.027$ . A transition near $\kappa = 1.2$ is indicated by a change in the curve's shape, and the gaps between curves. . . . .	80
6.6	Structure relaxation time measured from Figs. 6.4 and 6.5 as a function of (a) temperature and (b) screening parameter $\kappa$ . The structure relaxation time in my 2D underdamped Yukawa system does not obey the Arrhenius law or Vogel-Fulcher law. The same data are plotted in the inset as a function of number density $1/\kappa^2$ , for the liquid regime. . . . .	82
6.7	The self-ISF at $k = 2\pi/b$ for the simulations at different damping rate $\nu$ . The simulations here include both Langevin MD simulations and frictionless MD simulations in a liquid regime, with constant values of $\Gamma = 200$ and $\kappa = 3$ . Unlike temperature and number density, changing the friction does not significant change the shape of the curves. The effect of friction in the self-ISF curves is a retardation of the decay at higher damping rate. . . . .	83
7.1	Experimental bit-map images of a monolayer suspension of microspheres in a dusty plasma. Each bright spot corresponds to one particle. Here, (a) is 1/12 of the original image from a digital camera and (b) is a magnified view, showing that a bright spot fills several pixels, while in (c) from an analog camera a bright spot fills about $5 \times 5$ pixels. Spot size depends on such factors as camera type and focusing. A particle's position is calculated as the bright spot's center; errors in this calculation are the topic of this chapter. . . . .	87
7.2	Histogram of intensity values of pixels in the original experimental image of Fig. 7.1(a). The inset shows the same data with a logarithmic scale. The prominent peak, centered at $I_{bg}$ , is due to noise in the camera. . . . .	88
7.3	Illustration of the method for calculating a sub-pixel map. First, a $10 \times 10$ pixel bit-map image (not shown here) is analyzed to yield a map (a) of particle positions. Second, the same positions are plotted relative to pixel edges in (b); these values are the fraction parts of the calculated positions. (c) An example sub-pixel map of $N = 617$ particles, calculated from an experimental image (full view of Fig. 7.1(c)), reveals pixel locking as a tendency of calculated positions to be concentrated at favored positions including the center and edges of pixels. . . . .	91

7.4	Illustration of boundaries. In algorithms for calculating particle positions from a bit-map image, the first step is selecting the contiguous pixels to be used, as defined by a boundary (solid white line) that encloses them. The codes tested here differ only in the way they select boundaries. (a) In ImageJ, only contiguous pixels above a threshold are included in the boundary. Code A (b) and Code K (c) use boundaries that are the smallest rectangles that enclose: all the contiguous pixels above the threshold in Code A, or the dashed contour produced by a 2D contour-plotting routine in Code K. . . . .	92
7.5	Magnified images of bright spots. (a) Experimental image from a digital video camera. (b),(c) Synthetic images, with a Gaussian profile centered on a known true position, here with two different spot radii. In generating synthetic images, I first choose the true position randomly, and then calculate the intensity of each pixel using Eq. (7.5) so that it includes both signal and noise. . . . .	94
7.6	The rms error of calculated positions as a function of the threshold $I_{th}$ . In general, errors increase with threshold, and superimposed on this increase is an oscillation. The rms errors are always calculated as in Eq. (7.6) using $N = 5000$ . (Here, $r_{spot} = 1.5$ pixel units, $I_{peak} = 5334$ intensity value units, corresponding to a total signal intensity $\sum I_{sig\ k} = 37\ 707$ . Also, $I_{base} = 0$ .) . . . . .	98
7.7	Cause of oscillations. Boundaries, selected in the first step of ImageJ, enclose fewer pixels as the threshold is increased. Removing one pixel from the boundary causes a discrete jump in the calculated particle position in Eq. (7.2). As the threshold increases, there is a sequence of jumps, as the boundary becomes smaller, one pixel at a time. These jumps, in aggregate for many particles, lead to oscillations in the rms error as the threshold is varied, a phenomenon I term the boundary effect. The three columns correspond to three different true positions.	99
7.8	Sub-pixel maps for $N = 100\ 000$ randomly distributed true positions. The signature of pixel locking is generally more severe for higher thresholds. (Here, $r_{spot} = 1.5$ , $I_{peak} = 5334$ , and $I_{base} = 0$ .) .	100
7.9	Simulation of slight lens defocusing. The optimal range of spot size lies between two other ranges: for very small $r_{spot}$ , errors worsen due to pixel saturation; for very large $r_{spot}$ , they worsen due to random errors. For my parameters, these two ranges are for $r_{spot} < 0.8$ and $r_{spot} > 2.0$ , respectively. Oscillations in the optimal range arise from a boundary effect. (Here, $I_{th} = 1000$ , $I_{base} = 0$ , and $\sum I_{sig\ k} = 37\ 707$ .)	101

7.10	The rms error as the intensity is varied, to simulate adjusting the illumination brightness, the exposure time or the camera aperture. The main trend is that the error decreases with increasing intensity due to an improved signal-to-noise ratio (SNR), as indicated by solid curves; the opposite trend, indicated by dashed curves, is attributed to a pixel-locking effect that I term the pedestal effect. (Here, $r_{spot} = 1.5$ , $I_{th} = 740$ , and $I_{base} = 0$ .) . . . . .	104
7.11	Cross section of a bright spot, illustrating the “pedestal.” Pixels brighter than the threshold identify the boundary for ImageJ in the first step. In the second step, both shaded portions contribute to the calculated particle position if $I_{base} = 0$ , i.e., if no baseline is subtracted in Eq. (7.2). The lower shaded portion, marked “pedestal,” can heavily influence the calculated particle position. The pedestal can be reduced by choosing $I_{base} = I_{bg}$ , or eliminated altogether by choosing $I_{base} = I_{th}$ . . . . .	105
7.12	Test of different baselines. The best choice to minimize rms error is subtracting a baseline equal to the threshold $I_{th}$ in Eq. (7.2). (I used ImageJ, and $r_{spot} = 1.5$ , $I_{th} = 740$ , and $I_{bg} = 384$ .) . . . . .	106
7.13	Sub-pixel maps, using a baseline $I_{base} = I_{th}$ for two different thresholds (a) $I_{th} = 1150$ and (b) $I_{th} = 2950$ . Comparing these panels shows that the signature of pixel locking can be virtually eliminated, as in (a), by making the best choice of threshold as well as choosing $I_{base} = I_{th}$ . (Here, I used the same 100 000 images as in Fig. 7.8.) . . . . .	107
7.14	Total error, using a baseline $I_{base} = I_{th}$ . Comparing to Fig. 7.6 where $I_{base} = 0$ , errors have been reduced. The lowest rms error that can be achieved with these images is 0.017, using the same optimal choice of parameters as in Fig. 7.13(a). (I used the same 5000 images as in Fig. 7.6. Here and in Fig. 7.13, I used ImageJ.) . . . . .	108
7.15	Experimental bit-map images of a monolayer suspension of microspheres in a dusty plasma. Here, (a) is 1/12 of the original image and (b) is a magnified view. A bright spot fills about $5 \times 5$ pixels. Compared to Fig. 7.1(a), the hardware was improved by slight lens defocusing. . . . .	111
7.16	Choosing the coarse range of threshold using experimental images. Counting the particles identified in 100 images, I choose the nearly flat portion $325 \leq I_{th} \leq 925$ as the coarse range. Outside this coarse range, many false particles appear at lower $I_{th}$ due to noise, while many true particles are missed at higher $I_{th}$ . Labels a-h identify thresholds used in Fig. 7.17. . . . .	112

7.17 Experimental sub-pixel maps for different thresholds within the coarse range. Here, (a) is an entire map, and (b)-(h) show the lower left corner. I choose the lowest  $I_{th}$  with a weak signature of pixel locking, 325. The signature is stronger for  $I_{th} \geq 525$ , with a concentration of calculated positions on pixel edges. Vastly better than Fig. 7.3(c), there is no obvious signature of pixel locking for  $I_{th} < 525$ . (Here, I used ImageJ with  $I_{base\ k}$  calculated from Eq. (7.7) and a dark-field image.) . . . . . 113

## CHAPTER 1 INTRODUCTION

### 1.1 Review of dusty plasma concepts

#### 1.1.1 Dusty plasma

Plasma is generally defined as a quasineutral gas of charged and neutral particles which exhibits collective behavior [1]. Most plasmas consist of electrons, positive ions and neutral gas. Plasmas can also contain micron-size particles of solid matter, which are often called dust particles following the terminology of astrophysics. Dust particles could be made of any material, although dielectric materials are most common. My experiments reported in Chapters 3-5 made use of polymer microspheres, Fig. 1.1.

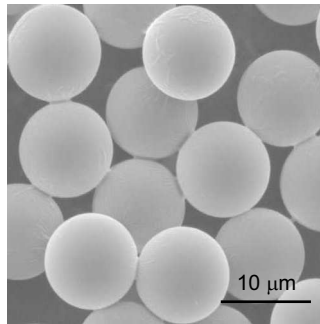


Figure 1.1: Scanning electron microscopy image of melamine-formaldehyde microspheres. These microspheres, which are referred to as “dust particles” or “particles” in this thesis, are introduced into a plasma, where they are dispersed and do not touch one another as shown here. The particles I used were  $4.83 \mu\text{m}$  and  $8.09 \mu\text{m}$ , slightly smaller than those shown here. This image is reproduced courtesy of Dr. Karl-Heinz Lerche, microParticles GmbH, Berlin, Germany.

Experiments with dusty plasmas began in the late of 1980’s. An IBM scientist, Gary Selwyn, first observed a dust cloud that was confined in a glow-discharge

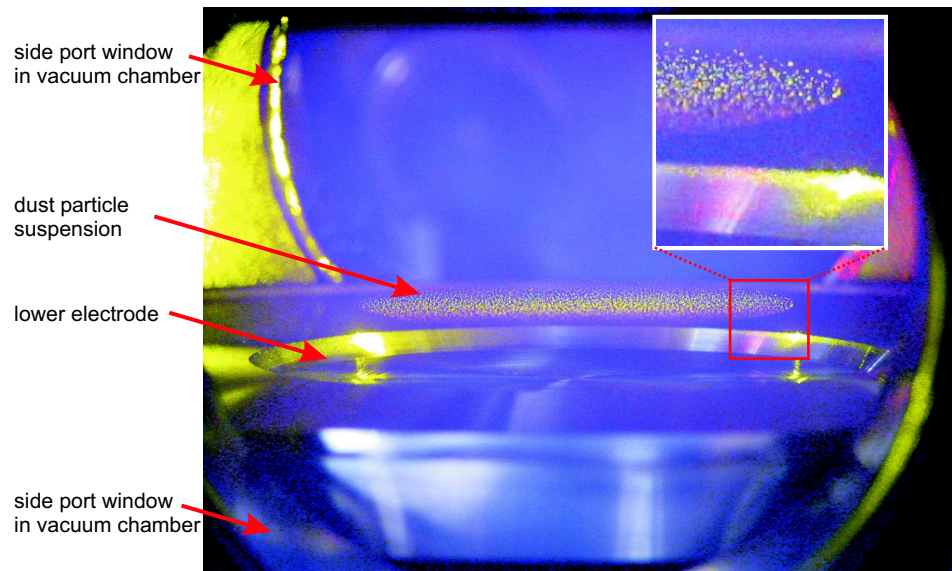


Figure 1.2: View of my single-layer suspension of dust particles, confined in a glow discharge plasma. Viewed from a side port window of the vacuum chamber (as discussed in Sec. 2.1.1), the suspension is illuminated by a horizontal 577-nm yellow-green laser sheet (as discussed in Sec. 2.1.5) that enters the chamber from a port window on the right. Another circular side port window is seen on the far side. The interior of the stainless-steel vacuum chamber appears to be a violet color due to glow emission from the argon glow-discharge plasma. The lower electrode is seen in the bottom half of the image. A negative dc self-bias voltage on the lower electrode provides a dc electric field that levitates the negatively-charged dust particles against the downward force of gravity (as discussed in Sec. 2.1.1 and 2.1.3). The lower electrode also has a cylindrical depression of 3 mm depth (as discussed in Sec. 2.1.3), to promote horizontal confinement. The dust particles, shown magnified in the inset, are dispersed with approximately 0.5 mm spacing between particles.

plasma. Dust particles were seen suspended in a cloud above a horizontal electrode inside a chamber that was used for plasma etching of semiconductor wafers [2]. Selwyn found that, inside the plasma, dust particles nucleated and grew by aggregating materials from gases. While the plasma was on, the dust particles were levitated, i.e., suspended in the plasma, despite the downward force of gravity. This levitation indicated that electric charging occurred on particles. Selwyn observed the dust particles *in situ* by laser light scattering and imaging with a photographic

camera. When the plasma was switched off, Selwyn's dust particles fell to the bottom of the chamber. Although particle growth and levitation is undesirable for semiconductor manufacturing, Selwyn's discovery inspired other experimenters who wished to purposefully charge and confine dust particles within a plasma. In 1994, experimenters [3, 4, 5] discovered that these methods of producing dusty plasma allow the study of strongly-coupled plasma as predicted by Ikezi [6]. A photograph of a suspension of dust particles is shown in Fig. 1.2.

### 1.1.2 Strongly-coupled plasma

Strongly-coupled plasma is a collection of free charged particles where the Coulomb interaction with nearest neighbors is so strong that particles do not easily move past one another [7]. The most widely used parameter for strongly-coupled plasma is  $\Gamma$ , which is defined as the ratio of the potential energy between neighboring particles and the kinetic energy. It is expressed as

$$\Gamma = Q^2(4\pi\epsilon_0r)^{-1}/(k_B T), \quad (1.1)$$

where  $T$  is the kinetic temperature of the particles and the characteristic interparticle distance  $r$  is typically defined as either the lattice constant  $b$ , or the Wigner-Seitz radius  $a$ . Based on Ichimaru's definition [7], if  $\Gamma > 1$ , then the plasma is strongly-coupled.

Plasma can become strongly coupled due to either *high density* as in neutron star crusts [8] and white dwarf stars [9], *low temperature* as in pure ion plasma [10], or *high particle charge* as in dusty plasma [11]. Until twenty years ago, strongly-coupled plasmas were mainly studied theoretically, because of a lack of suitable laboratory methods. Laboratory strongly-coupled plasma experiments became more common with the discoveries of ways to form dusty plasma [11], laser cooled ion plasmas in a Penning trap [10], and ultracold neutral plasmas [12].

While particle motion in weakly-coupled plasmas is like molecular motion in gases, with particles moving past one another easily, motion in strongly-coupled plasmas resembles that in liquids or solids. Due to Coulomb interactions, charged particles in a strongly-coupled plasmas cannot move freely, but instead remain in relative fixed positions with respect to nearest neighbors. For high values of  $\Gamma \gg 100$ , random motion is so weak that particles tend to remain trapped or caged near equilibrium positions centered among nearest neighbors and particles self-organize in a crystalline-like lattice. For moderate values of  $\Gamma \gg 1$ , the particles do not remain caged for a long time, and they do not line up in long straight lines as in a crystalline lattice. This latter condition is like a liquid, or for  $\Gamma \approx 1$  like a non-ideal gas. Strongly-coupled plasmas are often described in term of structure, which is the spatial pattern at a microscopic scale for the arrangement of particles. A weakly-coupled plasma, like a gas, has no structure, and particles have nearly random positions with respect to nearby particles. Strongly-coupled plasma can have the structure of a crystalline lattice or solid for  $\Gamma \gg 100$ , and the structure of a liquid for  $\Gamma \gg 1$ . Images from one of my experiments, illustrating solid and liquid-like structure, are shown in Fig. 1.3.

While strongly-coupled and weakly-coupled plasmas have much in common, the theoretical and experimental methods used to study them are usually different. Weakly-coupled plasmas are usually studied theoretically using *continuum* methods, treating each component as a continuum in the case of Vlasov or two-fluid models, or treating the entire plasma as a single continuum in the case of MHD model. When a *particle* model is used to model weakly-coupled plasmas, Coulomb collision are weak and often ignored. Strongly-coupled plasmas can also be treated as a continuum, but they are more often treated as a collection of discrete particles. This is because of the strong effects of particle-particle Coulomb interactions. Unlike

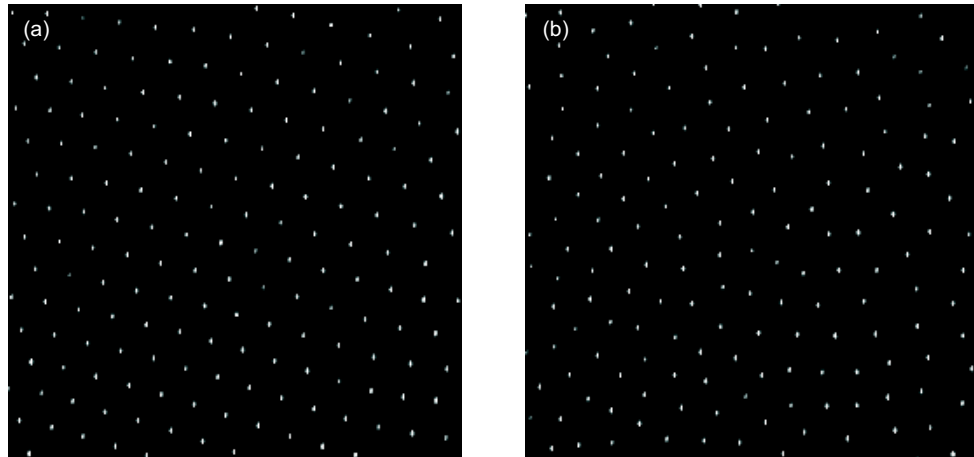


Figure 1.3: Video microscopy images of 2D particle suspension with typical solid (a) and liquid (b) structures, from the experiment reported in Chapter 5.

experiments with weakly-coupled plasmas, where parameters that are measured are usually continuum parameters, such as number density or current, experiments with strongly-coupled plasmas usually allow the particles themselves to be imaged individually. This allows studies at the level of discrete particles. Strongly-coupled plasmas exhibit some of the same phenomena as weakly-coupled plasmas, such as waves, transport, and instabilities, but with significant differences. For example, waves have different dispersion relations in strongly-coupled and weakly-coupled plasmas. Another difference is that physical problems in strongly-coupled plasmas can be classified as studies of either structure or dynamics, whereas in weakly-coupled plasmas there is no structure arising from Coulomb interactions.

### 1.1.3 Yukawa interaction

In dusty plasma experiments, I usually use polymer microspheres with a diameter of several microns, Fig. 1.1. When these dust particles are immersed in the plasma environment, they will disperse and absorb both electrons and positive ions continuously. Since electrons have a much higher thermal velocity than positive

ions, the dust particles will become negatively charged. For micron-size particles, this negative charge is typically several thousand elementary charges.

After they become charged, dust particles in the plasma environment disturb nearby electrons and positive ions, yielding a non-neutral region called a “sheath” that surrounds each dust particle. The thickness of this sheath around a dust particle is characterized by the Debye length,  $\lambda_D$ . This sheath shields the electrostatic interaction between two dust particles if they are separated by large distances  $r \gg \lambda_D$ . As was demonstrated experimentally [13], in a plane perpendicular to ion flow, the interaction between particles is accurately modeled by a repulsive Yukawa potential,

$$\phi(r) = Q(4\pi\epsilon_0 r)^{-1}\exp(-r/\lambda_D), \quad (1.2)$$

which is the electric potential at a distance  $r$  for an isolated dust particle of charge  $Q$ .

#### 1.1.4 Forces acting on dust particles

One hallmark of dusty plasma experiments is that the dust particles experience many kinds of forces. In addition to the electric and Lorentz forces, they also experience: gravity, the radiation-pressure force, gas drag, ion drag, and thermophoretic forces.

In my experiments, only four of these forces are considerable: gravity, electric, radiation pressure, and gas drag forces. The relative strengths of the forces can be understood by considering their scaling with particle radius,  $r_{dust}$ . The gravitational force, which is proportional to  $r_{dust}^3$ , is substantial in my experiments because  $r_{dust}$  is several microns, while it would be negligible for nanometer-size particles. The electric force and Lorentz force are both proportional to  $r_{dust}$  because of the capacitance of dust particles. The electric force is important in my experiment; it provides not only the (upward) levitation force against (downward) gravity, but

also the interparticle interaction in the horizontal plane that yields all the collective effects that I will study. However, since an additional magnetic field is not used, the Lorentz force is negligible. The other forces are all proportional to  $r_{dust}^2$ . These include the radiation pressure force, which occurs when powerful laser beams are applied so that photon momentum is deflected or absorbed by particles, thereby imparting a force. The laser radiation force provides an external energy input that is easily controlled to manipulate particles, as I explain in Sec. 1.1.6. The gas drag force provides energy dissipation; this is the resistance experienced by a particle moving relative to gas at velocities  $v_{dust}$ . For the low gas pressure in my experiments, the gas drag force  $F_{gas}$  can be modeled using the Epstein's expression [14], where  $F_{gas} \propto v_{dust}$ . Following the traditional nomenclature [14], I use the damping rate,  $\nu_f = F_{gas}/(m_{dust}v_{dust})$ , to express the gas drag force. The ion drag force is aligned with the vertical confinement of my experimental setup (which will be explained in Sec. 1.1.5), but it is small due to low ion density. The thermophoretic force is negligible due to small temperature gradient in my experiments.

### 1.1.5 Two dimensionality

To study two-dimensional (2D) physics in my experiments, I used a single-layer suspension of dusty plasma. Above the horizontal lower electrode, there is a non-neutral sheath region that provides vertical confinement. When dust particles fall into the sheath, the strong electric field there will provide an upward levitation force that balances the downward force of gravity. Horizontal confinement is provided by natural horizontal electric fields in the glow-discharge plasma, due to the ambipolar diffusion arising from the different masses of electrons and positive ions. The combination of vertical and horizontal confinement results in an infinite confinement time for the dust particles. Electrons and positive ions, however, are not confined in a glow-discharge plasma. Details of the vertical and horizontal

confinement will be presented in Sec. 2.1.3.

The motion of my dust particles is constrained to be mostly two-dimensional. Random motion in the vertical direction, i.e., out-of-plane displacement, is small due to strong vertical confinement forces. In my experiments, the single layer of particles was never observed to buckle. While the dust particles are essentially constrained to a 2D plane, the electrons and positive ions are not. They fill the entire three-dimensional (3D) volume of the plasma chamber.

Studying 2D physics has considerable value. First, all 2D physical systems are intrinsically interesting for theoretical reasons. Second, there are several famous examples of 2D physical systems, and much of what I learn about mine will apply to those. Examples of 2D physical systems include Wigner lattices of electrons on the surface of liquid helium [15], vortices in superconductors [16], colloids [17] and granular materials [18]. Third, 2D systems allow experimental observation at a microscopic level of phenomena such as melting and transport that also occur in 3D systems including 3D strongly-coupled plasmas. Thus, insight gained in studies of 2D systems is helpful for understanding 3D physics as well.

#### 1.1.6 Manipulation

Dusty plasma can be manipulated easily using many methods. The various forces acting on dust particles listed above can be exploited to push particles in a dusty plasma. Some of the earliest manipulation schemes involved simply adjusting plasma parameters, such as gas pressure or ion density, which regulate some instabilities [19, 20]. Later, magnetic and electrostatic forces were employed to manipulate dusty plasma [21], and electric pulses were used to apply a sudden energy input [22, 23]. Thermal gradients were used to help levitate dust particles, allowing the formation of 3D dusty plasmas, which are called “Coulomb balls” or “Yukawa balls” [24].

A more recently developed manipulation method that I used in my experiments exploits the radiation pressure force applied by laser beams [25]. Laser manipulation offers several advantages, compared to other methods. First, laser manipulation only affects the motion of dust particles; other components in the plasma environment, such as electrons, ions, neutral gas atoms, will not be disturbed by laser manipulation. Plasma parameters, such as particle charge, Debye length, electron density, ion flow, and sheath thickness are also not affected by laser manipulation at all. Second, laser beams can be rastered in well-defined patterns using scanning mirrors driven by servos. This allows one to manipulate particles in a small region, or everywhere. Power can be applied suddenly, constantly, or with any desired temporal modulation. One of the earliest uses of laser manipulation was the excitation of longitudinal [25] and shear waves [26], which can be difficult to excite using other methods.

## 1.2 Dusty plasma as a model system

### 1.2.1 Studying liquids and solids at an atomistic scale

Since the experimental discovery that dusty plasmas provide a convenient way to experiment with strongly-coupled plasmas [3, 4, 5], they have attracted considerable attention. One striking aspect of the experiments is the use of video microscopy (e.g. Fig. 1.3), which allows individual particles to be identified and tracked. Micron-size particles are readily imaged because they scatter sufficient laser light and because in a plasma they are separated by a distance of typically 0.5 mm, which is easily resolved in the images. The particles also move slowly; the typical dynamical time scale is about  $10^{-2}$  s, which is suitable for high-speed video recording.

The ability to track the motion of individual particles provides opportunities to perform experiments where the dust particles are analogous to atoms or molecules in conventional liquids and solids. Of course, in most liquids and solids it is not practical to track the motion of atoms or molecules, so there is considerable value in performing experiments with “model systems” that have larger particles that interact amongst themselves in the same way that atoms or molecules do in conventional liquids and solids. Some of the physics that has been studied using dusty plasmas as a model system include waves [27], transport [28, 29, 30, 31], and phase transitions [19, 20, 32].

### 1.2.2 Comparison to other model systems

Compared with other model systems, such as colloidal suspensions and granular materials, dusty plasmas have unique features that enable new kinds of experiments. Unlike the overdamped colloidal systems, in a plasma dust particles only experience the damping from the rarefied gas, so that a dusty plasma is an underdamped system. Many interesting dynamics, such as microscopic motion during thermal transport and wave propagation, are easily observed in underdamped dusty plasmas without being affected by the medium. These same dynamics cannot be observed in overdamped colloidal systems. Additionally, it is possible to control the kinetic temperature of dust particles independently of the temperature of the background medium of the plasma, unlike the case of colloids where particles are in thermal equilibrium with a solvent whose temperature cannot be varied over a wide range. Unlike the strong hard-sphere interaction in granular fluids, the interparticle interaction in dusty plasmas is a soft Yukawa interaction [13].

These properties of dusty plasma make it possible for us to study many dynamical processes microscopically, at a scale analogous to the atomistic scale in conventional liquids and solids [11]. In my thesis, I will exploit these properties

of dusty plasma to study several condensed matter physics topics that cannot be studied easily any other way.

### **1.3 Topics in strongly-coupled plasmas and condensed matter physics**

#### 1.3.1 Solid-liquid transition and solid superheating

Melting and solidification, which are solid-liquid phase transitions, are important physics problems for both strongly-coupled plasmas and condensed matter. Two exotic examples of this phase transition are solid superheating and liquid supercooling. A superheated solid has the microscopic structure of a solid, but a temperature above the melting point [33]. A supercooled liquid is the opposite; it has the microscopic structure of a liquid, but a temperature below the freezing point [33].

Observing solid superheating in condensed matter was once thought to be impossible [34], but it is now practical due to new instrumentation for heating [35, 36] or fabricating special samples [37, 38]. Despite these new kinds of instrumentation, however, I found that the literature for solid superheating lacks experiments performed with atomistic-scale observation of the kind that is possible with dusty plasmas. The literature for solid superheating also lacks experiments in any kind of strongly-coupled plasma. While experiments with strongly-coupled plasma have demonstrated solid and liquid [19, 20, 23, 32] behavior, and recently supercooled liquid as well [39], they have until now not demonstrated superheated solid behavior. Since dusty plasmas allow both imaging at an atomistic scale and controlled heating using laser manipulation, I used dusty plasma to perform an experimental study of solid superheating.

### 1.3.2 Shear-induced melting

Melting, which has always been an important problem in strongly-coupled plasmas and condensed matter physics, can be induced several ways, including the application of shear [40, 41, 42, 43, 44, 45]. Shear-induced melting has been studied in simulations [42, 43, 44, 45] and theories [41]. Experimental studies of shear-induced melting have been performed in a variety of physical systems, including colloidal suspensions [40, 46], 2D electron crystals with magnetic field [47], foams [48], polymer glasses [49], and dusty plasmas [50].

Most previous experimental and theoretical studies of shear-induced melting have concentrated on steady-state conditions only. If shear were instead applied suddenly, one could investigate the spatiotemporal development of shear-induced melting. However, until now, there have been no such experiments reported in any physical system. Since dusty plasma allows atomistic observation and the local application of shear force using laser manipulation, I used dusty plasma to study the spatiotemporal development of shear-induced melting.

### 1.3.3 Viscoelasticity

Viscoelasticity is a property of materials that exhibit both viscous and elastic characteristics [51]. Usually, one thinks of viscous properties for liquids and elastic properties for solids, but most materials are viscoelastic and exhibit both properties. Viscoelastic materials include, for example, polymer, human tissue, and hot metal [51]. In general, liquids exhibit elastic effects at short length or time scales [52], but viscous effects in the opposite case of long length or time scales. Below, I will review the strongly-coupled plasma literature for viscoelasticity, and then I will review how viscoelasticity is quantified in conventional liquids.

In the literature for strongly-coupled plasmas, viscoelasticity has been studied

both theoretically [53, 54] and experimentally [55, 56]. Kaw and Sen introduced viscoelastic coefficients in a generalized hydrodynamics model to describe the dynamics of strongly-coupled plasmas [53]. In a similar theoretical approach, Murillo generalized the viscosity coefficient by adding a viscoelastic relaxation time in a hydrodynamic model of strongly-coupled plasmas [54]. This approach yielded a viscoelastic Navier-Stokes equation [54]. There have been only a few strongly-coupled plasma experiments that involved viscoelasticity [55, 56]. Until now these experiments have yielded only descriptive presentations of the viscoelastic properties [55] and the corresponding microscopic motion of particles [56]. In other experiments, the static viscosity  $\eta$  was measured [50] and estimated from diffusion observations [21].

To quantify viscoelasticity, theorists in the field of liquid physics often use the frequency-dependent viscosity  $\eta(\omega)$  [57]. This function tends toward the more common static viscosity,  $\eta$ , as  $\omega \rightarrow 0$ . In 3D liquids,  $\eta(\omega)$  is easily measured using rheometers and viscometers [57].

Besides  $\eta(\omega)$ , the wavenumber-dependent viscosity,  $\eta(k)$ , has also been used by theorists to quantify the viscoelastic character of liquids [58, 59, 60, 61, 62]. They have recently developed ways of computing  $\eta(k)$  from the trajectories of random motion of molecules [61, 62]. However, until now, there have been no experimental measurements (in plasmas or any other kind of physical system) known to me of  $\eta(k)$ . Dusty plasma is a good candidate system to exploit this new method. Because the particle trajectories during random motion can be precisely measured in dusty plasma, I used dusty plasma to exploit the method of calculating  $\eta(k)$  to quantify the viscoelasticity of dusty plasma.

### 1.3.4 Intermediate scattering function in 2D dusty plasmas

The intermediate scattering function (ISF) [63], which has been used widely in other fields, is defined in terms of the particle trajectories:

$$F(\mathbf{k}, t) = \frac{1}{N} \sum_i \sum_j \langle \exp(-i\mathbf{k} \cdot [\mathbf{r}_i(t) - \mathbf{r}_j(0)]) \rangle. \quad (1.3)$$

Here,  $\mathbf{r}_i(t)$  is the trajectory of the  $i$ th particle in a system consisting of  $N$  particles. The Fourier transform variable  $\mathbf{k}$  is usually called a wavenumber, although no waves are studied using this method. Equation (1.3) makes use of an ensemble average  $\langle \cdot \cdot \cdot \rangle$ , which in practice is done by averaging for various initial starting times in place of  $t = 0$ . If the particle trajectories are known as they are in this thesis, then the ISF can be calculated directly using Eq. (1.3). This method has been used previously in some experiments [64, 65] and MD simulations [66, 67, 68] for systems other than strongly-coupled plasmas.

The ISF is a measure of particle dynamics. It has been widely used for studying dynamics in many fields, such as caging [65] and relaxation [64] in granular materials, diffusive dynamics in liquids [66], the aging effect in glass formation [67], and dynamic heterogeneities of gels [68]. I will borrow this tool from other fields to study two physical processes in dusty plasmas: relaxation in the liquid phase of strongly-coupled plasmas and the melting phase transition.

## 1.4 Organization of this thesis

There are eight chapters in my thesis. I will introduce my experiment setup and data analysis method in Chapter 2. In Chapters 3-6, I will present the four physics topics I studied in 2D dusty plasmas: solid superheating, evolution of shear-induced melting, viscoelasticity, and the intermediate scattering function. In Chapter 7, I will present improved methods of measuring particle positions that minimize

measurement errors. Finally, Chapter 8 is a brief summary of my thesis.

## CHAPTER 2 EXPERIMENTAL SYSTEM

### 2.1 Experimental setup

#### 2.1.1 Plasma chamber

My dusty plasma experiments are performed using a glow discharge, formed inside a vacuum chamber, Fig. 2.1, which is a modified version of the GEC Reference Cell [69, 70]. The typical base pressure of the vacuum chamber is about  $10^{-7}$  Torr. I use argon at a typical gas pressure of 10 mTorr to generate a glow discharge plasma. To achieve a high-purity argon gas environment at a stable pressure, 0.1 standard cubic centimeters per minute (sccm) argon gas flow is introduced in the chamber by an Alicat controller, while simultaneously an MKS butterfly valve with a feedback circuit is used to regulate the pressure by controlling the pumping speed.

In my experiments, the plasma is produced using a capacitively coupled electrodes. The lower electrode is an aluminum plate with a diameter of 22.2 cm. The upper electrode is a stainless steel ring of 2 cm width, which has a diameter similar to that of the lower electrode. The upper electrode is mounted to the upper flange, so that like the chamber walls it is grounded. A broad-band radio-frequency (rf) amplifier, Amplifier Research 200A15, is used to amplify 13.56 MHz rf waveforms from a function generator. The output of the amplifier, typically with 150 V peak-to-peak, is connected to a matching circuit, Nye Viking MB-V-A. In experiments, I adjust the matching circuit to minimize the reflected rf power to the amplifier. Finally, the rf current flows to the lower electrode through a capacitor, thereby blocking dc current. An oscilloscope is used to monitor the voltage and current at the lower electrode.

The plasma is ignited and sustained by rf electric fields. There are also dc

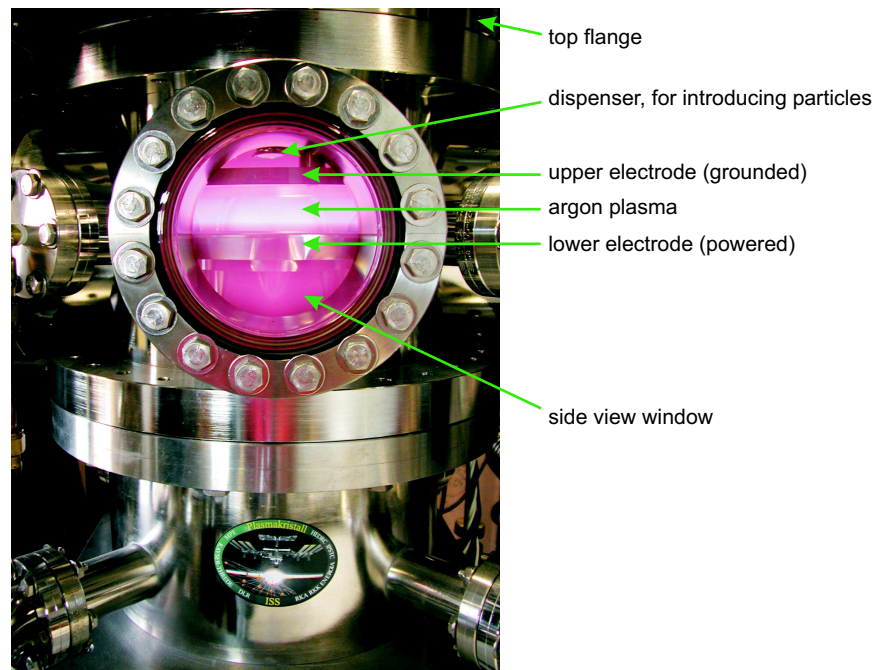


Figure 2.1: Plasma chamber used for the experiments. The vacuum chamber is a modified version of the GEC Reference Cell, with a large window on the top flange replacing the original GEC upper electrode, and a 22.2 cm diameter lower electrode. The lower electrode in Chapter 3 was flat, while in Chapters 4 and 5 it had a shallow cylindrical depression of diameter 9.6 cm and a depth of 0.3 cm. Photograph courtesy of John A. Goree.

electric fields that develop naturally in the plasma due to ambipolar transport of electrons and ions. Electrons are accelerated primarily by the rf electric field because of their tiny mass. However, positive ions and charged dust particles are not able to respond to the rf electric field because of their bigger mass; they can only respond to the dc electric field inside the plasma and its sheath region. Because of the different masses of electrons and positive ions, and the use of the blocking capacitor, a dc bias on the lower electrode develops. In my experiments, electrons impact argon gas atoms to sustain the ionization of the plasma. Figure 2.1 shows the glow discharge inside the vacuum chamber when the argon plasma is ignited. For the type of argon glow discharge plasma used in my experiments, typical plasma parameters are an

electron temperature of 1 eV and an electron number density of  $10^9 \text{ cm}^{-3}$ . The plasma is weakly ionized, with about 0.1% argon atoms ionized in the main plasma in the inter-electrode region.

### 2.1.2 Dust particles

I use polymer (melamine-formaldehyde) microspheres as dust particles, Fig. 1.1. This material is chosen because the particles do not tend to coagulate, but instead disperse when they are dropped into a plasma.

These polymer microspheres are monodisperse, with a diameter of either  $4.83 \pm 0.08 \text{ }\mu\text{m}$  or  $8.09 \pm 0.18 \text{ }\mu\text{m}$  [14]. They are placed inside a dispenser, which is a small stainless steel container with a single tiny hole at its bottom. The dispenser is attached to a small stainless steel rod installed in a vacuum feedthrough on the top flange so that it can be manipulated from outside of the chamber. At the beginning of an experiment, I introduce polymer microspheres by agitating the rod. After introducing particles into the plasma, I lift the dispenser well above the ring electrode and rotate it near the grounded wall of the chamber to minimize its effect on the electric field in the plasma.

### 2.1.3 Suspension

Because of gravity, dust particles fall inside the plasma when they are first introduced by the dispenser. At the same time, they become negatively charged almost immediately (with a time scale of a  $10^{-5} \text{ s}$ ). As they fall into the sheath above the lower electrode, the strong dc electric field in the sheath provides an upward force that levitates them against downward gravity, Fig. 2.2. In my experimental setup, the plasma density in the center is slightly higher than at the edges, so the sheath there is slightly thinner in the center. The slightly curved sheath, which is like a shallow bowl, provides a natural radial confinement for these dust particles,

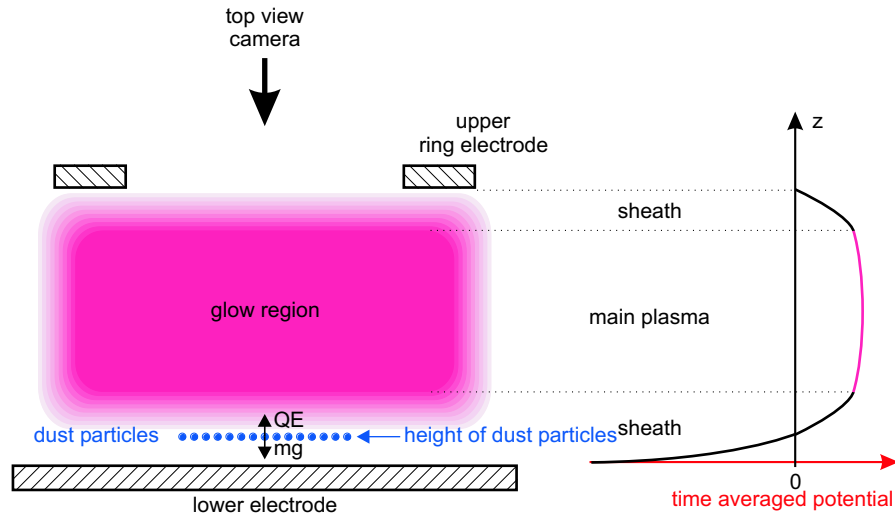


Figure 2.2: Sketch of particle levitation and confinement. A dc electric field in the lower sheath levitates particles against the downward force of gravity. A slight curvature of the sheath, not shown here, provides radial confinement. The dc electric fields are much stronger in the sheath than in the main plasma (glow region), as indicated by the electric potential sketched on the right.

as was discussed in Chapter 1. The depth of this curved sheath can be enhanced to provide more radial confinement by using a cylindrical depression in the lower electrode, as I do in Chapters 4 and 5, but not Chapter 3. This depression can be seen in Fig. 1.2. Because of the radial confinement, dust particles do not escape in the radial direction but instead concentrate above the center of the lower electrode. They repel each other because they are all negatively charged, so that they do not all occupy the same equilibrium positions. Thus, the particles distribute themselves spatially, as in Fig. 1.3, with a typical interparticle distance of about 0.5 mm, which is approximately equal to the Debye length in the sheath.

The polymer particles I introduce in the plasma can form a single-layer suspension. Due to the large diameter of the electrode, 22.2 cm, and the weak horizontal (radial) confinement compared to the much stronger vertical confinement, particles tend to form a single layer which can be as large as 5 to 10 cm in diameter, before a

second layer forms. In my single-layer dusty plasma suspension, the typical particle number is about 10,000. However, if I add more particles, eventually they would fill a second layer. Additionally, my particles are monodisperse in size. If instead I were to use polydisperse particles, the heavier particles would be levitated at a lower height, and multiple layers would form.

Without any other perturbations, the dust particles self-organize in a triangular lattice with six-fold symmetry, as I will describe later. Because of the strong vertical confinement due to the dc electric field in the sheath, particle motion is essentially 2D, with negligible out-of-plane displacements and no buckling of the particle layer.

In my experiments, I mainly focus on observing the particles, particularly those in the central portion,  $\approx 3$  cm, of the suspension. There are at least two advantages in studying dynamics in this central region only. First, the radial confinement is nearly flat for the lower electrode with a larger diameter, 22.2 cm. Second, the interparticle distance is relatively uniform in the central region.

#### 2.1.4 Laser manipulation

Because of the advantages of laser manipulation, as mentioned in Sec. 1.1.6, I use a powerful laser to manipulate 2D dusty plasma suspensions. The apparatus is sketched in Fig. 2.3. The manipulation laser is a 532-nm Verdi solid state laser operated steady state, and its power can be adjusted up to 18 W. The 532-nm laser beam is split into two beams, which are directed by mirrors so that they enter windows on opposite sides of the plasma chamber. Thus, these two beams are used to manipulate the dusty plasma symmetrically from two opposite directions. For each beam, a pair of galvanometer scanning mirrors allow pointing or scanning the beam in the  $x$  and  $y$  directions. This is done by controlling the angle of the scanning mirror using a servo that responds to an applied voltage. By applying a desired

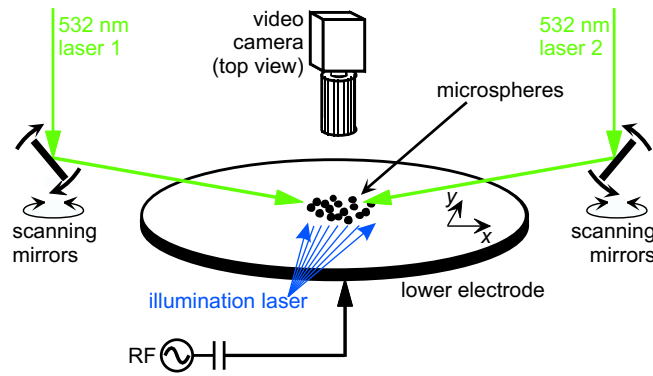


Figure 2.3: Particle imaging and manipulation. A vacuum chamber, shown in Fig. 2.1, encloses the lower electrode. The primary diagnostic is video microscopy using a top-view camera with an illumination laser. Another laser, used to manipulate particles, is directed from two sides using scanning mirrors.

waveform to the scanning mirrors, the laser beams are directed in a desired pattern in the chamber. When a dust particle is struck by a laser beam, it will be pushed by the momentum of the photons, resulting in the radiation pressure force. The beams intercept the single layer of particles obliquely, at an angle of  $6 - 9^\circ$ , so that the force is primarily in the horizontal direction.

### 2.1.5 Data recording and laser illumination

I use three cameras during my experiments. Two cameras view from the top: one is a narrow field of view (FOV) camera that provides my main data, and the other is a wide FOV that allows me to monitor the entire suspension. Examples of images from the narrow FOV camera are shown in Figs. 1.3 and 2.4. The other camera views from the side with a wide FOV. The narrow FOV camera yields a video (a sequence of video frames) that is recorded directly on a computer. Each video frame is recorded as a bit-map image. In these experiments, I use two cameras for the narrow FOV: a 14-bit cooled CCD camera, model PCO model 1600, which can be operated at 55 frames per second; and a 12-bit high-speed CMOS camera, Phantom

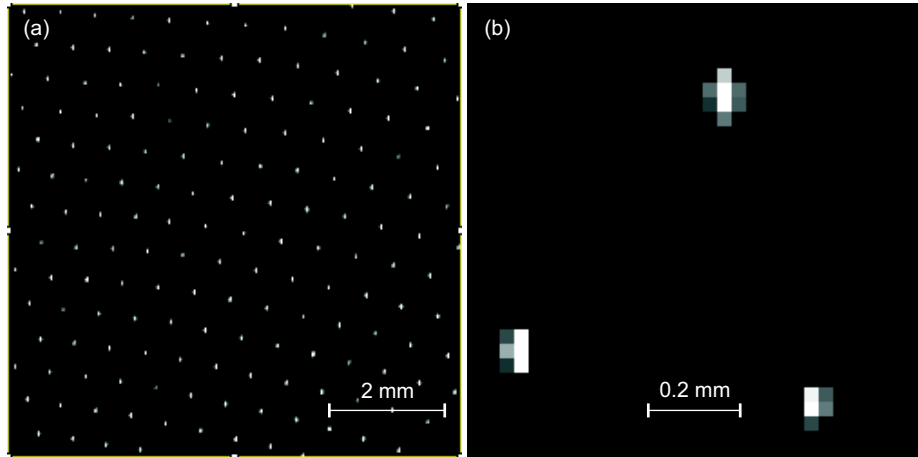


Figure 2.4: Experimental bitmap images of a single-layer suspension of microspheres in a dusty plasma. Each bright spot corresponds to one particle. Here, (a) is  $\approx 1/12$  of the original image from a narrow FOV camera (Phantom v5.2), and (b) is a magnified view, showing that a bright spot fills several pixels. Spot size depends on such factors as camera type and focusing. A particles position is calculated as the bright spots center.

model v5.2. The narrow FOV camera typically views a region of ( $30 \text{ mm} \times 20 \text{ mm}$ ), containing about 1500 particles. The wide FOV top and side view cameras are both NTSC analog video cameras.

For these three cameras, I use three laser sheets, each with a different wavelength, to illuminate the particles in the suspension. The illumination lasers are a 488-nm argon laser or a 577-nm solid state laser for use with the narrow FOV camera, a 632-nm He-Ne laser for the wide FOV top view camera, and a red diode laser for the side view camera. The cameras are equipped with optical bandpass filters that pass the desired wavelength corresponding to a illumination laser, while blocking glow emission and other undesired light at other wavelengths.

I use two methods to form a laser sheet for illumination. When videos are recorded at 55 frames per second, as in Chapters 3 and 4, the laser sheet is generated by rastering the laser beam. The laser is rastered with a scanning mirror

synchronized to the narrow FOV camera, providing a single sweep of laser across the suspension. If I use a high speed camera, as in Chapter 5, the mechanical response of the scanning mirror is not fast enough. Instead, I use a cylindrical lens to disperse the laser beam into a sheet. A cylindrical lens is also used to disperse a He-Ne laser for the wide FOV camera. Both of these illumination lasers (for the two top view cameras) are focused using a telescope with a pair of plano-convex lenses to provide a narrow waist inside the chamber. For the side view, the diode laser is sufficiently wide to illuminate the single-layer suspension without any cylindrical lens.

## 2.2 Data analysis method

### 2.2.1 Particle tracking velocimetry

During my experiments, I record a sequence of bit-map images using the narrow FOV top-view camera. Each image corresponds to a video frame. This sequence of frames is a movie of typically  $> 5000$  frames. An example image from my experiment is shown in Fig. 2.4(a). An image of one particle fills  $\approx 10$  pixels, as shown in Fig. 2.4(b). The  $x - y$  coordinates, or the position, of each particle can be calculated based on the intensity of those bright pixels using the moment method, which will be described in detail in Chapter 7, where I present my advances in the state of the art in this method. After calculating the particle positions in each frame, I can track particles from one frame to the next, and then calculate their velocities as  $v_{i,x}(t + \delta t/2) = [x_i(t + \delta t) - x_i(t)]/\delta t$ . With the calculated positions and velocities of all particles, I can perform structural and dynamical analysis, which I will discuss next.

### 2.2.2 Kinetic temperature

As an important parameter of my 2D dusty plasma suspension, the kinetic temperature can be calculated using

$$k_B T = \frac{1}{N} \sum_{i=1}^N \frac{1}{2} m [(v_{i,x} - \bar{v}_x)^2 + (v_{i,y} - \bar{v}_y)^2], \quad (2.1)$$

where  $N$  is the number of particles analyzed,  $\bar{v}_x$  and  $\bar{v}_y$  are the center-of-mass velocities. The kinetic temperature  $T$  of the dust particle motion is not a thermodynamic temperature. The plasma is a non-equilibrium system, so that  $T$  is different from the temperatures of other constituents in the plasma including the neutral gas, electrons, ions. It is also different from the temperature of the polymer material of the particles themselves.

### 2.2.3 Structural analysis

As compared to 3D systems, 2D systems are convenient for experimenters because of the inherently 2D-nature of video microscopy images. Thus, a particle's coordinates can be determined completely from the images.

The structural measures that I use include the pair correlation function  $g(r)$ , which is the same function as in the BBGKY hierarchy for weakly-coupled plasmas [71]. Additionally, I also use Voronoi diagrams and the bond-angular-order parameter  $G_\theta$  [72, 73]. I will introduce only Voronoi diagrams here; the other two will be discussed in later chapters when I use them.

A Voronoi diagram is computed mathematically from positions of particles. Nearby pairs of particles are identified; these pairs are said to be connected by “bonds”. The most common mathematical method for computing these pairs is Delaunay triangulation [74]. Next, a corresponding Voronoi diagram [32] is computed by drawing perpendicular lines to bisect all bonds. If a particle has six nearest neighbors, it will be surrounded by a six-sided polygon. Figure 2.5 illustrates how

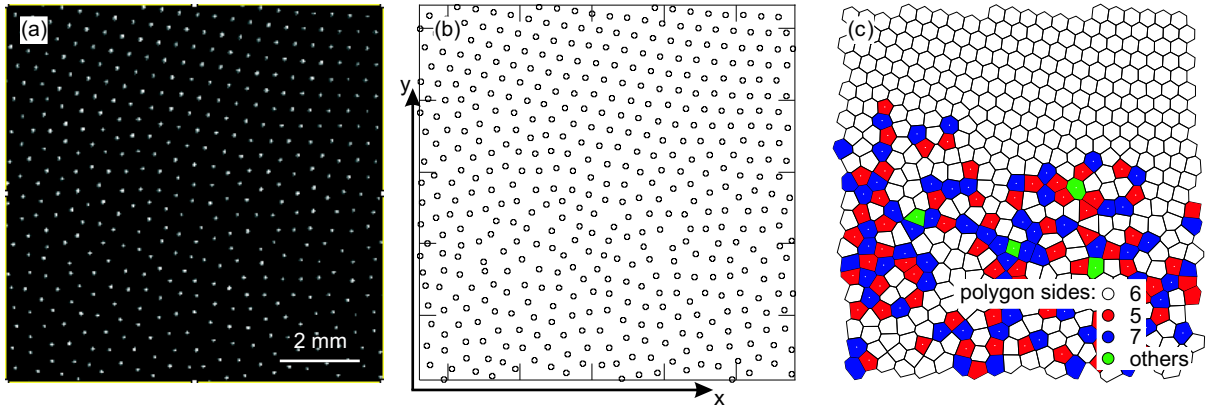


Figure 2.5: Video microscopy image (a), and the corresponding particle positions (b) and Voronoi diagram (c). The suspension has the structure of an ordered solid lattice in the top half of each panel, but a disordered liquid in the bottom half. Defects in a lattice are identified in a Voronoi diagram as non-six-sided polygons, which are shown in color. The original video microscopy image was much larger than the portion shown in panel (a). These data are from an experiment reported in Chapter 4.

a Voronoi diagram is calculated from an image from my experiment.

Voronoi diagrams are widely used to identify disorder in the relative positions of particles [32, 74]. The type of disorder that it indicates is a lattice defect. For a defect-free 2D crystal, the Voronoi diagram would include only six-sided polygons. When defects are present, they are identified by the presence of non-six-sided polygons, as in Fig. 2.5(c), where I use different colors to indicate the non-six-sided polygons. To reduce the information in a Voronoi diagram to a single parameter, I calculate the defect fraction as the ratio of the areas of all non-six-sided polygons to the area of the entire Voronoi diagram. The defect fraction can vary from zero for a defect-free crystal to  $\approx 0.3$  for a liquid.

#### 2.2.4 Dynamical analysis

Using the time series of particle positions and velocities that results from my image analysis, I can perform many kinds of dynamical analysis, in addition to calculating the kinetic temperature.

For a 2D dusty plasma suspension, the collective oscillation of particles can be characterized by the nominal 2D dust plasma frequency  $\omega_{pd}$ , which can be expressed as  $\omega_{pd} = (Q^2/2\pi\epsilon_0ma^3)^{1/2}$  [75]. The concept of  $\omega_{pd}$  is comparable to the plasma frequency, except that there is no resonance in the motion of particles at  $\omega_{pd}$  if the particles are constrained to a single layer as they are in my experiments.

Another important time scale for collective particle motion is the period of oscillation corresponding to the Einstein frequency,  $\omega_E$ . Here  $\omega_E$  has the usual meaning: it is the hypothetical oscillation frequency that a particle's motion would have in a cage formed by nearby particles, if all the other particles were stationary [75].

Collective dynamics of 2D dusty plasmas also include sound waves, due to Coulomb interparticle interaction. The wave spectra can be calculated from the motion of particles [27], using a Fourier transformation of particle currents computed from particle positions and velocities [76]. My 2D strongly-coupled dusty plasmas sustain both longitudinal and transverse sound waves. In general, transverse sound waves occur in solids and to a lesser extent in liquids as well [77], but not in gases such as weakly-coupled plasmas.

The dispersion relations for longitudinal and transverse waves can be measured explicitly from the wave spectra. This is done by identifying the peaks of the energy vs. frequency curve for each wavenumber. This experimental dispersion relation is computed separately for the longitudinal and transverse waves.

I use the experimentally measured dispersion relation to determine several

parameters of the dusty plasma. I generally do this using images recorded for a suspension in a highly-ordered crystalline lattice, before applying any laser manipulation. Comparing the measured and theoretical dispersion relations, and varying values of  $\kappa$  and  $\omega_{pd}$  in the theoretical expression, I can find the values of  $\kappa$  and  $\omega_{pd}$  that best fit the experimental data. This fitting is done using a plot of chi-square as a function of the fit parameters  $\kappa$  and  $\omega_{pd}$ . Other parameters for the dusty plasma suspension, such as  $\lambda_D$  and  $Q$ , are then calculated from  $\kappa$  and  $\omega_{pd}$ . Additionally, the longitudinal and transverse sound speeds can also be measured from the slope the dispersion relation,  $\partial\omega/\partial k$  as  $k \rightarrow 0$ .

As a note regarding terminology, it is useful to know that in the field of condensed matter physics, the longitudinal and transverse waves described above are called phonons. In later chapters, I will refer to my “wave spectra” as “phonon spectra.”

### CHAPTER 3

#### SOLID SUPERHEATING IN DUSTY PLASMA

Unlike weakly-coupled plasmas, strongly-coupled plasmas can exhibit solid-like or liquid-like behavior, and they have a phase transition between the solid and liquid phases. To distinguish solids and liquids, strongly-coupled dusty plasma experimenters rely on measurements of particle positions, which are then used to compute structural measures. These methods are well-suited for strongly-coupled plasmas because of the importance of the Coulomb interactions of discrete particles. As a solid is heated, its temperature increases and it becomes more disordered, but these do not necessarily happen simultaneously. Instead, if heating is applied rapidly enough, the strongly-coupled plasma can retain a solid-like structure at a temperature well above the melting point, as I demonstrate for the first time. This phenomenon, termed solid superheating, is very rare in all fields of physics, having been observed previously only with a few specially-prepared samples of metal or with exotic heating methods employing ultra-fast lasers.

It is demonstrated experimentally that strongly-coupled plasma exhibits solid superheating. A 2D suspension of microspheres in dusty plasma, initially self-organized in a solid lattice, was heated and then cooled rapidly by turning laser heating on and off. Particles were tracked using video microscopy, allowing atomistic-scale observation during melting and solidification. During rapid heating, the suspension remained in a solid structure at temperatures above the melting point, demonstrating solid superheating. Hysteresis diagrams did not indicate liquid supercooling in this 2D system.

The results in this chapter correspond to Y. Feng, J. Goree, and B. Liu, “*Solid superheating observed in two-dimensional strongly coupled dusty plasma*,” Physical Review Letters, Vol. 100, article number 205007 (2008), and Y. Feng, B. Liu, and

J. Goree, “*Rapid heating and cooling in two-dimensional Yukawa systems,*” *Physical Review E*, Vol. 78, article number 026415 (2008).

### 3.1 Introduction

Strongly-coupled plasma is a collection of free charged particles where the Coulomb interaction with nearest neighbors is so strong that particles do not easily move past one another [7]. Plasma can become strongly coupled due to high density as in neutron stars [8], low temperature as in pure ion plasma [10], or high particle charge as in dusty plasma [31]. Dusty plasma is partially ionized gas containing micron-size particles of solid matter. Dusty plasmas have been used in the study of phase transitions [19, 20, 23, 32, 39], waves [27], transport [28, 29, 30, 31], and liquid microstructure [56].

Materials like water can exist as superheated solid [36] or supercooled liquid [78]. These are, respectively, a solid at temperatures above the melting point [33], and a liquid below the melting point [79]. Observing solid superheating was once thought to be impossible [34], but it is now practical due to new instrumentation for heating [36, 35] or fabricating special samples [37, 38].

I find that the literature for solid superheating lacks experiments with atomistic-scale observation. Here, the term “atomistic-scale” indicates that molecules or their equivalent are imaged or tracked individually. Most solid superheating experiments use external measurements like diffraction in metals [35, 37, 38] or optical absorption in ice [36], or electrical measurements for Abrikosov vortices [80]. In contrast to the experimental literature, theory for solid superheating includes simulations that track individual molecules [33]. Experiments with colloidal suspensions include direct imaging of particles in supercooled liquids [17, 81], but apparently not superheated solids.

The literature for solid superheating also lacks experiments with strongly-coupled plasma. Experiments with strongly-coupled plasma have demonstrated solid and liquid [19, 20, 23, 32, 56] behavior, and recently supercooled liquid as well [39], but not superheated solid.

Liquid supercooling, unlike solid superheating, is easily achieved in many three-dimensional (3D) systems, but it is an open question whether supercooling ever occurs in one-component 2D systems [17]. Experiments are needed to answer this question. Candidate systems for 2D experiments include electrons on a liquid helium surface [15], granular fluids [18], colloids [17], and dusty plasmas [31].

Here, I seek answers to three questions. First, can strongly-coupled plasmas exhibit solid superheating? Second, can solid superheating experiments be performed using direct imaging of particles? Third, does my one-component 2D system exhibit liquid supercooling?

### 3.2 Dusty plasma experiment

I report experiments with a 2D suspension of particles in a dusty plasma, which is a kind of strongly-coupled plasma. Highly-charged particles, which are polymer microspheres, are immersed in partially ionized argon gas. Electrons and positive ions are collected by a particle, giving it a large negative electric charge. In a plane perpendicular to ion flow, particles interact through a repulsive Yukawa potential  $U(r) = Q^2(4\pi\epsilon_0r)^{-1}exp(-r/\lambda_D)$  [13].

My particles experience multiple forces, the largest arising from gravity, electric fields, gas friction, and laser radiation pressure. The apparatus [31] provides a plasma with a sheath above a lower horizontal electrode. This sheath has electric fields that levitate and confine charged particles, so that they are suspended as a single layer. Particles have a diameter  $4.83\pm 0.08 \mu\text{m}$  [14] and mass  $m = 8.93\times 10^{-14}$  kg. To partially ionize 7 mTorr argon gas, I used radio-frequency power at 13.56 MHz,

with an amplitude of 97 V peak-to-peak. Particles experience gas drag with a coefficient of  $2.1 \text{ s}^{-1}$  [14] when they move.

As in colloidal suspensions, my particles can self-organize in a crystal. Unlike colloids, however, my particles are underdamped, and they can be heated without heating the gas or ions. In my experiment, particle motion was essentially 2D, with negligible out-of-plane displacements and no buckling of the particle layer.

Video microscopy allows imaging this 2D suspension at an atomistic scale, so that I can track particles and measure their individual positions and velocities in each video frame. Viewing from above, I recorded a movie of 5575 frames at 55 frames per second with a total field-of-view (FOV) of  $34.2 \times 25.6 \text{ mm}^2$ . I analyzed data in a  $30.7 \times 22.2 \text{ mm}^2$  sample region in the center of FOV, which included about 1000 of the  $> 5000$  particles in the suspension. The particle spacing was characterized by a Wigner-Seitz radius [31] of 0.45 mm. In each frame, I measured positions of particles and tracked their motion. The particle positions were used for three structural indicators, described below. For each video frame, the 2D particle velocities  $v_i$  were used to calculate the temperature  $T = (\sum_{i=1}^N m(v_i - \bar{v})^2/2)/Nk_B$ , where  $N$  is the number of particles analyzed, and  $\bar{v}$  is the center-of-mass velocity. This kinetic temperature is different from the temperatures of the other constituents including the neutral gas, electrons, ions and the polymer material of the particles themselves. My velocity distribution function contained some non-Maxwellian features, as in [82], including a peak at  $v_y^2 = 5 \text{ (mm/s)}^2$  as in Fig. 4(c) of [82]. Particle velocities were also used in the wave-spectra analysis method [27] to determine the particle charge  $Q = -(4360 \pm 440) e$  and the screening length  $\lambda_D = (0.65 \pm 0.15) \text{ mm}$ .

At first, without additional heating, the suspension has the solid structure of a triangular lattice with six-fold symmetry. Due to its extreme softness and the

stresses applied by confining electric fields, this solid is never defect-free. Even at the lowest temperatures, it has some defects, arranged in strings defining domain walls [23].

My laser heating method [31, 82] allows adjusting the kinetic temperature of particles by varying the laser power. This does not affect the plasma environment or particle charge, unlike previous methods [19, 20, 23, 32]. Random kicks are applied through radiation pressure from a pair of 532-nm laser beams that are rastered across the suspension in a Lissajous pattern with frequencies  $f_x = 48.541$  Hz and  $f_y = 30$  Hz in a rectangular region slightly larger than the FOV. During laser heating, the suspension is a driven-dissipative system [31]. In steady state, the particle kinetic temperature is determined by a balance of external laser heating and frictional drag cooling from neutral gas. Due to the orientation of the laser beams, the temperature is higher in the  $x$  direction [82] by a ratio of 2 during steady heating, and increasing monotonically from 1 to 2 during rapid heating.

To provide conditions favorable for solid superheating or liquid supercooling, I switch the laser on and off abruptly, so that the temperature will change suddenly. In my rapid heating and cooling experiment, the pair of 532-nm laser beams is ramped between 0 and 7 W in 1 or 2 sec, for rapid cooling and heating, respectively. This results in a temperature that changes at a rate  $> 20\,000$  K/s during rapid heating.

I measure three indicators of microscopic structure in addition to the temperature time series. First, I identify defects and calculate defect area fraction by calculating Voronoi diagrams [32]. Second, I measure short-range translational order using the height of the first peak of the pair correlation function  $g(r)$  [82], which is larger for solids than for liquids. Third, I measure the short-range orientational order using the bond-angular-order parameter,  $G_\theta$  [72], which varies from zero for a gas to unity for a perfect crystal. For a solid,  $G_\theta$  is less than unity if there are

defects.

### 3.3 Results

In addition to my measurements with rapid heating and cooling, I also performed slower heating and cooling to measure the melting point, in the range 4600 – 5600 K. This is consistent with the prediction  $4600 \pm 1000$  K of 2D Yukawa simulations [73] using my measured values of inter-particle spacing,  $Q$  and  $\lambda_D$ ; the error bar arises from uncertainties in  $Q$  and  $\lambda_D$ .

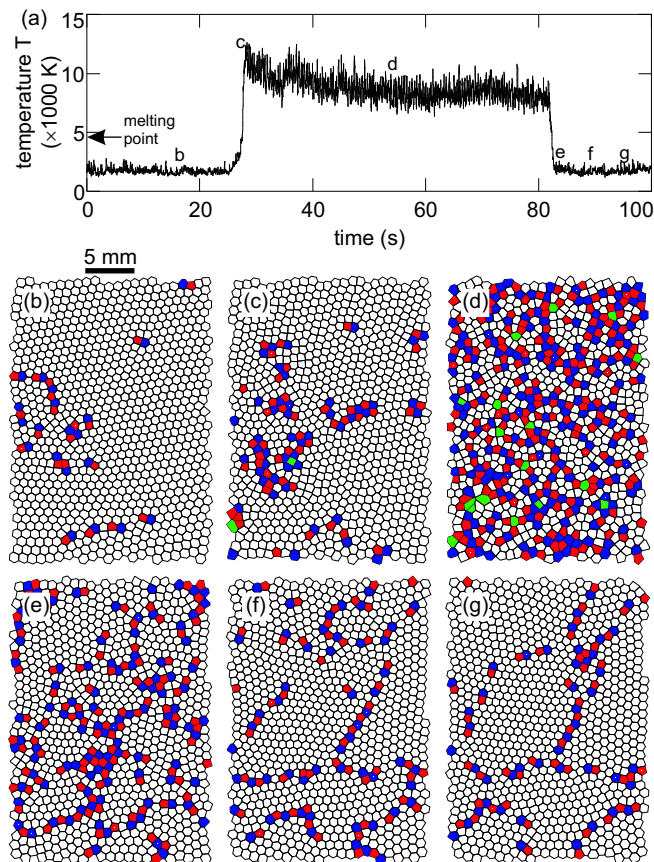


Figure 3.1: Temporal development of temperature and structure. (a) Time series of particle kinetic temperature  $T(t)$ , when laser heating was switched on and then off. Times marked b-g correspond to panels below. (b)-(g) Voronoi diagrams, showing defects in color. Polygons indicate the number of nearest neighbors of a particle: red (5), white (6), blue (7), and green (others).

My main results are time series of temperature and the microscopic structure indicators. I applied rapid heating, followed by 55 s of steady conditions and then rapid cooling. The temperature time series, shown in Fig. 3.1(a), is marked at six times corresponding to the Voronoi diagrams in Fig. 3.1(b)-(g). Time series are presented in Fig. 3.2 for the structure indicators: defect fraction,  $g(r)$  peak value, and  $G_\theta$ . I combine time series data to yield a hysteresis diagram, Fig. 3.3. Details are presented next.

The sequence of Voronoi diagrams, Fig. 3.1(b)-(g), reveals solid superheating. Before heating Fig. 3.1(b), the suspension has a solid polycrystalline structure, with domains as large as the sample region shown here. In the most significant panel in this sequence, Fig. 3.1(c), at  $T > 9000K$  near the end of rapid heating, the structure remains a polycrystalline solid, with only a modest increase in defects mostly near the previous defect locations. Since this is a solid structure, while at the same time the temperature is above the melting point, I conclude that it is a superheated solid. Later, in steady heating, Fig. 3.1(d), the structure is liquid, as indicated by the numerous defects and lack of large crystalline domains. Immediately after rapid cooling, Fig. 3.1(e), defects have diminished greatly. Five and ten seconds after rapid cooling, Fig. 3.1(f) and 3.1(g), respectively, the suspension is again a polycrystalline solid, with crystalline domains separated by string-shaped defect clusters. These crystallites grow bigger by merging neighbors together gradually in a slow recrystallization process [23].

Time series for microscopic structure indicators, Fig. 3.2, reveal different time scales. In order to compare these time scales, I rescaled all four variables in Fig. 3.2(d) to vary from 0 (before rapid heating) to 1 (during steady heating) using a linear function with a slope and intercept for each variable. During cooling, structure indicators change at different rates: translational order changes fastest, and

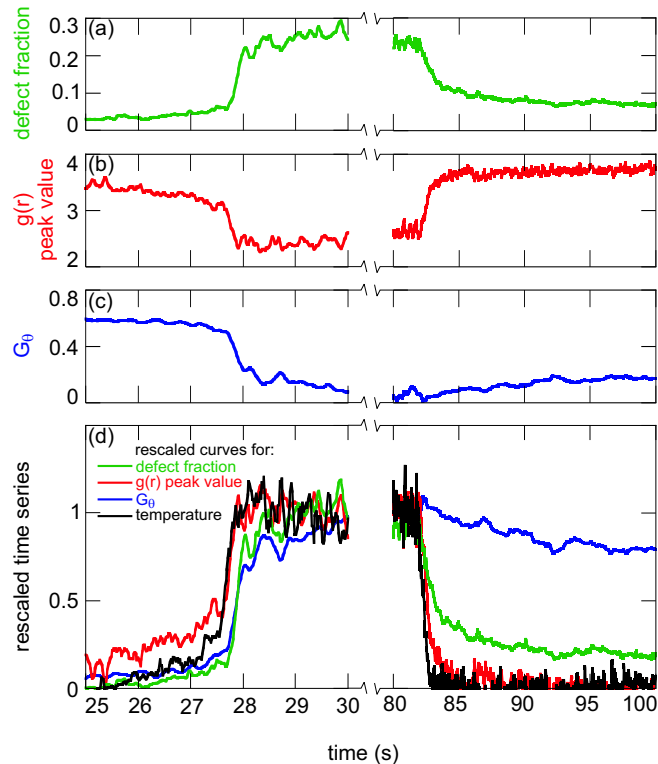


Figure 3.2: Time series of structure indicators and temperature. (a) Defect fraction (the area of defective polygons, as a fraction of total area, in Voronoi diagrams as in Fig. 3.1). (b) Height of the first peak of the pair correlation function  $g(r)$ . This is an indicator of short-range translational order. (c)  $G_\theta$  [72], an indicator of short-range orientational order. This can vary from zero for a gas to unity for a perfect crystal. (d) Time series for the three structure indicators and temperature, rescaled to vary from zero (for a solid before heating) to unity (for a liquid during heating). Data are smoothed over 3 frames.

orientational order slowest, consistent with the data of [23]. I also measured the defect fraction, which changed at a rate between the other two. My experimental method also allows measurements during rapid heating, where I observe a delay in the response of the structure as the temperature increases. This delay is shortest ( $\leq 0.04$  s) for translational order, and longer ( $\approx 0.2$  s) for defect fraction and orientational order.

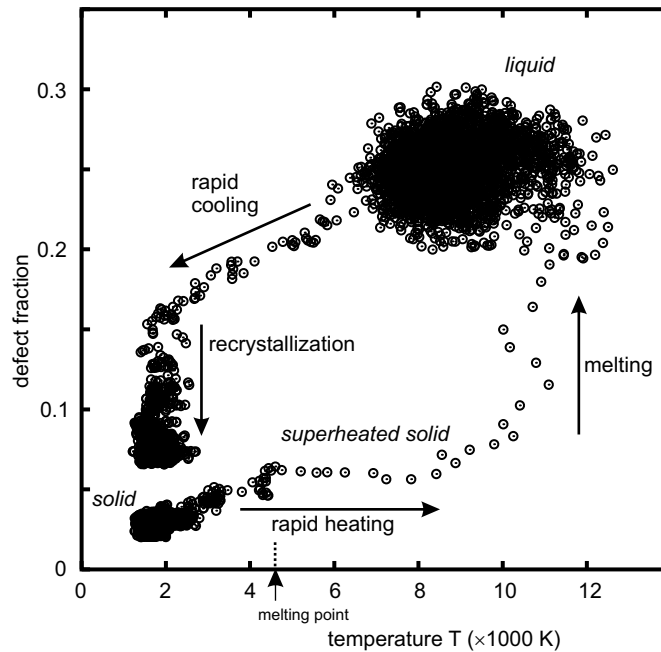


Figure 3.3: Hysteresis diagram made by combining data from Figs. 3.1 and 3.2. The time interval between data points is 0.018 s. Initially, I had a solid, lower left corner. Then rapid heating was applied, causing a temperature increase across the melting point without much change in structure, the lower horizontal line of data points. This is a signature of solid superheating. Next, the superheated solid melted, as shown by the nearly vertical line of data points on the right. The resulting liquid in the upper right corner had a high defect fraction. Later, during rapid cooling, defect fraction dropped dramatically as the temperature declined. Finally, the suspension slowly recrystallized.

Hysteresis diagrams, like Fig. 3.3, are traditional tools for studying phase transitions [37, 83]. Hysteresis arises because structure does not respond immediately to a change of temperature. This can occur either due to a delayed response as in the case of my rapid heating, or a gradual response as for my rapid cooling. In previous solid superheating experiments, the vertical axis was typically from X-ray diffraction [37]. Here I use direct imaging of particles to yield an indicator of microscopic structure for the vertical axis of a hysteresis diagram, Fig. 3.3. My hysteresis diagram allows a useful interpretation: a signature of solid superheating or liquid

supercooling would be a horizontal row of data points across the melting point. Such a horizontal row would indicate a temperature that has changed without a corresponding change in structure.

My chief conclusion, an observation of solid superheating, is based on two results. First, Voronoi diagrams compared before and after rapid heating indicate solid superheating, as described above. Second, the hysteresis diagram, Fig. 3.3, has the signature of solid superheating: a nearly horizontal row of data points, which can be seen near the bottom of the graph.

After the superheated solid is formed, it then melts, as indicated by a proliferation of defects. Because the substance being melted is a superheated solid, the melting occurs without much further temperature increase, yielding a nearly vertical line of data points in Fig. 3.3. The lifetime of the superheated solid and the duration of the subsequent melting are both about 0.25 s.

I also conclude that my rapid cooling did not produce a supercooled liquid. The rapid-cooling portion of Fig. 3.3, lacks the signature of a supercooled liquid. Instead, the defect fraction drops dramatically during the temperature decrease. Additionally, the Voronoi diagrams for rapid cooling, Fig. 3.1(e)-(g), lack a liquid structure.

My observation that I did not form a supercooled liquid might be attributable to the low dimensionality of the experiment. For 3D systems, many examples of materials, including dusty plasma [39], can be quenched to form supercooled liquids or glasses. For 2D systems, however, forming a supercooled liquid or glass seems to be difficult [17]. The role of dimensionality in transitions to a glassy or supercooled state remains an important question [39, 84]. A previous 2D experiment addressing this question was performed using colloidal suspensions [17], which have much higher friction than in my suspension.

The solid superheating had a limited duration, which I interpret as an indication that it is a kind of transient solid superheating. In general, one could identify solid superheating as being either transient or metastable, depending on the duration of the solid structure after increasing the temperature above the melting point. The distinction between transient and metastable superheating has been previously mentioned in a review of the literature [85]. For my experiment, I judge the duration of the superheated solid by comparing its lifetime of about 0.25 s to another important time scale for particle motion: the period of oscillation corresponding to the Einstein frequency,  $\omega_E$ . Here  $\omega_E$  has the usual meaning: it is the oscillation frequency that a charged particle's motion would have in a cage formed by all the other particles, if all the other particles were stationary. The Einstein frequency for my experiment can be estimated from a combination of my experimental measurement of the plasma frequency,  $\omega_{pd} = 33.3 \text{ s}^{-1}$ , and a previous simulation that provided a relationship between  $\omega_{pd}$  and  $\omega_E$  [75]. This yields an estimate for in my experiment of  $\omega_E = 0.612 \omega_{pd} = 20.4 \text{ s}^{-1}$ . The corresponding period of oscillation for the charged particle in the experiment is  $\tau_E = 2\pi/\omega_E = 0.31 \text{ s}$ . Comparing now to the experimentally observed lifetime of about 0.25 s for the superheated solid, I find that the lifetime was only about one oscillation period, before melting occurred. Therefore, I interpret my experimental results as an indication of transient, not metastable superheating.

The underlying reason for the solid superheating in the experiment is simple to understand, now that the time scales have been determined. Initially, in the solid below the melting point, particles are caged by their nearest neighbors. Caged particle motion in a solid consists mainly of oscillations, with a turning point located well within the cage. In a full period of oscillation, characterized by a  $\tau_E$ , a particle's trajectory has two turning points. As rapid heating is suddenly applied, particles

in the cage are accelerated, the cage distorts as other particles are also accelerated, and the enclosed particle can eventually decay and thereby generate a defect. In the experiment, the time indicated by the hysteresis diagram for this decaying to occur is about 0.25 s, about the same as  $\tau_E = 0.31$  s. Comparing these two values indicates that after sudden heating is applied, a particle typically decays after bouncing about twice in the cage. This short-lived stage of bouncing about twice before decaying corresponds to the transient superheated solid.

During the experiment, the single-layer particle suspension was not constrained in its size. In principle, its areal number density could vary in time. I calculated a time series for the areal number density, and I found that there was no significant expansion as the temperature increased. The areal number density remained constant within 1.5% during the experiment [86], despite very large temperature changes of an order of magnitude. It is interesting that despite the extreme softness of this suspension, its volume varies so little with temperature.

One feature of the hysteresis diagram that requires explanation is the gap in data points at the lower left of Fig. 3.3. This gap is due to the finite data-recording time in the experiment. After the initial rapid cooling, a very slow recrystallization takes place. During the recrystallization, crystalline domains gradually grow in size by merging with neighboring domains. The merging process is slow because a domain must rotate until its orientation aligned with a neighboring domain. This process becomes increasingly slow as the remaining domains become larger, as can be seen in the Voronoi movie from the experiment [86]. The camera in the experiment had a finite memory, allowing the recording of a movie limited to 100 s duration for the entire experiment.

Previous to my experiment [86], Knapek *et al.* reported another experiment [23] to study the recrystallization during cooling. They used a similar dusty

plasma with a single-layer suspension of microspheres. They heated their suspension suddenly by applying an electrical pulse to wires. Using video microscopy, particle motion was recorded well after the pulse was completed, so that the experimenters observed the cooling process, but not the heating process. As in my experiment [86], this cooling process included a rapid cooling followed by a slow recrystallization. Like us, they reported time series for temperature and defect fraction; they also reported correlation lengths as measures of orientational and translational order, serving roles similar to  $G_\theta$  and height of the first peak of  $g(r)$ . They found that temperature decreases more rapidly than defect fraction [23], a result that I verified in [86]. They also found that orientational order drops much more slowly than translational order, and attributed this to the presence of domains in various orientations during the slow recrystallization process [23]. My experiment differed by using laser heating, which did not disturb the particle layer severely. Because of this, I was able to record particle motion during both heating and cooling, allowing us to prepare hysteresis diagrams.

In addition to my experiment, I also performed a numerical simulation. I found conditions that result in the same signature of transient solid superheating as in the experiment, as I report in [87].

### 3.4 Conclusion

In conclusion, firstly I have shown that strongly coupled plasmas can exhibit solid superheating. This suggests investigating superheating in other solid strongly-coupled plasmas that can melt, like laser-cooled ions [10] and the crust of neutron stars [8]. Secondly, I have demonstrated an experimental method of studying solid superheating using direct imaging of particles. These two results are apparently the first of their kind. Thirdly, I found a lack of liquid supercooling in my 2D system.

## CHAPTER 4

### EVOLUTION OF SHEAR-INDUCED MELTING IN DUSTY PLASMA

Unlike weakly-coupled plasmas, strongly-coupled plasmas can exhibit melting, i.e., a solid-liquid phase transition, as was mentioned in Chapter 4. In general, melting of any kind of solid can be induced by many ways, including applying shear. All previous studies of shear-induced melting, for all physical systems, were carried out only under steady-state conditions. Here, I report the first experiment, both for strongly-coupled plasmas and for all other physical systems as well, of sudden shear-induced melting. Strong shear will be applied suddenly to a strongly-coupled plasma in a solid phase, to induce and observe sudden shear-induced melting. This experiment requires applying shear on a time scale as fast as internal time scales for the sample, such as  $\omega_{pd}^{-1}$ , and an ability to observe order or disorder on the same time scale. Strongly-coupled dusty plasmas allow this, with laser manipulation to provide sudden shear, and video microscopy to observe order and disorder, both with the required fast time scales compared to particle motion. A dusty plasma also allows underdamped wave propagation as a mechanism for energy propagation, so that I will investigate whether waves might account for the speed of melting. This experiment requires analyzing both structure at an atomistic scale and dynamics of discrete particles, which are made possible by video microscopy.

The spatiotemporal development of melting is studied experimentally in a 2D dusty plasma suspension. Starting with an ordered lattice, and then suddenly applying localized shear, a shear flow develops. A transition between two melting stages is observed before a steady state is reached. Melting spreads with a front that propagates at the transverse sound speed. Unexpectedly, coherent longitudinal waves are excited in the flow region.

The results in this chapter correspond to Y. Feng, J. Goree, and B. Liu, “*Evolution of shear-induced melting in a dusty plasma,*” Physical Review Letters, Vol. 104, article number 165003 (2010).

#### 4.1 Introduction

Applying shear can induce melting [41, 42, 43, 44, 45]. Experiments have been reported in soft materials: colloidal suspensions [40, 46], two-dimensional (2D) electron crystals with magnetic field [47], foams [48], polymer glasses [49] and dusty (complex) plasmas [50]. Most of these studies were done with a steady application of shear.

If shear were instead applied suddenly, one could investigate the spatiotemporal development of shear-induced melting. However, there have been no such experiments reported in any physical system to my knowledge.

In addition to melting, another result of sudden application of shear is wave excitation. When strong shear is applied to a 2D crystal lattice, plastic deformation occurs, and this can cause melting [50]. When the applied shear is weaker and deformation is elastic, transverse waves (phonons) propagate through the lattice [26]. Another type of wave is longitudinal. To my knowledge, at least within the literature for dusty plasmas, there have been no reports of the excitation of coherent *longitudinal* waves due to the application of *shear* in either the elastic or plastic regimes.

Here I seek answers to three questions. First, can coherent longitudinal waves be generated by applying shear? Second, when shear is applied suddenly, and melting occurs, what is the spatiotemporal development? Third, is there a melting front, and how does it spread?

Physical systems that allow motion essentially on a 2D plane include a Wigner lattice of electrons on a liquid-He surface [47], ions confined in a Penning trap [88],

colloidal suspensions [89], granular fluids [18], vortex arrays in the mixed state of type-II superconductors [16], and dusty plasmas levitated in a single layer [55, 86].

Melting of 2D systems has a different mechanism than for 3D systems [89]; it is sometimes termed an order-disorder transition [90]. Order and disorder are characterized by measures of structure. For example, the local six-fold bond-orientational order  $|\phi_6|$  [42, 44, 91] measures local order, while global order can be characterized by the abundance of defects [86, 90], which are non-hexagonal Wigner-Seitz cells in Voronoi diagrams [44, 86].

## 4.2 Dusty plasma

Dusty plasma is partially ionized gas containing micron-size particles of solid matter [86]. Dusty plasmas allow atomistic scale observation of dynamics by tracking particles with video microscopy, and they also allow laser manipulation of particles [86]. I will exploit these capabilities to observe at an atomistic scale, with both spatial and temporal resolution, the sudden onset of shear-induced melting. In most previous dusty plasma experiments, melting was studied under *steady-state* conditions (by changing plasma parameters [19, 20, 92], varying particle number [93], and laser manipulation [50, 82]). The *temporal development* of melting has received less study, and experiments that have been reported [22, 86] relied on mechanisms other than shear-induced melting.

Particles have an electrical charge  $Q$  and are electrically confined in a single horizontal layer where they self-organize with a structure analogous to a crystalline solid or a liquid [86]. Coulomb repulsion is shielded with a screening length  $\lambda_D$  [13]. Dusty plasmas are driven-dissipative systems [31, 86], with frictional drag on the rarefied gas at a damping rate  $\nu_f$  [14]. The collective oscillation of particles can be characterized by the nominal 2D dust plasma frequency  $\omega_{pd}$  [75].

For a dusty plasma suspension, shear must be applied differently than for

most substances (e.g., colloidal suspensions [46]) because the suspension does not contact a container. I apply shear internally within my sample, using laser radiation pressure [50, 91].

### 4.3 Experiment

Using the apparatus of [31], an Argon plasma was generated in the vacuum chamber at 15.5 mTorr, powered by 13.56 MHz radio-frequency voltages at 184 V peak to peak. The particles were polymer microspheres with a diameter  $8.1 \mu\text{m}$  and a gas damping rate  $\nu_f = 2.7 \text{ s}^{-1}$  [14].

The particles were suspended in a single layer. Before applying shear they self-organized in a triangular lattice with six-fold symmetry [86]. Particle motion was essentially 2D, with negligible out-of-plane displacements and no buckling of the particle layer. The suspension had a diameter  $\approx 52 \text{ mm}$  and contained  $> 11\,000$  particles. About 2800 particles were in the analyzed region,  $(24.7 \times 20.4) \text{ mm}^2$ . The particle spacing was characterized by a Wigner-Seitz radius [75]  $a = 0.25 \text{ mm}$ .

To apply shear stress with a sudden onset, I used laser radiation pressure, which applies forces internally within the sample [50]. The power of a pair of 532-nm laser beams was increased within 40 ms to a constant level. A different constant level was chosen for each of my four runs, varying from 0.57 to 1.90 W per beam, as measured inside the chamber. The beams pointed oppositely in the  $\pm x$  directions and struck the suspension at a  $6^\circ$  downward angle. Their width and separation were  $\Delta Y_l \approx 0.2 \text{ mm}$  and  $L = 4.7 \text{ mm}$ , respectively. To apply shear across the entire suspension width, the beams were rastered across the full suspension (at a frequency high enough, 200 Hz, to avoid exciting coherent waves at the rastering frequency [82]).

Using a top-view camera, I recorded videos for a duration of 14 s (including 5 s before applying shear). While applying shear, particles flowed out of the camera's

field of view (FOV); they circulated around the suspension's perimeter and then reentered the FOV [50]. Between runs I turned laser manipulation off for  $\approx 20$  min, so that the suspension had enough time to cool, solidify and anneal [86]. Then I calculated particle positions and velocities in each video frame [86].

Using the wave-spectra analysis method for particle random motion in an ordered lattice [27], I found these parameters for my dusty plasma:  $\omega_{pd} = 72.6 \text{ s}^{-1}$ ,  $Q/e = -(8700 \pm 900)$ ,  $\lambda_D = (0.33 \pm 0.07) \text{ mm}$ . The same method also yielded the transverse and longitudinal sound speeds,  $C_t = (4.0 \pm 0.4) \text{ mm/s}$  and  $C_l = (15.0 \pm 1.5) \text{ mm/s}$ , respectively. When coherent waves are observed experimentally, they can be identified as transverse or longitudinal waves by their speed and by the direction  $v_x$  or  $v_y$  of particle motion.

#### 4.4 Data analysis

The experiment was designed to have symmetry with an ignorable coordinate  $x$ . I average some quantities over  $x$ , as denoted by  $\langle \rangle_x$  (averaging with cloud-in-cell weighting with a bin width of the lattice constant,  $1.9 a$ ). The kinetic energy (KE) is averaged over both  $x$  and  $y$  for the full analyzed region, as denoted by  $\langle \rangle_{xy}$ . I calculate  $\text{KE} = \text{KE}_x + \text{KE}_y$ , where  $\text{KE}_x = m \langle v_x^2 \rangle_{xy} / 2$ , and similarly for  $\text{KE}_y$ . Although this definition includes the energy of directed flow as well as random motion, I will report the values in temperature units ( $K$ ), to allow comparison to other experiments.

#### 4.5 Results

Results in Fig. 4.1(a),(b) show the development of KE and the flow velocity after I suddenly applied shear stress. The KE increases dramatically, by about two orders of magnitude, Fig. 4.1(a). Melting occurs for laser powers above a threshold  $\approx 0.4 \text{ W}$ . The flow pattern, Fig. 4.1(b), broadens until reaching a steady state

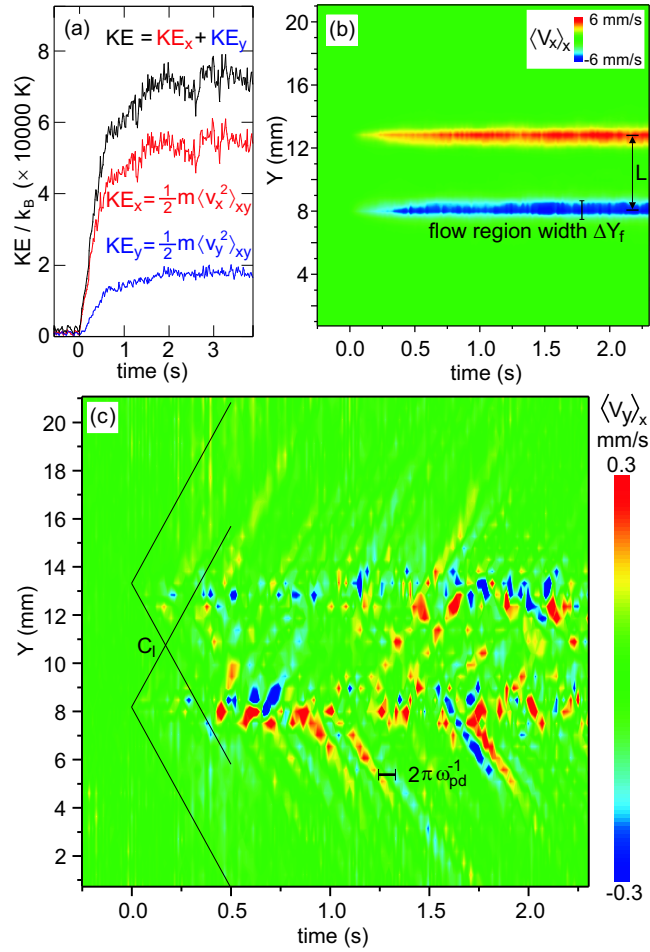


Figure 4.1: Temporal development of kinetic energy (KE), flow, and transverse velocity. (a) Time series of the average KE. Shear was applied suddenly by applying 0.95W of laser power starting at  $t = 0$ . The KE rose about two orders of magnitude until a steady state was reached at  $\approx 1$  s. (b) Spatiotemporal evolution of the flow velocity  $\langle v_x \rangle_x$ . Two counter-propagating flow regions broaden to a width  $\Delta Y_f$  (defined as FWHM of the velocity profile). Length scales, including the thickness  $\Delta Y_l$  and spacing  $L$  of the laser sheets, are ordered as  $\Delta Y_l \approx a < \Delta Y_f < L$ . (c) Coherent longitudinal waves, generated near the flow region and propagating outward. This is revealed by the repeated pattern of wavefronts in this plot of  $\langle v_y \rangle_x$ . For comparison, the longitudinal sound speed  $C_l$  is indicated by the straight lines. The observed wave period is  $\approx 4\pi\omega_{pd}^{-1}$ .

at  $\approx 1$  s, when the full width at half maximum (FWHM) of the velocity profile is  $\Delta Y_f = 1.2$  mm, which I will refer to as the flow regions. This width  $\Delta Y_f$

is determined by a combination of shear stress applied by the laser, gas friction, and shear viscosity of the suspension [50]. The KE is greater for velocities in the  $x$  direction than in the  $y$  direction because shear was applied in the  $x$  direction ( $\approx 53\%$  of  $\text{KE}_x$  is due to directed flow in the steady state). Scale lengths in the flow are ordered as  $\Delta Y_l \approx a < \Delta Y_f < L$ . The flow is laminar, with a Reynolds number  $\ll 10^2$  [50]. In the flow region, the kinetic temperature (estimated from  $v_y$ ) is high, with  $\Gamma \approx 20$ ; this is well beyond the predicted melting point  $\Gamma = 160$  [73].

To answer my first question, I observe coherent *longitudinal* waves propagating away from the flow region. This result might be surprising because the energy input was purely shear. These longitudinal waves are revealed in Fig. 4.1(c) by wavefronts with a slope corresponding to the longitudinal sound speed,  $C_l$ . The wavefronts emerge from the flow region, suggesting that the longitudinal waves were generated there. These wavefronts repeat, indicating the waves are coherent, not random.

The coherent longitudinal waves in Fig. 4.1(c) have a period  $\approx 4\pi\omega_{pd}^{-1}$ . This is almost the same as the period where the dispersion relations of longitudinal and transverse waves cross [94]. This observation suggests that the coherent longitudinal waves I observe could be explained by scattering from transverse waves.

Energy is carried into the surrounding lattice by these coherent longitudinal waves. I will consider the speed of these waves below, when explaining sudden shear-induced melting.

To answer my second question, I find that after sudden application of shear, melting occurs in two steps. Examining Fig. 4.2(a), I can see that defects initially proliferate at a higher rate, then soon after at a slower rate, with a distinctive transition between. I term these “melting stages” 1 and 2. Afterwards, at a long time, there is of course a steady state. I confirmed that the transition is ubiquitous: it occurs for all four laser powers I tested, and also in other suspensions with various

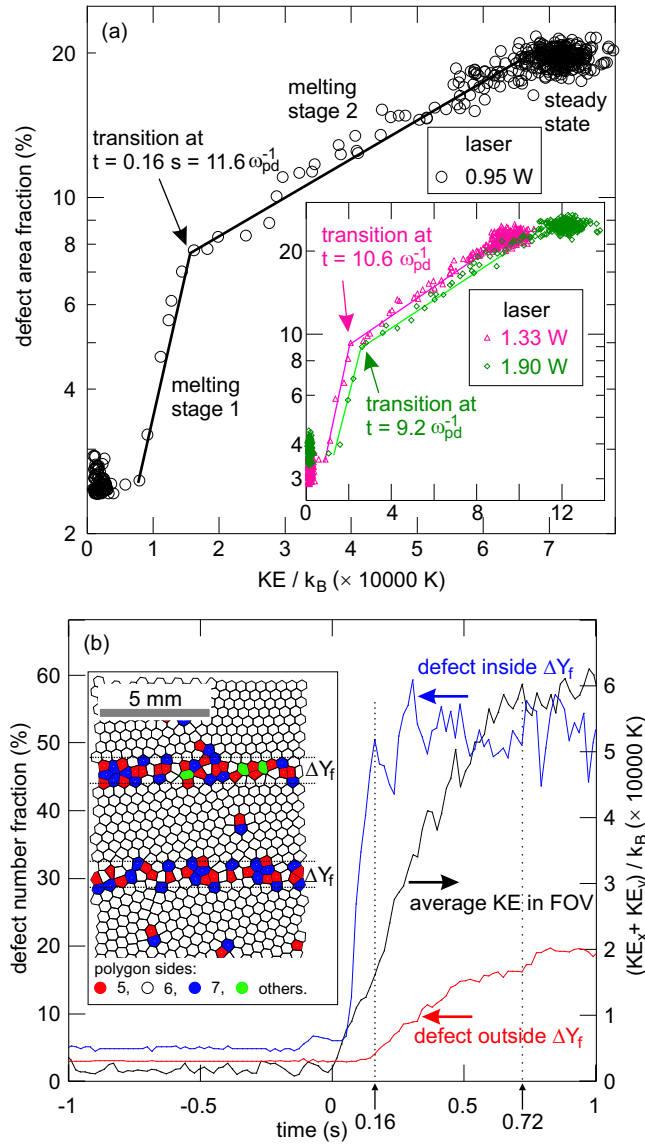


Figure 4.2: Two melting stages, due to the spatial development. (a) Phase diagram, showing the proliferation of defects as the KE increases, recorded at 0.018 s intervals, for three laser powers. A transition between two stages is revealed. The quantity plotted is the defect area fraction; this measure of structure is the area of a Voronoi diagram that is occupied by defects [86], divided by the total area. (b) Time series for KE and defects, counted separately inside and outside the flow regions of width  $\Delta Y_f$ . The timing indicates that defects proliferate outside only after they saturate inside the flow regions. (The inset shows about 1/4 of the Voronoi diagram, for the run at 0.95 W at  $t = 0.16 \text{ s}$ .)

values of the particle spacing.

My experiment provides both spatial and temporal resolution, which I can exploit to investigate the cause of the transition between the two melting stages. I am motivated by Fig. 4.1(b) to analyze time series separately in two spatial portions: inside and outside the flow regions. This yields the time series in Fig. 4.2(b), where the quantity plotted is the defect number fraction, calculated by dividing the number of defects by the number of particles.

Figure 4.2(b) reveals that defects proliferate in different places at different times. In melting stage 1, they proliferate mainly inside the flow regions until saturating at  $t = 0.16$  s. Importantly, this is the same time as the transition in Fig. 4.2(a). Only afterwards do defects spread widely outside the flow region, as seen in the bottom curve in Fig. 4.2(b). Thus, the transition in the phase diagram arises from the different timing of when defects appear in the two different regions: first inside the flow region until defects saturate there, and then outside.

I can quantify the physical time scales for the two melting stages. Candidate time scales include  $\omega_{pd}^{-1}$ , which characterizes mutual particle motion due to inter-particle electric fields, and  $\nu_f^{-1}$  due to gas friction. Initially, when velocities are low, I expect friction to be small, leading us to consider  $\omega_{pd}^{-1}$  as the time scale for melting stage 1. I find that melting stage 1 has a duration on the order of  $10 \omega_{pd}^{-1}$ , no matter how much shear is applied, as shown in Fig. 4.2(a). Later, as the KE increases, Fig. 4.2(b), dissipation by gas friction grows until it balances the energy input from the laser, yielding a steady state. The role of friction in limiting the spread of melting is suggested by noting that the duration of melting stage 2 is  $\approx 1.5 \nu_f^{-1}$ .

To answer the third question, I find that there is a distinctive melting front, and it propagates at about the transverse sound speed,  $C_t$ . This is seen in Fig. 4.3,

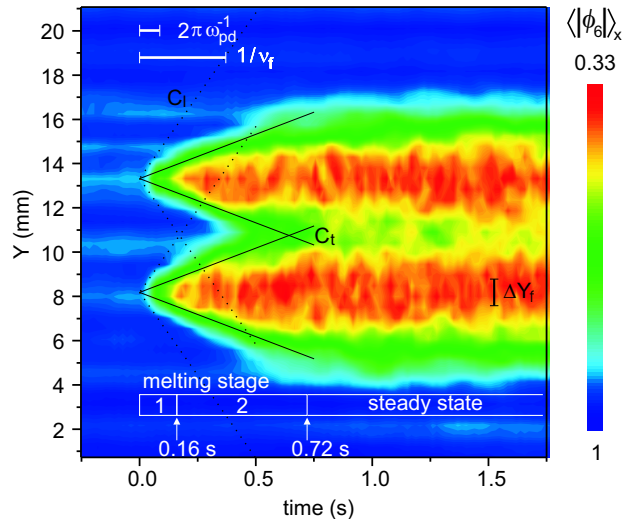


Figure 4.3: Spatiotemporal evolution of orientational order,  $|\phi_6|$ , which is defined to have a maximum of unity for a perfectly crystalline region [42, 44, 91]. Lines are drawn with the slopes  $C_t$  and  $C_l$ , starting at  $t = 0$ . The transverse sound speed,  $C_t$ , coincides with the melting front propagation. The resolution of my data along the  $Y$  axis is  $1.9 a$ .

where the colored contours show how disorder spreads with time. I also draw lines with a slope corresponding to  $C_t$ ; comparing these to the melting front, I see that they coincide. Thus, the melting front propagates at about  $C_t$ , not the much faster  $C_l$ . I verified this result using three different measures of structure. These include the local six-fold bond-orientational order  $|\phi_6|$  [42, 44, 91] (as shown in Fig. 4.3), defect number fraction, and height of the first peak of the local pair correlation function.

Before this experiment, it was not obvious whether the melting front should spread at a rate corresponding to  $C_t$ ,  $C_l$ , or thermal conduction. Thermal motion can be decomposed into incoherent waves that include both transverse and longitudinal modes. Coherent waves are also present, including the surprising longitudinal modes I found propagating away from the flow region. Thermal conduction due to temperature gradients [29, 30, 95] would also lead to a spreading of energy as time

passes.

To determine whether the flow of energy is in the form of waves or thermal conduction [29, 30, 95], I varied the laser power, which will vary the gradients. Linear waves propagate at the same speed, regardless of their amplitude; but energy spreads by thermal conduction more rapidly if the gradients are larger. I found that the melting front propagated at nearly  $C_t$  for all four laser powers I tested. Thus, I dismiss thermal conduction as the main mechanism for the propagation of energy that results in the melting front.

My result that the melting front propagates at about  $C_t$  suggests that the propagation of transverse waves is the mechanism for transferring the energy required for melting in my experiment. Transverse waves, which were excited when shear was first applied, propagate outward carrying energy that can create defects. As this wavefront travels, it loses energy by creating disorder and by gas friction. Eventually, after traveling about 3 mm, the outward traveling wave loses so much energy that it can no longer generate more defects, and the steady state is reached. It is possible that in other systems, with greater applied shear, the generated coherent longitudinal waves might be strong enough to melt a solid lattice, so that the melting front would propagate at  $C_l$ .

## 4.6 Conclusion

In summary, I found that coherent longitudinal waves are excited in this shear-induced melting system. Applying shear suddenly led to melting in two stages separated by a distinctive transition. After defects saturated within narrow flow regions, they spread wider with a melting front that propagates at about  $C_t$ .

## CHAPTER 5

### VISCOELASTICITY OF 2D LIQUIDS QUANTIFIED IN A DUSTY PLASMA EXPERIMENT

Strongly-coupled plasmas can exhibit solid-like or liquid-like behavior, which are often characterized by the properties of elasticity or viscosity, respectively. However, most liquids and soft materials actually exhibit both elasticity and viscosity at the same time, and this is called viscoelasticity. While viscoelasticity is well known for other materials, it has been little studied for strongly-coupled plasmas, perhaps because weakly-coupled plasmas cannot exhibit viscoelasticity. Previous work has been limited to a few quantitative theories for liquid-phase strongly-plasmas and a few dusty-plasma experiments that provided qualitative descriptions of collective particle motion ascribed to viscoelasticity. In the theory of liquids, it is common to quantify viscoelasticity using the frequency-dependent viscosity  $\eta(\omega)$  or, more recently, the wavenumber-dependent viscosity  $\eta(k)$ . However, for strongly-coupled plasmas there have been no previous experiments, and only one recent simulation [96], that make use of these measures of viscoelasticity. Here, I exploit the ability to track discrete particles in a dusty plasma experiment in order to compute the functions needed to calculate  $\eta(k)$ . To confirm my interpretation of the experiment, I also perform a Langevin simulation under conditions that mimics the experiment, and this provides the same kind of data for the discrete particles: time series for their positions and velocities. This experiment is the first laboratory quantification of viscoelasticity in a strongly-coupled plasma.

In order to calculate  $\eta(k)$  for a dusty plasma, I must account for the effect of gas friction acting on the particles. To do this, I generalize the expression for calculating  $\eta(k)$  from the transverse current autocorrelation function (TCAF), which is found by tracking random particle motion. I find that the TCAF exhibits an

oscillation that is a signature of elastic contributions to viscoelasticity. I also find that  $\eta(k)$  diminishes with increasing  $k$ , indicating that viscous behavior is gradually replaced by elastic behavior as the scale length is reduced. This diminishment can be modeled as  $\propto (1 + \alpha k^2)^{-1}$ . To validate my method of analyzing the experimental results, I also perform a simulation of a 2D Yukawa liquid.

The results in this chapter correspond to Y. Feng, J. Goree, and B. Liu, “*Viscoelasticity of 2D liquids quantified in a dusty plasma experiment*,” *Physical Review Letters*, Vol. 105, article number 025002 (2010).

## 5.1 Introduction to viscoelasticity

Two-dimensional (2D) physical systems include electrons on a liquid helium surface [15], colloids [89], granular fluids [18], and dusty plasmas [11]. In experiments and simulations, elastic properties, such as transverse waves [26, 97], and transport properties, such as viscosity  $\eta$  [50, 98, 99], have been studied.

Viscoelasticity is a property of materials that exhibit both viscous and elastic characteristics [51]. One usually thinks of viscous properties for liquids and elastic properties for solids, but most materials are viscoelastic and exhibit both. These include, for example polymers, human tissue, and hot metal [51]. In general, liquids exhibit elastic effects especially at short length or time scales [52], but viscous effects at long length or time scales.

To quantify viscoelasticity, one often uses the frequency-dependent viscosity  $\eta(\omega)$  [57, 100], which tends toward the static viscosity,  $\eta$ , as  $\omega \rightarrow 0$ . The  $\eta(\omega)$  is easily measured in three-dimensional (3D) liquids using rheometers and viscometers [57, 100], but not in most 2D liquids.

## 5.2 Wavenumber-dependent viscosity

Besides  $\eta(\omega)$ , the wavenumber-dependent viscosity,  $\eta(k)$ , has been used by theorists to quantify the viscoelastic character [58, 59, 60, 61, 62]. They have recently developed ways of computing  $\eta(k)$  from the trajectories of random motion of molecules [61, 62]. However, until now, there have been no experimental measurements in any physical systems known to us of  $\eta(k)$  that exploit this new analysis method. One difficulty in using this method in an experiment is that it requires, as its inputs, the positions  $x_i$  and velocities  $v_i$  of  $N$  individual molecules or particles as they move about randomly. In this chapter, I will use an experimental system, dusty plasma, that allows observing these inputs directly.

Here I further develop a method for computing  $\eta(k)$ , generalizing it for multiphase systems like dusty plasma. As was originally developed for 3D molecular dynamics (MD) simulations, the method begins with computing the normalized transverse current autocorrelation function [61, 62] (TCAF), which is defined as

$$C_T(k, t) = \langle j_y^*(k, 0) j_y(k, t) \rangle / \langle j_y^*(k, 0) j_y(k, 0) \rangle, \quad (5.1)$$

where  $j_y(k, t) = \sum_{i=1}^N v_i^y(t) \exp[ikx_i(t)]$  is the transverse current, with the vector  $k$  parallel to the  $x$  axis. Then,  $\eta(k)$  can be calculated [61, 62] through  $\eta(k)/\rho = 1/(k^2 \Phi)$ , where  $\Phi$  is the area under the normalized TCAF. This equation can be derived, assuming that the viscosity is a valid transport coefficient, either from the hydrodynamic Navier-Stokes equation or from linear response theory [62]. Here, I generalize this equation using  $\partial \mathbf{j}(\mathbf{r}, t) / \partial t - (\eta/\rho) \nabla^2 \mathbf{j}(\mathbf{r}, t) + \nu_f \mathbf{j}(\mathbf{r}, t) = 0$ , a Navier-Stokes equation that includes an additional frictional drag force  $\nu_f \mathbf{j}(\mathbf{r}, t)$  due to a second phase [50]. This equation is valid in both 2D and 3D systems. Following the method of [62], I find

$$\eta(k)/\rho = ((1/\Phi) - \nu_f)/k^2. \quad (5.2)$$

The detailed derivation is in the Appendix A.

Here I will characterize viscoelasticity in an experiment two ways. First, as a signature of elastic effects, I will detect oscillations in the TCAF [59, 61] for large  $k$ , which is different from the monotonic decay of the TCAF [59] at small  $k$  due to viscous behavior. Second, I will measure the diminishment of  $\eta(k)$  as  $k$  increases. This diminishment occurs along with a relative increase of elastic contributions to viscoelasticity, for large  $k$ .

### 5.3 Dusty plasma

Dusty (complex) plasma, is partially ionized gas containing micron-size particles of solid matter [11, 20, 86]. Particles have a charge  $Q$  and can be electrically confined in a single horizontal layer where they self-organize with a structure like a crystalline solid [86]. Coulomb repulsion is shielded with a screening length  $\lambda_D$  [13, 101]. The elastic properties of the crystalline solid arise from interparticle repulsion and can be characterized by the phonon spectrum for longitudinal and transverse waves [94], which have a frequency close to the nominal 2D dust plasma frequency  $\omega_{pd}$  [75]. The solid can be melted, to form a liquid, by applying laser manipulation [82, 102].

Dusty plasmas are attractive for experimental quantification of viscoelastic effects at a microscopic scale. As in colloids [89] and granular fluids [18], they allow video microscopy to track the  $x_i$  and  $v_i$  of individual particles. They also provide both elastic and viscous effects. The particles are immersed in a medium that is a rarefied gas that does not overdamp particle motion, unlike colloids [89] with their solvents.

In the literature of strongly-coupled plasmas, viscoelasticity has been studied both theoretically [53, 54] and experimentally [55, 56]. Kaw and Sen introduced viscoelastic coefficients in a generalized hydrodynamics model to describe the dynamics of strongly-coupled plasmas [53]. In a similar theoretical approach, Murillo

generalized the viscosity coefficient by adding a viscoelastic relaxation time in a hydrodynamic model of strongly-coupled plasmas [54]. This approach yielded a viscoelastic Navier-Stokes equation [54]. A recent simulation [96] yielded results for  $\eta(\omega)$  or  $\eta(k)$ , as measures of viscoelasticity, for 3D strongly-coupled plasmas.

Dusty plasma experiments, until now, have yielded descriptive presentations of viscoelasticity [55] and demonstrations of the microscopic motion of particles associated with viscoelastic response [56]. In experiments, the static viscosity has been measured [50] and estimated from diffusion observations [21]. However, quantitative characterization of viscoelasticity, using  $\eta(\omega)$  or  $\eta(k)$ , is lacking from the literature.

A challenge in dusty plasma experiments is that they do not allow direct contact of the suspension with a container. Thus, the viscoelastic response cannot be measured with a rheometer. I overcome this challenge by observing the random particle motion and using Eq. (5.2) to compute  $\eta(k)$ . I will do this with experimental data, and confirm my interpretation using a simulation.

#### 5.4 Experiment

Using the apparatus of [31], a plasma was powered by 13.56 MHz, 170 V peak to peak voltages. After the 8.1  $\mu\text{m}$  diameter microspheres were introduced into the plasma (which had an Argon pressure of 14 mTorr), they experienced a damping rate of  $\nu_f = 2.4 \text{ s}^{-1}$  [14].

The particles were suspended in a single layer. They self-organized in a triangular lattice [86]. Particle motion was essentially 2D, with negligible out-of-plane displacements. The suspension had a diameter  $\approx 52 \text{ mm}$  and contained  $> 5400$  particles. The lattice constant  $b = 0.67 \text{ mm}$  corresponds to a Wigner-Seitz radius [75]  $a = 0.35 \text{ mm}$ .

Particle tracking was done by imaging from the top. For each of four runs,

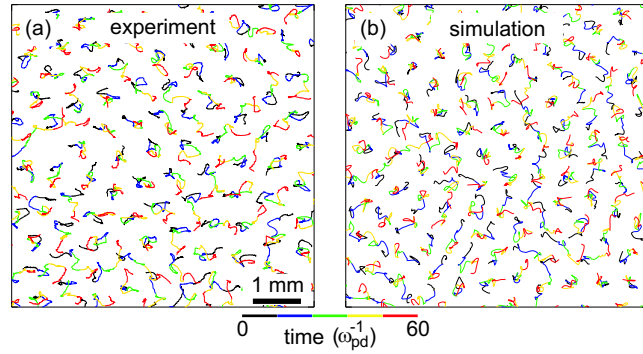


Figure 5.1: Particle trajectories in a 2D liquid, with color representing time. To illustrate the random particle motion, (a) shows  $\approx 10\%$  of the spatial region I analyzed, for a duration  $60 \omega_{pd}^{-1}$  which is about  $\approx 10\%$  of one movie, i.e., one run in the experiment, while (b) is a part of a Langevin MD simulation, shown over the same time interval.

20 s videos were recorded at 250 frames/s, providing adequate time resolution for the TCAF. The  $(36.2 \times 22.6)$  mm<sup>2</sup> field of view (FOV) included  $\approx 2100$  particles. I recorded the maximum 5061 frames per run allowed by the 12-bit Phantom v5.2 camera, with a lens that provided a resolution of 0.03 mm/pixel. For each video frame  $j$ , I computed [103] the position of the  $i$ th particle,  $\tilde{x}_{i,j}$ . To compute  $j_y(k, t)$ , I used  $x_{i,j} = (\tilde{x}_{i,j-1} + \tilde{x}_{i,j} + \tilde{x}_{i,j+1})/3$  and  $v_{i,j}^y = (\tilde{y}_{i,j+1} - \tilde{y}_{i,j-1})/2\delta t$ . This finite-difference method reduced errors arising from the high frame rate. Examples of particle trajectories from the experiment are shown in Fig. 5.1(a). Next, I computed  $j_y(k, t)$  and smoothed its time series over five frames before calculating the TCAF, Eq. (5.1), and finally  $\eta(k)$ , Eq. (5.2).

Before melting the suspension, I used the phonon-spectrum method for a lattice [94] to measure  $Q/e = -6000$ ,  $\kappa_0 = a/\lambda_D = 0.5$ , and  $\omega_{pd} = 30 \text{ s}^{-1}$ . After melting, I determined  $T$  from the mean-square velocity fluctuation [86] yielding  $\Gamma = (Q^2/4\pi\epsilon_0 a)/(k_B T) = 68$ .

I melted the lattice and maintained a steady kinetic temperature  $T$  using laser manipulation [31, 82]. Random kicks were applied by radiation pressure from a

pair of 532-nm laser beams that were rastered across the suspension in a Lissajous pattern with frequencies  $f_x = 48.541$  Hz and  $f_y = 30$  Hz. This pattern filled a rectangle larger than the camera's FOV. Along with the desired random motion, the Lissajous heating method also produces coherent modes [82], which had about 8% of the total kinetic energy for motion in the  $y$  direction, similar to [31]. I analyzed half of the FOV, where the temperature was uniform within extremes of  $\pm 20\%$ .

## 5.5 Simulation

Since this is apparently the first experiment to make use of the TCAF to measure  $\eta(k)$ , I performed a Langevin MD simulation [87, 104, 105, 106] of a 2D Yukawa liquid to mimic my experiment. Using periodic boundary conditions and 4096 particles, the equation of motion Eq. (3) of [87] was integrated, yielding particle trajectories, Fig. 5.1(b). The simulation parameters  $\Gamma = 68$ ,  $\kappa_0 = 0.5$ , and  $\nu_f/\omega_{pd} = 0.08$  match the experimental values. To improve statistics, the simulation was run much longer,  $\omega_{pd}t = 22\,300$ , than the experiment  $\omega_{pd}t = 607$ . To validate my Langevin MD simulation, I also performed a frictionless MD simulation [98] and calculated  $\eta(k)$  as in Eq. 5.2 but with  $\nu_f = 0$ ; I found that the results for  $\eta(k)$  for the two types of simulations agree. In addition to computing  $\eta(k)$ , I also computed the static viscosity  $\eta$  using the Green-Kubo relation, Eq. (3) of [98]. The latter assumes that the shear-stress autocorrelation function decays significantly faster than  $1/t$ , which I verified.

## 5.6 Results

Experimental results for the TCAF, Fig. 5.2(a), reveal elastic properties in the viscoelastic regime for this liquid. The TCAF computed from Eq. (5.1) exhibits an initial decay followed by oscillations around zero [59, 61], for  $kb = 3.26$

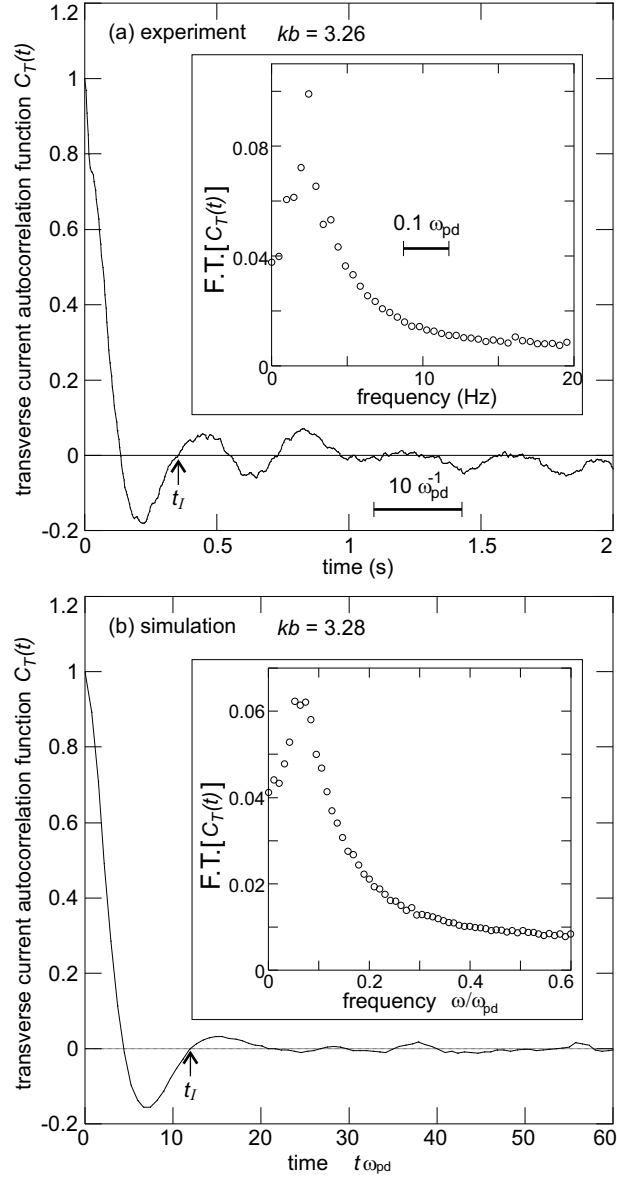


Figure 5.2: Transverse current autocorrelation function (TCAF) in the 2D liquid computed using Eq. (5.1) for (a) the experiment at  $kb = 3.26$ , and (b) the Langevin MD simulation at  $kb = 3.28$ . At short times, the TCAF decays due to viscous effects, while at longer times (after its first positive zero crossing,  $t_I$ ) it oscillates due to elastic effects. The frequency spectrum for each TCAF, shown in the insets, reveals a peak that is a signature of the elastic contribution to viscoelasticity. These results are different from the pure monotonic decay of TCAF and its spectrum that would be observed in a purely viscous regime. (Here,  $b$  is the lattice constant measured before melting.)

in Fig. 5.2(a). Such oscillations typically indicate that the selected wavenumber corresponds to the viscoelastic regime. The TCAF is a time series; I also calculate its frequency spectrum, shown in the inset of Fig. 5.2(a). (This frequency spectrum can also be used in generating a phonon spectrum [52]). The spectrum features a prominent peak at non-zero frequency. This peak is a signature of shear elasticity; it would be absent in a viscous regime. To my knowledge, the TCAF time series has not previously been reported for dusty plasma experiments as an indicator of viscoelasticity.

Simulation results, Fig. 5.2(b), exhibit features in the TCAF and its spectrum [59] similar to those in the experiment. This agreement between experiment and simulation lends confidence to my use of the TCAF as a quantitative indicator of viscoelasticity in an experimental system.

For wavenumbers much smaller than those shown in Fig. 5.2, i.e., for very long wavelengths, I would expect viscous behavior characterized by a simple decay of the TCAF with no oscillations. This hydrodynamic regime has been well studied in simulations and theory [77]. Observing it requires a sufficiently large system. One of the attractions of my physical system is that it allows direct observation of motion at an atomistic scale. Thus, I use it here to observe the viscoelastic regime (at small wavelengths), not the purely viscous hydrodynamic regime.

As my chief result, my experimentally measured wavenumber-dependent viscosity,  $\eta(k)$ , is presented quantitatively in Fig. 5.3(a). I observe that  $\eta(k)$  diminishes as  $k$  increases. Physically, this trend indicates that dissipative or viscous effects diminish at shorter length scales. At these shorter length scales, elasticity has a greater effect.

Since previous experiments are not available for quantitative comparison, I compare my experimental results to the Langevin simulation, Fig. 5.3(b). I note

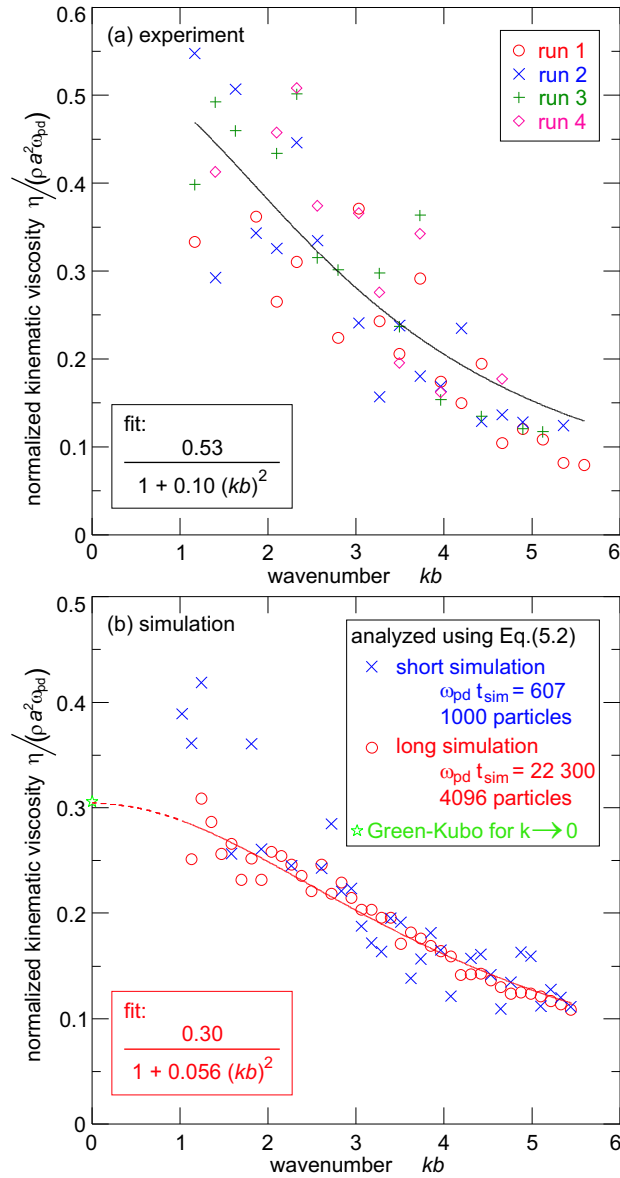


Figure 5.3: The wavenumber-dependent viscosity  $\eta(k)$  of the 2D liquid, computed using Eq. (5.2) for (a) the experiment and (b) simulations of two sizes. I find that  $\eta(k)$  diminishes with  $k$ , which is a signature of viscoelastic effects. The size of the smaller simulation mimics the size of the experiment; comparing them reveals that the scatter of the experimental data (a) arises from the data size. In (b), the Green-Kubo (static) viscosity  $\eta$  is indicated by a star symbol. Here, the kinematic viscosity  $\eta(k)/\rho$  and wavenumber  $k$  are normalized to be dimensionless.

that  $\eta(k)$  exhibits the same downward trend and similar quantitative values in the experiment and the simulations. For both the experiment and simulation, I present results for  $\eta(k)$ , computed using Eq. (5.2), for the viscoelastic regime, i.e.,  $k > 1/b$ . For each  $k$ , the infinite time limit for the integration of  $\Phi$  was replaced with  $t_I$ , the time of the first upward zero-crossing of TCAF time series (Fig. 5.2). This integration limit retains both the viscous effects at short time and the elastic effects within the first negative peak.

Noise in the experimental results arose from the finite amount of current data used to compute the TCAF. To verify that this accounts for the scatter in the experimental  $\eta(k)$  in Fig. 5.3(a), I repeated the simulation with a shorter time, matching the experiment not only in duration but also in particle number. This test shows, in Fig. 5.3(b), that scatter arises from the finiteness of the  $j_y(k, t)$  data to the same extent as in the experiment. In both the experiment and in the shorter simulation, a few TCAF curves were too noisy to analyze, with a lack of a well-defined upward zero-crossing; the corresponding few data points are omitted from Fig. 5.3.

I fit  $\eta(k)$  in Fig. 5.3 to the same empirical Padé approximant used originally for MD simulations of 3D liquids of hard spheres [58] and water [61]. This approximant,  $\eta(k) \propto (1 + \alpha k^2)^{-1}$ , apparently has never been applied for 2D liquids. I found that this form fits both my experimental and simulation data in Fig. 5.3 as well as the scatter allows. However, a simple power law does not fit the  $\eta(k)$  data as well.

In addition to finding that my  $\eta(k)$  fits the Padé approximant, I also find in Fig. 5.3(b), that it extrapolates as  $k \rightarrow 0$  to the static viscosity  $\eta$  [61]. In this test, I found  $\eta$  using the Green-Kubo relation [98] with my Langevin simulation; and this result, shown as a star in Fig. 5.3(b), agrees with previous simulations that used different methods [98, 99].

## 5.7 Conclusion

In conclusion, I performed an experiment to quantify viscoelasticity of 2D liquids using the TCAF and  $\eta(k)$ . I did this using measurements of random particle motion in a dusty plasma, which is a frictional system. I generalized a method of calculating  $\eta(k)$  by including the friction in the Navier-Stokes equation; and I presented an experimental demonstration of this method. My experimental results for  $\eta(k)$  show that it diminishes with increasing  $k$  that can be modeled as  $\propto (1 + \alpha k^2)^{-1}$ , which compares well with simulation results.

## CHAPTER 6

### DUSTY PLASMA RELAXATION AND MELTING STUDIED USING THE INTERMEDIATE SCATTERING FUNCTION

In this chapter, I report numerical simulations of random particle motion in strongly-coupled plasmas. Because of the importance of discrete particle effects, including motions with respect to nearby particles, strongly-coupled plasmas are best modeled using particle simulations. Unlike weakly-coupled plasmas, however, which can be modeled by particle simulations such as PIC (particle-in-cell) codes, strongly coupled plasmas have a much smaller number of particles in a Debye sphere and are dominated by Coulomb collisions. Therefore, instead of using a PIC simulation, I use a simulation that does not aggregate physical particles into synthetic super-particles, or employ grid-like smoothing techniques to eliminate the electric fields associated with Coulomb collisions. I use the molecular-dynamics (MD) method, which is simply an integration of the equation of motion for each discrete particle along with a precise calculation of the interparticle electric forces. My MD simulations are performed two ways: without external friction, and with friction to mimic gas drag in a dusty plasma.

At the microscopic scale of discrete particles, a weakly-coupled plasma is almost random like an ideal gas, and it can relax almost immediately from its previous state. However, a strongly-coupled plasma has a memory of the previous positions of individual particles with respect to their neighbors, due to the dominant role of Coulomb interparticle interactions. Here, I use a quantitative measure of the relaxation that is common in other fields such as condensed matter physics. This measure is the self-intermediate scattering function (self-ISF), which is a dynamical measure of random motion that requires for its calculation a time series of particle positions that is provided by the MD particle simulation.

Two problems are studied: relaxation in liquids and the solid-liquid phase transition. Relaxation is characterized by the temporal decay of the self-ISF, which I find can be fitted to a stretched exponential. A scaling of the relaxation time with wavenumber is found, and this scaling is shown to be useful for distinguishing normal and anomalous diffusion. (This kind of anomalous diffusion is different from the anomalous transport mechanisms that often take place in magnetized weakly-coupled plasmas, due to turbulence for example.) Friction has little effect on relaxation except for high levels of frictional dissipation, where the effect is a retardation of relaxation. The solid-liquid phase transition is usually identified by measures of structure, but here the self-ISF, which is a dynamical measure, is demonstrated to be a sensitive indicator of the phase transition.

The results in this chapter correspond to Y. Feng, J. Goree, and B. Liu, “*Dusty plasma relaxation and melting studied using the intermediate scattering function,*” Physical Review E (submitted, 2010).

## 6.1 Introduction

Dusty plasma is partially ionized gas containing micro-sized particles of solid matter [86]. In a plasma [86], the sheath above a lower electrode has electric fields that can levitate and confine highly charged particles, so that they are suspended. When only a single layer is suspended, the interaction between dust particles is a repulsive Yukawa potential [13]. Video microscopy allows imaging this two-dimensional (2D) suspension at an atomistic scale, so that I can track particles and measure their individual positions and velocities in each video frame, yielding the same kind of data as the molecular dynamics (MD) simulations, reported here.

Particles self-organize in a crystal-like triangular lattice with hexagonal symmetry due to strong interparticle interaction. In this strongly-coupled plasma, the Coulomb interaction with nearest neighbors is so strong that particles do not easily

move past one another [7]. In many experiments, the particles occupy only a single horizontal layer, and are described as 2D experiments [55, 82, 86, 93, 94, 107]. Dusty plasma is a driven-dissipative system [86], and its kinetic energy is determined by the balance of the energy input and dissipation. As the driven energy input increases, the lattice becomes disordered in a solid-liquid phase transition [19, 20, 23, 32, 82, 86, 92].

Random particle motion in dusty plasmas can be divided into several stages. Ballistic motion [31] occurs on a short time scale  $< \omega_{pd}^{-1}$ , while caging oscillations [108] happen on a typical time scale of  $10 \omega_{pd}^{-1}$ . Here  $\omega_{pd}$  is the nominal plasma frequency [75]. At later times, particles can escape their cages and diffuse. A current research topic that has not been resolved is whether this long-time random motion is normal diffusion or anomalous diffusion. Experiments [31, 109] and simulations [104, 110, 111] with these 2D systems have indicated superdiffusion, where the mean-square-displacement (MSD) increases with the time more rapidly than linear scaling, but other simulations suggest that motion may be normal diffusion at sufficiently long times [106].

Data analysis methods used to study phase transitions and random motion are generally grouped in two categories: static and dynamic. In dusty plasma experiments and Yukawa MD simulations, attempts to identify phase transitions have mostly employed only structural measures, such as Voronoi diagrams and correlation functions for particle distance and angular orientation [19, 20, 23, 32, 73, 82, 86, 92]. Identifications of normal diffusion and superdiffusion have typically made use of dynamical measures: MSD time series, the PDF (probability distribution function) for particle displacements, and the velocity autocorrelation function [104, 106, 110, 111]. Here I will use a different dynamical analysis tool: the intermediate scattering function. I will use it to study both phase transitions and random motion.

The intermediate scattering function (ISF) [63], which has been used widely in other fields, is defined in terms of the particle trajectories:

$$F(\mathbf{k}, t) = \frac{1}{N} \sum_i \sum_j \langle \exp(-i\mathbf{k} \cdot [\mathbf{r}_i(t) - \mathbf{r}_j(0)]) \rangle. \quad (6.1)$$

Here,  $\mathbf{r}_i(t)$  is the trajectory of the  $i$ th particle in the system consisting of  $N$  particles. The Fourier transform variable  $\mathbf{k}$  is usually called a wavenumber, although no waves are studied using this method. Equation (6.1) makes use of an ensemble average  $\langle \cdot \cdot \cdot \rangle$ , which in practice is done by averaging for various initial starting times in place of  $t = 0$ . If the particle trajectories are known, then the ISF can be calculated directly using Eq. (6.1). This is the method I will use, as has been done previously in some experiments [64, 65] and MD simulations [66, 67, 68] for systems other than dusty plasmas. Besides starting from measurements of particle trajectories, other experimental methods of finding the ISF have been devised for colloids [112], supercooled liquids [113], and polymer nanocomposites [114]. In these experiments, the ISF was determined from data produced by dynamic light scattering [112], x-ray photon correlation spectroscopy [114, 115], or neutron spin echo spectroscopy [113, 77].

In Sec. 6.2, I will review the ISF method briefly. In Sec. 6.3, I will introduce my two MD Yukawa simulation methods: Langevin and frictionless. They will model a 2D dusty plasma. In Sec. 6.4, I will present results for the two physical processes studied here: relaxation in liquids and the melting phase transition.

## 6.2 Self-intermediate scattering function

Here I review the ISF, defined in Eq. (6.1), which is also called the density-density correlation function [116]. As mentioned in Sec. 6.1, the particle trajectories are the only required input data for calculating the ISF.

The ISF is composed of two parts [77, 117],  $F(\mathbf{k}, t) = F_s(\mathbf{k}, t) + F_c(\mathbf{k}, t)$ . The

most commonly used part is  $F_s(\mathbf{k}, t)$ , which is often called the *incoherent* part, or the *self-ISF*:

$$F_s(\mathbf{k}, t) = \frac{1}{N} \sum_i \langle \exp(-i\mathbf{k} \cdot [\mathbf{r}_i(t) - \mathbf{r}_i(0)]) \rangle. \quad (6.2)$$

The less commonly used part is  $F_c(\mathbf{k}, t)$ , which is called the *coherent* part:

$$F_c(\mathbf{k}, t) = \frac{1}{N} \sum_{i \neq j} \sum_j \langle \exp(-i\mathbf{k} \cdot [\mathbf{r}_i(t) - \mathbf{r}_j(0)]) \rangle. \quad (6.3)$$

The self-ISF,  $F_s(\mathbf{k}, t)$ , is a measure of single-particle dynamics as a function of time. This makes it comparable to the MSD and PDF, which are also computed from the trajectories of individual particles. Thus, the self-ISF can be used to study some of the same physical phenomena as MSD and PDF, such as random motion and the related idea of relaxation [65]. If random motion consists of normal diffusion, as for example with Brownian motion with a diffusion coefficient  $D$ , then [64, 65, 117]

$$F_s(\mathbf{k}, t) \simeq \exp(-Dk^2t). \quad (6.4)$$

In Sec. 6.4.1.2, I will generalize Eq. (6.4) for the case of anomalous diffusion, such as superdiffusion.

The self-ISF, Eq. (6.2), is often used by itself, without reporting the coherent part, Eq. (6.3). This is a common practice with particle trajectory data from experiments [64, 65] and MD simulations [66, 67, 68] for various physical systems. Here, I will also use only the self-ISF for my Yukawa simulations of dusty plasmas.

A graph of the self-ISF typically reveals two stages of random motion. I illustrate this in Fig. 6.1 with a sketch of  $F_s(\mathbf{k}, t)$  for a liquid that is not supercooled. Caging motion is indicated at short times. This early part of the curve is sometimes termed the fast  $\beta$  relaxation. Diffusive motion is indicated at long times, as particles gradually escape their cages [65]. In this later part of the curve, sometimes termed  $\alpha$  relaxation,  $F_s(\mathbf{k}, t)$  gradually decays toward zero. This decay is sometimes fitted

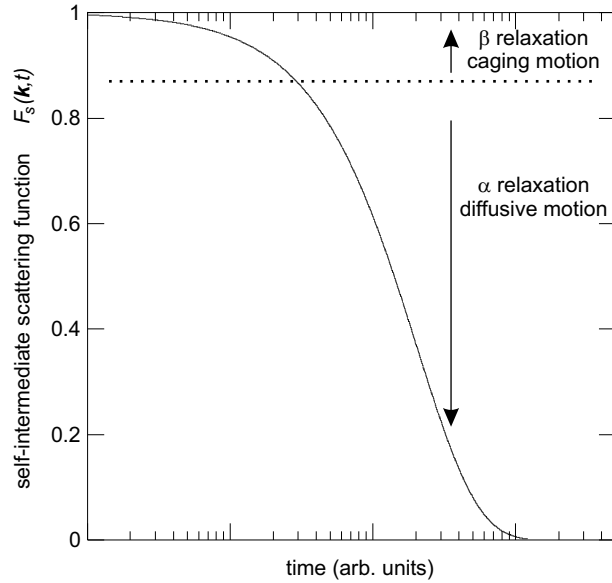


Figure 6.1: A typical example of the self-intermediate scattering function (self-ISF) for a normal liquid. Relaxation happens in two steps: early-time caging motion, and long-time diffusive motion. The self-ISF curve is often modeled by Eq. (6.5).

to a stretched exponential [79]:

$$F_s(\mathbf{k}, t) = \exp[-(t/\tau(k))^{\beta(k)}], \quad (6.5)$$

where  $\tau(k)$  is a relaxation time. (Note that this use of the symbol  $\beta$  has no relation to the  $\beta$  relaxation.)

In this chapter I will calculate the self-ISF from trajectory data for random motion in 2D Yukawa simulations. To characterize random motion, I will fit the self-ISF to Eq. (6.5), yielding  $\tau$  and  $\beta$ . Both of these fitting parameters are generally functions of  $k$ . I will then search for a scaling law for  $\tau(k)$ . Additionally, I will discuss the physical processes indicated when  $\beta$  differs from unity.

## 6.3 Simulation

### 6.3.1 Parameters

Equilibrium Yukawa systems can be classified by the values of the coupling parameter  $\Gamma$  and the screening parameter  $\kappa$  [118, 119]. Here,  $\Gamma = Q^2/(4\pi\epsilon_0 a k_B T)$  and  $\kappa \equiv a/\lambda_D$ , where  $Q$  is the particle charge,  $T$  is the particle kinetic temperature,  $\lambda_D$  is the screening length,  $a \equiv (n\pi)^{-1}$  is the Wigner-Seitz radius [75], and  $n$  is the areal number density. Another length scale is the lattice constant  $b$  for a defect-free crystal, which is  $b = 1.9046 a$  for a 2D triangular lattice.

My two simulation methods are the same in many aspects. Both simulation methods use a binary interparticle interaction with a Yukawa pair potential,

$$\phi_{i,j} = Q^2(4\pi\epsilon_0 r_{i,j})^{-1} \exp(-r_{i,j}/\lambda_D), \quad (6.6)$$

where  $r_{i,j}$  is the distance between the  $i$ th and  $j$ th particles. In both simulations, particles are only allowed to move in a single 2D plane. Conditions remained steady during each simulation run. For both simulations, the parameters I used were  $N = 16\,384$  particles in a rectangular box with periodic boundary conditions. The box had sides  $137.5 b \times 119.1 b$ . I truncated the Yukawa potential at radii beyond  $12 b$  [87]. The integration time step was  $0.037 \omega_{pd}^{-1}$ , and simulation data were recorded for a time duration of  $1777 \omega_{pd}^{-1}$  in after the system reached its steady state. Other simulation details are presented in [87, 110]. I report results with distances normalized by  $b$ , while time (and frictional damping rate  $\nu$ ) are normalized using the nominal plasma frequency  $\omega_{pd} = (Q^2/2\pi\epsilon_0 m a^3)^{1/2}$  [75], where  $m$  is the particle mass.

I will next review the two simulation methods. They differ mainly in the equations of motion that are solved.

### 6.3.2 Langevin MD simulations

My Langevin MD simulations take into account the dissipation due to frictional gas damping. The Langevin equation [87, 104, 105, 106, 110, 111] of motion for each particle is

$$m\ddot{\mathbf{r}}_i = -\nabla \sum \phi_{ij} - \nu m\dot{\mathbf{r}}_i + \zeta_i(t). \quad (6.7)$$

Trajectories  $\mathbf{r}_i(t)$  are found by integrating Eq. (6.7) for all particles. Terms on the right-hand side include a frictional drag  $\nu m\dot{\mathbf{r}}_i$  and a random force  $\zeta_i(t)$ . Note that I retain the inertial term on the left-hand-side in Eq. (6.7), unlike some Brownian-dynamics simulations of overdamped colloidal suspensions [120], where it is set to zero.

My Langevin simulations mimic 2D dusty plasma experiments [86], but the driven-dissipation mechanism is only an approximation of the processes in experiments [87]. In my Langevin simulation, the heating and friction are explicitly coupled by the fluctuation-dissipation theorem [121, 122]; this models collisions with gas atoms that provide both frictional drag and random kicks. However, besides random kicks from gas atoms, in dusty plasma there are some additional heating mechanisms arising from ion flow and sometimes external laser manipulation [86, 87] that are not explicitly modeled in my Langevin simulations.

### 6.3.3 Frictionless equilibrium MD simulations

In addition to my Langevin MD simulations which include friction, to obtain results in the frictionless limit, I also performed frictionless equilibrium MD simulations [110]. The equation of motion is

$$m\ddot{\mathbf{r}}_i = -\nabla \sum \phi_{ij}, \quad (6.8)$$

which I integrate for all particles. A Nosé-Hoover thermostat is applied to maintain a desired temperature [110].

This MD simulation method describes a frictionless atomic system. The particles collide among themselves, without any interaction with gas or other external influences. It mimics thermal equilibrium conditions.

There are two parameters I can change in the frictionless MD simulations:  $\Gamma$  and  $\kappa$ . In the Langevin simulations, I can also vary  $\nu$ . Varying  $\Gamma$  and  $\kappa$  is equivalent to varying temperature and density, and I will vary them over a range that allows us to simulate liquids or solids.

My method is to generate trajectories  $\mathbf{r}_i(t)$  for all particles by integrating Eq. (6.7) or (6.8), and then to compute the self-ISF using Eq. (6.2). The self-ISF is a time series. I repeat its calculation for various wavenumbers,  $k$ .

## 6.4 Results and discussions

I present results for two physical processes. First, I report the relaxation of the self-ISF for random motion in a liquid. I repeat this for different length scales by varying the wavenumber  $k$ . Second, I test whether the self-ISF can serve as a sensitive indicator of the phase transition between solid and liquid. All of these results are for steady conditions.

### 6.4.1 Relaxation and scaling

For random motion, the term “relaxation” refers to a gradual movement of particles from their previous positions, e.g., diffusion. This is indicated by the self-ISF,  $F_s(\mathbf{k}, t)$ , which begins at unity at  $t = 0$ , and then relaxes gradually to zero as  $t \rightarrow \infty$ . The relaxation rate in general depends on the scale length, which is parameterized here by  $k$ . Using the terminology of other users of the self-ISF [65, 123], the early stage of decay is termed  $\beta$  relaxation; during this early time particles are mainly trapped within their cages formed by nearest neighbors. The later stage is termed  $\alpha$  relaxation, and this corresponds to diffusive motion as particles deca-

The term “decaging” refers to a particle’s movement so that it is no longer trapped by the previous nearest neighbors. In a liquid, particles decay much more rapidly than in a solid, so that this  $\beta$  relaxation is much faster in liquids than solids.

#### 6.4.1.1 Results for self-ISF

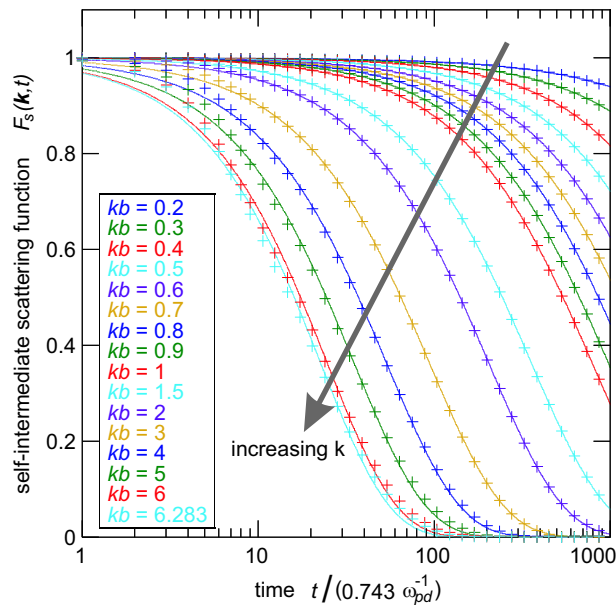


Figure 6.2: Time dependence of the self-ISF for various wavenumbers ( $k$ ) for the Langevin molecular dynamics (MD) simulation in the liquid regime:  $\Gamma = 200$ ,  $\kappa = 2$  and  $\nu/\omega_{pd} = 0.027$ . The solid lines are the corresponding fits to Eq. (6.5).

Relaxation results from my Langevin simulations are presented in Fig. 6.2 for typical liquid conditions far from the phase transition. Curves are shown as functions of time for various values of  $k$ . Note the smooth and gradual decay from unity to zero as time increases, without any plateau. The lack of a plateau in the time-variation of the self-ISF is similar to what is seen in granular flows [64, 65], but different from what is expected for supercooled liquids and glasses (cf. Fig. 3 of [123]).

To help quantify the relaxation that is observed in Fig. 6.2, I fit the time time-dependence of the self-ISF to the empirical form Eq. (6.5). Since the relaxation process spans many decades of time, to perform this fit without biasing results toward long times, data points were sampled from the simulation results at time intervals equally spaced on a logarithmic scale. For a liquid far from the phase transition, Eq. (6.5) (shown as solid lines in Fig. 6.2) fits my simulation data points well. The two free parameters for the fit,  $\tau(k)$  and  $\beta(k)$ , help quantify the relaxation process. I discuss their physical significance below.

#### 6.4.1.2 Searching for anomalous diffusion

I develop two tools for identifying anomalous diffusion. Previous investigators have usually used the MSD, looking for a scaling with time that differs from the  $\text{MSD} \propto t$  scaling expected for normal diffusion [31, 104, 106, 109, 110]. Data are typically fit to the form

$$\langle r^2(t) \rangle = 4D t^\alpha, \quad (6.9)$$

where  $\alpha = 1$  is the case of normal diffusion,  $\alpha > 1$  is superdiffusion, and  $\alpha < 1$  is subdiffusion. (This use of the symbol  $\alpha$  has no relation to the  $\alpha$  relaxation mentioned above.) Here I introduce two other tools that are also based on how random motion develops with time: the scaling with  $\tau$  vs.  $k$ , and the value of  $\beta$ , where  $\tau$  and  $\beta$  are the fitting parameters for Eq. (6.5).

My first new tool is the power-law scaling of the fitting parameter  $\tau$  as compared to  $k$ . To do this, I must first generalize Eq. (6.4) to allow for anomalous diffusion. Starting from Eq. (6.2), previous authors [117, 124] have demonstrated that

$$F_s(\mathbf{k}, t) \simeq \exp\left(-\frac{k^2 \langle r^2(t) \rangle}{4}\right), \quad (6.10)$$

where I have substituted 4 in place of 6 in the denominator for two dimensions

instead of three. Next, I substitute Eq. (6.9) in Eq. (6.10), yielding

$$F_s(\mathbf{k}, t) \simeq \exp(-k^2 Dt^\alpha) = \exp(-D(k^{2/\alpha} t)^\alpha). \quad (6.11)$$

Examining the argument on the right-hand-side reveals the scaling

$$\tau \propto k^{-2/\alpha}. \quad (6.12)$$

In the case of normal diffusion,  $\alpha = 1$ , the scaling is  $\tau \propto k^{-2}$ , as previous authors have noted [64, 65, 117]. Here, I note that the superdiffusion case  $\alpha > 1$  has  $\tau$  varying with a lesser power. Thus, the signature of superdiffusion will be a slope weaker than  $-2$  when  $\tau$  is plotted vs.  $k$  using log-log axes.

My second new tool is the fitting parameter  $\beta$  for the self-ISF. Comparing Eq. (6.5) and Eq. (6.11), I see that the value of  $\beta$  is essentially the same as  $\alpha$ . The only difference is that when using actual data, the value of  $\beta$  is generated by a fit, while  $\alpha$  is generated by examining a log-log plot. The community of scientists who use the self-ISF traditionally use  $\beta$ , although until now it has not been used as an indicator of superdiffusion. Scientists who use MSD to characterize superdiffusion, on the other hand, traditionally use  $\alpha$ .

#### 6.4.1.3 Results for fitting self-ISF

For the conditions of a liquid far from the phase transition, I use my two tools (scaling of  $\tau$  vs.  $k$  and value of  $\beta$ ) to test for anomalous diffusion. I use my two MD simulations, Langevin and frictionless. Ott and Bonitz [106] previously varied the values of friction  $\nu$  and observation time over wide ranges, and using the MSD method prepared a diagram showing the conditions that favor normal diffusion or superdiffusion. This diagram, Fig. 3 of [106], predicts that the value of  $\nu$  which I use in my Langevin simulation will yield normal diffusion, while the  $\nu = 0$  case of my frictionless simulation will yield superdiffusion over any reasonable observation time. Here I test whether my two cases, analyzed using my two new tools, yield the

same conclusion as in [106].

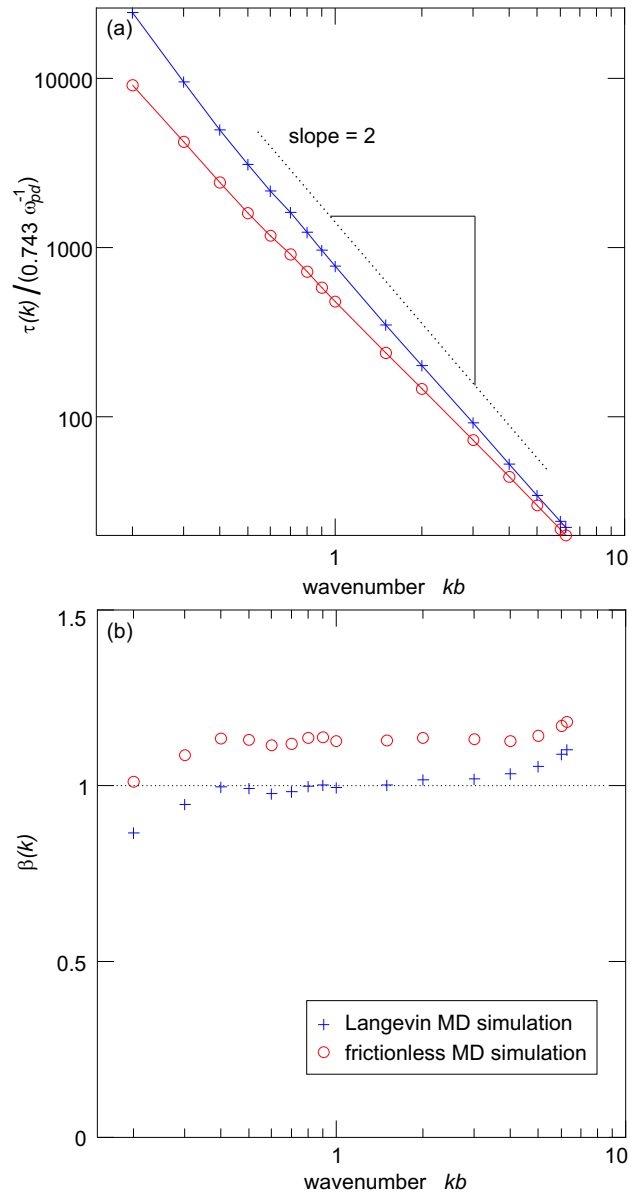


Figure 6.3: The fitting parameters, relaxation time  $\tau$  in (a) and exponent  $\beta$  in (b), as a function of  $k$ . These cross symbols are from fitting the data in Fig. 6.2 for the Langevin MD simulation, and the circle symbols are for the frictionless MD simulation for the same  $\Gamma = 200$ ,  $\kappa = 2$ .

For the  $\tau$  vs.  $k$  scaling, in Fig. 6.3(a) I find the scaling  $\tau \propto k^{-2}$  for the

Langevin MD simulations, and the scaling of  $\tau \propto k^{-\gamma}$  ( $\gamma < 2$ ) for the frictionless MD simulations. In other words, random motion is diffusive for my frictional (Langevin) case, but superdiffusive for my frictionless case. This is in quantitative agreement with Fig. 3 of [106], prepared using MSD curves, which demonstrated that friction can inhibit superdiffusion [104, 106].

For  $\beta$ , in Fig. 6.3(b) I find values near unity for my Langevin simulation, but a value definitely  $> 1$  for the frictionless simulation, for moderate values of  $k$ . This is again consistent with the conclusion of diffusive motion for my frictional (Langevin) case, but superdiffusive motion for the frictionless case. At extremely small or large values of  $k$ , however,  $\beta$  can be different. Figure 6.3(b) reveals an overall trend for  $\beta$  to increase with  $k$ , especially at extremely small or large values of  $k$ . Previous authors [64, 65] have identified dynamic heterogeneities as the cause for  $\beta < 1$  for very small  $k$ , i.e., very large length scales. For large  $k$ , previous authors have not reported enhanced values of  $\beta$  like those I see in Fig. 6.3(b). One possible interpretation of my large  $k$  observation is that it is affected significantly by caging motion rather than random walks associated with decaging in the short length scales.

To summarize, I find that the relaxation of the self-ISF is a sensitive indicator to distinguish normal diffusion from anomalous diffusion. The indication can be made using either of the two fitting parameters,  $\tau$  and  $\beta$ .

#### 6.4.2 Phase transition

Simulation studies of the solid-liquid phase transition, which is sometimes called an order-disorder transition, are generally done using measures of structural order, such as defects or correlation functions of particle position or bond orientation. A limitation of structural measures is that they do not clearly distinguish a supercooled liquid from a liquid above the melting point, because they have nearly

the same microscopic structure. This difficulty suggests a need for an indicator of the phase transition that is based on particle dynamics rather than structure.

My first goal, for phase transitions, is to test the use of the self-ISF as an indicator of the phase transition. I perform tests that indicate that it is sensitive in distinguishing solids and liquids near the phase transition. This development is useful because the self-ISF is based on dynamics rather than structure. My second goal is to determine what role friction plays in the phase transition. I will vary temperature and density, using the normalized quantities  $\Gamma$  and  $\kappa$ , and I will also vary the friction  $\nu$ , to determine whether the self-ISF is sensitive to phase, and what role friction plays.

#### 6.4.2.1 Dependence on $\Gamma$

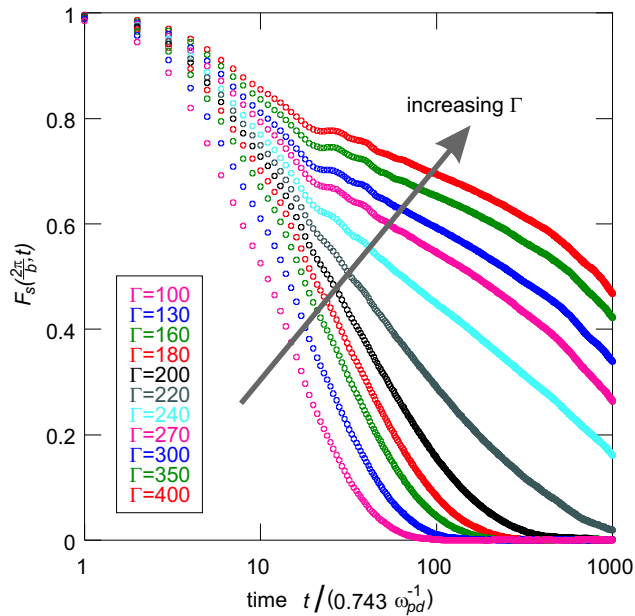


Figure 6.4: The self-ISF for the length scale corresponding to the lattice constant,  $k = 2\pi/b$ . Results shown are for the Langevin MD simulations with constant values of  $\kappa = 1.2$  and  $\nu/\omega_{pd} = 0.027$ , and varying  $\Gamma$ . A transition near  $\Gamma = 200$  is indicated by a change in the curve's shape, and by larger gaps between curves for solids,  $\Gamma > 200$ .

I find that the self-ISF time series undergoes a sudden change at the melting point. This is seen for the self-ISF in Fig. 6.4 for my Langevin simulation. Here, I have chosen to present results for a small wavenumber  $k_a = 2\pi/b$ , which is the wavenumber corresponding to a lattice constant so that the self-ISF indicates dynamics at the length scale of nearest neighbors. As I varied  $\Gamma$  in Fig. 6.4, I held  $\kappa = 1.2$  and  $\nu/\omega_{pd} = 0.027$  as constants.

I note two features of the self-ISF curves in Fig. 6.4 that are different on either side of this sudden change. First, the gap between curves is much wider for low temperature (high  $\Gamma$ ) conditions in the upper right of the figure as compared to the high temperature conditions in the lower left. I varied  $\Gamma$  in small steps near  $\Gamma = 200$ , where I find the sudden change in the gaps between the self-ISF curves. Second I identify a different shape for the decay of the self-ISF for low and high temperatures. For the high temperature (low  $\Gamma$ ) conditions expected for liquids I found, in Sec. 6.4.1, that the self-ISF decays according to the empirical law Eq. (6.5), but for low temperatures I found that Eq. (6.5) does not come even close to the shape of the curves in the upper right of Fig. 6.4.

Comparing to previous simulations that used structural measures, I can confirm that the sudden change in the self-ISF curve corresponds to the phase transition. Using a measure of local orientation order that exhibited a large jump at the phase transition, a phase transition curve for  $\Gamma$  vs.  $\kappa$  was reported, Fig. 6 in [73]. Interpolating their results, I find that the phase transition occurs at about  $\Gamma = 200$ , for  $\kappa = 1.2$ , for a 2D Yukawa system modeled with a frictionless MD simulation. This result is consistent with the sudden change that I observed in my self-ISF curves for  $\kappa = 1.2$  in Fig. 6.4: first, the curve's shape is changed; second, the curves are narrowly spaced for liquids ( $\Gamma < 200$ ) and widely spaced for solids ( $\Gamma > 200$ ). (One difference in the simulations of [73] and mine is my use of friction comparable

to values in 2D dusty plasma experiments. I will explore the role of friction in Sec. 6.4.2.4.)

Thus, I conclude that the self-ISF curve is very sensitive to phase. It shows promise to become a reliable indicator of the phase transition, although further tests, for different physical parameters, would be needed to confirm its reliability. An attraction of this method is that the self-ISF is a dynamical rather than structural measure.

#### 6.4.2.2 Dependence on $\kappa$

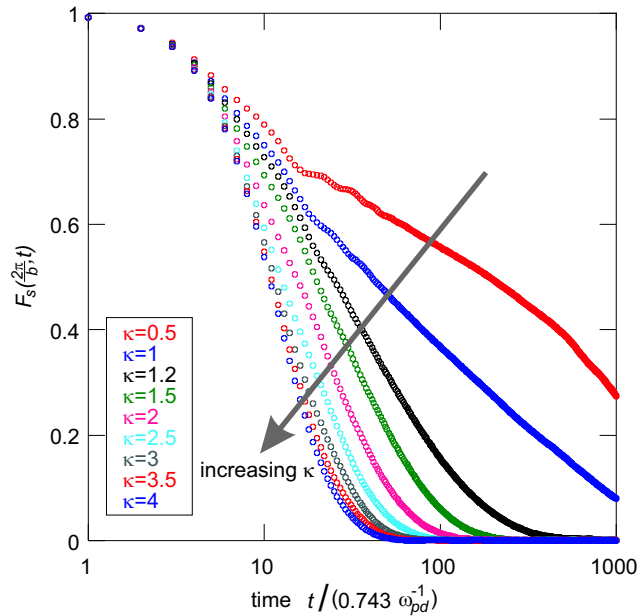


Figure 6.5: The self-ISF at  $k = 2\pi/b$ , as in Fig. 6.4 but with varying  $\kappa$ . The simulations here are all Langevin MD simulations with constant values of  $\Gamma = 200$  and  $\nu/\omega_{pd} = 0.027$ . A transition near  $\kappa = 1.2$  is indicated by a change in the curve's shape, and the gaps between curves.

Varying only the density or  $\kappa$ , I again find the same two results as for varying  $\Gamma$ . There is a sudden change in the gaps between curves, and the curves take a different shape at a point that I can identify as the phase transition. This is

seen in Fig. 6.5, where I changed  $\kappa$  in my Langevin simulations with  $\Gamma = 200$  and  $\nu/\omega_{pd} = 0.027$ . The transition occurs at  $\kappa = 1.2$ , which is consistent with Fig. 6 in [73].

#### 6.4.2.3 Structure relaxation time

I investigate how rapidly disorder develops on the length scale of a cage, i.e., the interparticle spacing  $b$ . I will test whether it occurs with an Arrhenius or Vogel-Fulcher law as in other complex fluids such as colloids [125], granular materials [65], supercooled liquids and glasses [126]. I carry out this investigation by characterizing a decay time for the self-ISF. I could use the fit parameter  $\tau(k)$  from Eq. (6.5), but for simplicity, rather than fitting the self-ISF, here I will adopt the practice of other authors of measuring the time required for the self-ISF to decay by a factor of  $1/e$  [125, 126]. This is done only for  $k = 2\pi/b$ , corresponding to the length scale of a cage. This  $1/e$  decay time, denoted here as  $\tau_{2\pi/b}$ , is called the ‘‘structure relaxation time,’’ and is in principle the same as  $\tau$  if  $\beta = 1$ .

Results for the structure relaxation time  $\tau_{2\pi/b}$  for the curves of Figs. 6.4, and 6.5 are shown in Fig. 6.6, revealing how  $\tau_{2\pi/b}$  varies with temperature and number density. As the normalized temperature  $1/\Gamma$  increases, the system melts and  $\tau_{2\pi/b}$  decreases about one order of magnitude. Melting also occurs as  $\kappa$  is increased. Plotting  $\tau_{2\pi/b}$  vs. number density, in the inset of Fig. 6.6(b), I note a nearly linear scaling in the liquid regime.

The scaling I observe for  $\tau_{2\pi/b}$  vs. number density is different from the Arrhenius and Vogel-Fulcher laws. The Vogel-Fulcher law, which has been found empirically for other complex fluids [65, 125, 126], has  $\tau_{2\pi/b}$  diverging to infinity as the number density increases toward the phase transition point. Here,  $\tau_{2\pi/b}$  increases about an order of magnitude near the phase transition, but it does not diverge.

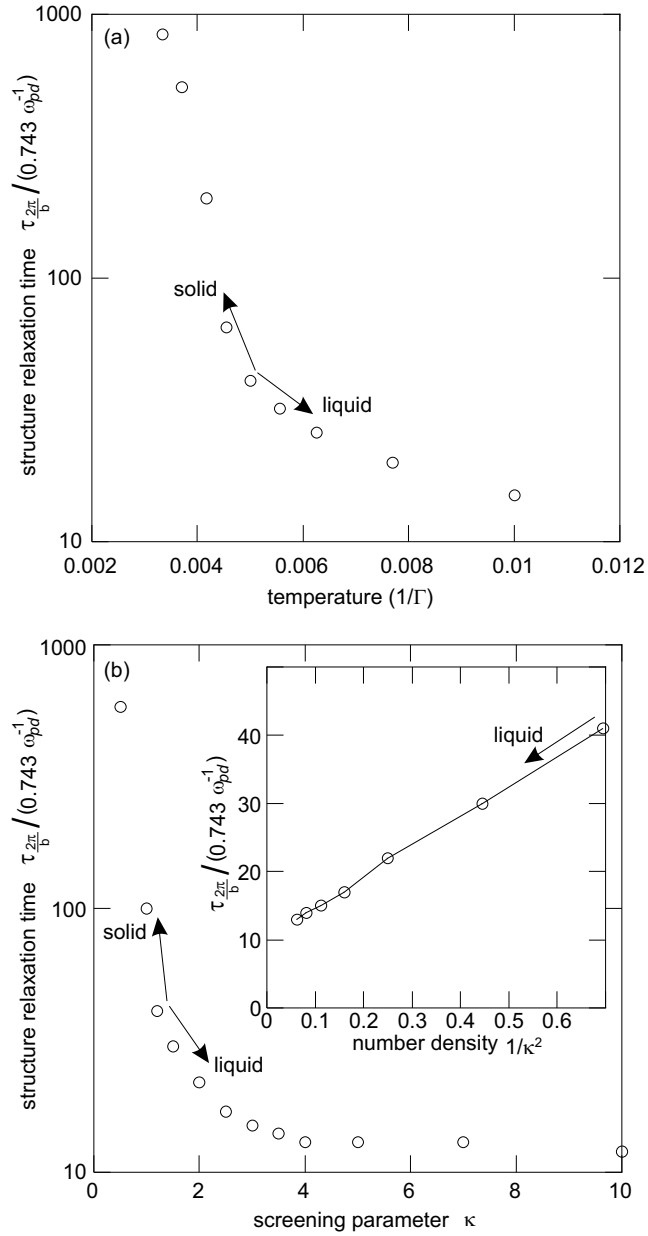


Figure 6.6: Structure relaxation time measured from Figs. 6.4 and 6.5 as a function of (a) temperature and (b) screening parameter  $\kappa$ . The structure relaxation time in my 2D underdamped Yukawa system does not obey the Arrhenius law or Vogel-Fulcher law. The same data are plotted in the inset as a function of number density  $1/\kappa^2$ , for the liquid regime.

#### 6.4.2.4 Dependence on $\nu$

I find that friction also plays an important role in the random motion of 2D Yukawa liquids, but only at large damping rate. This result is shown in Fig. 6.7

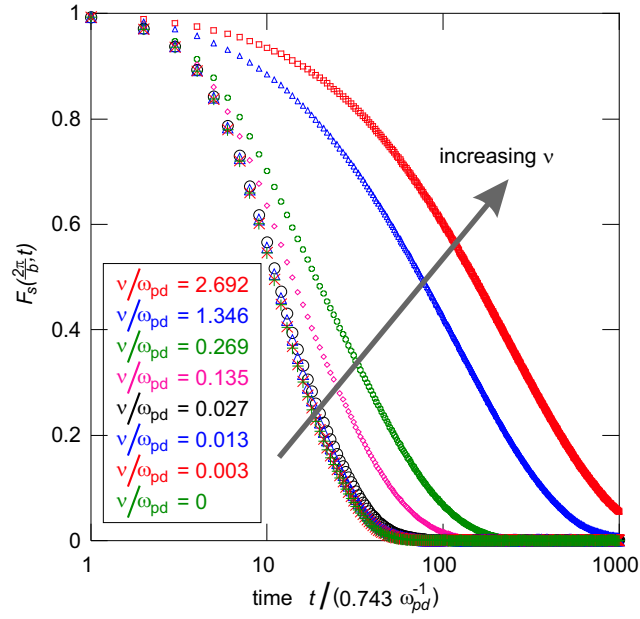


Figure 6.7: The self-ISF at  $k = 2\pi/b$  for the simulations at different damping rate  $\nu$ . The simulations here include both Langevin MD simulations and frictionless MD simulations in a liquid regime, with constant values of  $\Gamma = 200$  and  $\kappa = 3$ . Unlike temperature and number density, changing the friction does not significant change the shape of the curves. The effect of friction in the self-ISF curves is a retardation of the decay at higher damping rate.

where I varied  $\nu$  while holding  $\Gamma$  and  $\kappa$  constant in a liquid regime. I observe that the self-ISF curves all lie on top of one another for  $\nu/\omega_{pd} \lesssim 0.03$ , but not at higher damping rates where they decay more slowly as  $\nu$  is increased. The curves at higher damping rates have the same general shape, but are retarded in time. For the limiting case of no friction, I also include in Fig. 6.7 results for my frictionless equilibrium MD simulation, and these agree with the Langevin simulation for low friction  $\nu/\omega_{pd} \lesssim 0.03$ .

I interpret the difference in the  $F_s(\mathbf{k}_a, t)$  curves at various damping rates as indicating retardation of diffusive motion at high friction levels. At higher damping rate, the random motion of particles is resisted, then more energy is dissipated locally. As a result, the collective relaxation, which refers to the diffusive motion,

will be retarded.

## CHAPTER 7

### ACCURATE PARTICLE POSITION MEASUREMENT FROM IMAGES

Dusty plasma experiments are distinguished by a unique diagnostic: direct imaging of all discrete particles in the plasma. This capability is important for the study of strongly-coupled plasmas because they must be understood at the level of discrete particles due to the dominant pairwise Coulomb interaction of particles. After an image is recorded, showing hundreds or thousands of particles, the  $x - y$  coordinates of a particle position can be calculated using the moment method, which is an image analysis technique for sub-pixel estimation of particle positions. The total error in the calculated particle position includes effects of pixel locking and random noise in each pixel. Pixel locking, also known as peak locking, is an artifact where calculated particle positions are concentrated at certain locations relative to pixel edges.

After calculating a particle's position, I calculate its velocity as the displacement of the particle in two consecutive frames divided by the time interval between frames. Additionally, I can compute a time series of a particle's velocity  $\mathbf{v}(t)$  by tracking its motion over many consecutive pairs of frames. This method is called particle tracking velocimetry (PTV). As compared to methods used for measuring weakly-coupled plasmas, this method quantifies plasma dynamics at the level of discrete particles. In the fields of fluid mechanics and condensed matter physics, these methods of imaging are sometimes termed "video microscopy," which provides a capability to perform experimental simulation of condensed matter at an "atomistic scale."

In this chapter, I report calculations to gain an understanding of the sources of error and their dependence on parameters that the experimenter can control. I

recommend an algorithm for experimenters to choose optimal parameters to minimize total error and pixel locking. These results should be useful in other fields, such as colloids, biology, and fluid mechanics, where particle positions are measured using video microscopy.

The results in this chapter correspond to Y. Feng, J. Goree, and B. Liu, “*Accurate particle position measurement from images,*” *Review of Scientific Instruments*, Vol. 78, article number 053704 (2007).

## 7.1 Introduction

Measurement of particle positions from images is important in many fields, including dusty plasmas [127, 128], colloids [129, 130], fluid mechanics [131], biology [132], and computer vision [133]. Particle positions are generally estimated as the center of a bright spot of an image. Velocities can also be calculated from images; two common methods for this are Particle-Tracking-Velocimetry (PTV) and Particle-Image-Velocimetry (PIV).

To measure particle positions, an experimenter begins with a bit-map image. As an example, in Fig. 7.1 I present portions of single video frame from a dusty plasma experiment. Each bright spot represents an  $8\ \mu\text{m}$  diameter polymer microsphere illuminated by a  $0.633\ \mu\text{m}$  helium-neon laser sheet and imaged by a video camera with a Nikon 105 mm micro lens and a bandpass optical filter to eliminate unwanted light. The lens was focused to generate a sharp image. The experimental setup is similar to Fig. 2 of [127]. Figure 7.1(a) and a magnified view Fig. 7.1(b) show portions of a video frame recorded by a cooled 14-bit digital camera (pco1600) with a  $7.4\ \mu\text{m}$  pixel width and a linear response. It was operated at 30 frames per second with an exposure time of 30 msec. I should mention that experimental images of particles will differ, depending on many factors including the type of camera. To illustrate this point, I present in Fig. 7.1(c) an enlarged view of a bright spot in

a frame recorded by an analog camera with a nonlinear response corresponding to  $\gamma = 0.6$ . (Some cameras are nonlinear with an output intensity proportional to the input luminance to the power  $\gamma$ ).

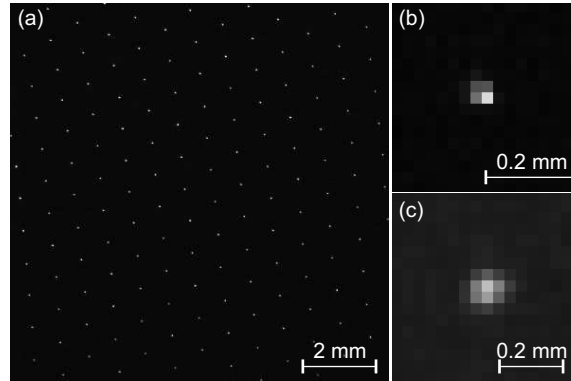


Figure 7.1: Experimental bit-map images of a monolayer suspension of microspheres in a dusty plasma. Each bright spot corresponds to one particle. Here, (a) is  $1/12$  of the original image from a digital camera and (b) is a magnified view, showing that a bright spot fills several pixels, while in (c) from an analog camera a bright spot fills about  $5 \times 5$  pixels. Spot size depends on such factors as camera type and focusing. A particle's position is calculated as the bright spot's center; errors in this calculation are the topic of this chapter.

In the images in Fig. 7.1, particles fill several pixels. This spot size may be due, in part, to diffraction by the particle as well as camera properties such as diffraction by the camera aperture [134] and imperfect lens focusing. The spot size cannot be explained merely by geometrical optics, because the small particle size and magnification would result in an image smaller than one pixel on the camera detector.

Images have random noise in each pixel. This can arise because of fluctuations in the camera's sensor and its electronics. Noise in the experimental image of Fig. 7.1(a) is shown in Fig. 7.2 as a histogram of the pixel intensity. The most prominent feature is the noise peak, corresponding to a large number of pixels

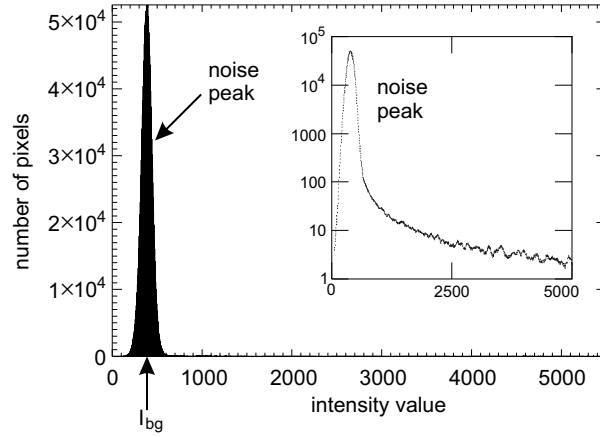


Figure 7.2: Histogram of intensity values of pixels in the original experimental image of Fig. 7.1(a). The inset shows the same data with a logarithmic scale. The prominent peak, centered at  $I_{bg}$ , is due to noise in the camera.

that are relatively dark. This noise peak has an average value that I term the “background intensity,”  $I_{bg}$ . The noise peak generally depends only on the camera and the sensor temperature.

After recording a bit-map image, the experimenter will then use a computer algorithm to measure the particle position. There are several methods to do this, including the moment method [14, 127, 128, 135, 136], which I will study in this chapter. Other methods include fitting a bright spot in the image to a Gaussian [137] or polynomial [128, 130], and simpler methods such as choosing the centroid as the particle center [128, 136]. In the moment method, the calculated particle position is

$$\mathbf{X}_{calc} = \frac{\sum_k \mathbf{X}_k I_k}{\sum_k I_k}, \quad (7.1)$$

where  $\mathbf{X}_k$  is the position and  $I_k$  is the intensity of a pixel  $k$ . The result of Eq. (7.1) is sometimes called the “center of mass” [136]. When the particle fills more than one pixel, this calculation yields an estimate of the particle position with sub-pixel accuracy. Because of the efficiency and accuracy of the moment method, it is widely

used when analyzing large quantities of data, as might be produced for example when using a video camera. Fitting methods, which are more computationally expensive, are often used as well [137]. The centroid method is similar to the moment method except that the intensity  $I_k$  of each pixel is replaced with a constant [128, 136].

One application of particle position measurements is the calculation of particle velocities using PTV. A velocity can be calculated by subtracting the positions of the same particle in two different frames and dividing by the time interval between frames. This method differs from PIV [138], where velocities are calculated at regular gridpoints, not for specific particles.

Errors in the calculated particle position arise from multiple sources, including random noise in each pixel and also from the finite spatial resolution of the pixels on a camera sensor. When an image is recorded by sampling it with a finite number of pixels, some information about the intensity profile is lost, and this can cause a type of systematic error known as pixel locking or peak locking. The total error in the calculated position will be due to a combination of these effects, not just random noise or pixel locking by itself.

In this chapter, I seek to minimize the total error, and doing this will require that I understand the contribution of pixel locking. My goal is to aid the experimenter in making optimal choices, in both hardware and software, to minimize the total error.

## 7.2 Pixel locking

Pixel locking, also known as peak locking, is an artifact where calculated particle positions tend to be concentrated at certain favored locations relative to pixel edges, such as the center or edges of a pixel. It is different from random errors, which do not result in favored positions for particles. To understand pixel locking,

consider a particle whose image fills only a single pixel. In this case, the sum in Eq. (7.1) would have only a single term, and the position would be assigned to the exact center of that pixel. If the particle's image instead fills two pixels with equal intensity, the position will be assigned to the midpoint of a pixel edge. The pixel center and midpoints of pixel edges are examples of favored positions that are found to occur even when the particle's image fills several pixels [82].

The scientific literature for pixel locking includes many papers where PIV is used to measure velocities. In the early 1990s, the PIV method was tested to demonstrate their sub-pixel accuracy for particles flowing along with a fluid [139, 140]. For specific applications of PIV, pixel locking has been studied by other authors as well [141, 142, 143, 144]. In comparison to PIV, the literature for PTV includes fewer studies of pixel locking, e.g. [82, 145]. Because of this, some users of PTV, including until recently us, were unaware of pixel locking and the problems it can cause. In addition to PTV, computer vision is another important area where pixel locking is recognized as a problem in measuring positions [133, 146, 147].

To detect pixel locking, I use sub-pixel maps as a diagnostic tool. A sub-pixel map shows all the calculated particle positions relative to pixel edges, and it is drawn in a small box having the size of one pixel. To prepare a sub-pixel map, I begin with a graph of calculated positions of  $N$  particles, as illustrated in Fig. 7.3(a), then plot the fraction parts of these positions in the small box, yielding the sub-pixel map in Fig. 7.3(b). In Fig. 7.3(c) I present an actual sub-pixel map calculated from a bit-map image by an analog camera in a dusty plasma experiment. The signature of pixel locking can be identified in general by concentrations of calculated particle positions at favored positions. These favored positions can vary, depending on both hardware and software, but they commonly include the center or edges of a pixel, as in Fig. 7.3(c). Sub-pixel maps are therefore very useful for detecting pixel locking.

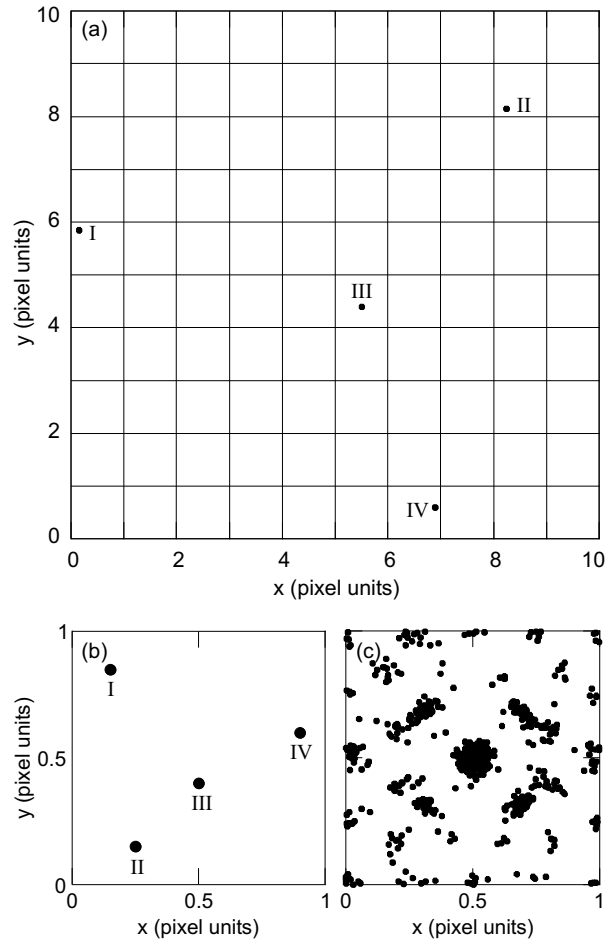


Figure 7.3: Illustration of the method for calculating a sub-pixel map. First, a  $10 \times 10$  pixel bit-map image (not shown here) is analyzed to yield a map (a) of particle positions. Second, the same positions are plotted relative to pixel edges in (b); these values are the fraction parts of the calculated positions. (c) An example sub-pixel map of  $N = 617$  particles, calculated from an experimental image (full view of Fig. 7.1(c)), reveals pixel locking as a tendency of calculated positions to be concentrated at favored positions including the center and edges of pixels.

Other authors have used similar graphs, where the calculated positions have been binned and plotted as a histogram [133, 146, 147].

### 7.3 Moment method

The algorithm I optimize in this chapter, the moment method, has two main steps. The first step is the selection of pixels that belong to each particle in the image. The second step is the calculation of position as an intensity-weighted moment of pixel positions.

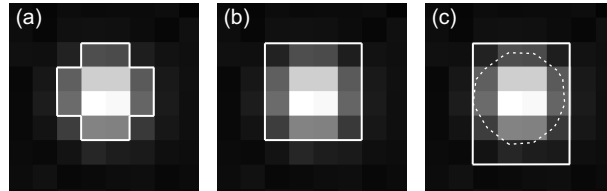


Figure 7.4: Illustration of boundaries. In algorithms for calculating particle positions from a bit-map image, the first step is selecting the contiguous pixels to be used, as defined by a boundary (solid white line) that encloses them. The codes tested here differ only in the way they select boundaries. (a) In ImageJ, only contiguous pixels above a threshold are included in the boundary. Code A (b) and Code K (c) use boundaries that are the smallest rectangles that enclose: all the contiguous pixels above the threshold in Code A, or the dashed contour produced by a 2D contour-plotting routine in Code K.

In the first step, the selection of pixels, the user begins by choosing a threshold  $I_{th}$ . The gray-scale image is replaced by a black-and-white image, where pixels brighter than  $I_{th}$  become black, and all others become white. The choice of the threshold is important for several reasons [135], as I will discuss later. Next, the boundaries for individual particle images are determined. There are several algorithms for selecting boundaries. I have examined several codes that use the moment method, and I found that the only difference is the algorithm for selecting boundaries. I will consider three algorithms, which I distinguish by the corresponding codes I will test. All three of these codes are well tested, and they generate reliable results from experimental images. In one algorithm, the boundary is selected to be a polygon that encloses only contiguous pixels brighter than the threshold, Fig. 7.4(a).

This algorithm is used in the freely available ImageJ [136] code. The other two algorithms select a boundary that is a rectangle. In Code A, the boundary is the smallest rectangle that encloses all the contiguous pixels above the threshold [148], Fig. 7.4(b). In Code K, the boundary is the smallest rectangle that encloses a special curved contour [149]. This curved contour is produced by a 2D contour-plotting routine, and it is drawn not as line segments around pixel edges but rather as a curve passing through various pixels. Within a pixel, the pixel center is assigned the value of the original pixel intensity, but other points within a pixel are assumed to have other intensities, which are calculated by 2D interpolation using four surrounding pixel centers. Then, the contour-plotting routine draws a curve by joining all points, with sub-pixel spacing, where the assumed intensity is equal to the threshold, as shown in Fig. 7.4(c) with a dash line. In both Codes A and K, but not ImageJ, the boundary can enclose some pixels that are less intense than the threshold.

In the second step, which is the same in all three codes I test, the particle positions are calculated as the moment, i.e., as the intensity-weighted position of pixels. The moment can be calculated [14, 127, 135] using Eq. (7.1). However, I will find it better to use a generalized form of the calculated particle position,

$$\mathbf{X}_{calc} = \frac{\sum_k \mathbf{X}_k (I_k - I_{base})}{\sum_k (I_k - I_{base})}, \quad (7.2)$$

where the baseline value  $I_{base}$  will be explained later. Note that the calculated particle position depends on the selection of pixels that are included in the summation in Eq. (7.1) or Eq. (7.2).

## 7.4 Method

### 7.4.1 Synthetic images

To test methods of measuring particle positions, I calculate position errors as compared to true positions in synthetic images. For this purpose I cannot use actual

experimental images because the true position is generally not known. Synthetic images allow us to vary the intensity and the size of a bright spot to find how errors depend on these parameters.

Units used in this chapter are pixel units for all distances including  $\mathbf{X}_k$ ,  $\mathbf{X}_{calc}$ , spot size and errors. Intensities, including signal and noise, are specified in intensity value units, i.e., a dimensionless integer ranging, for example, from 0 to  $2^{14} - 1$  for a 14-bit camera.

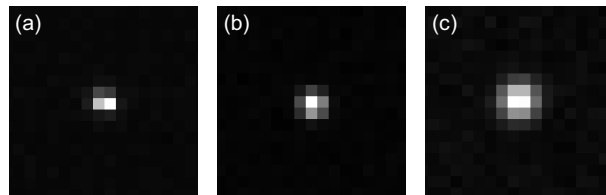


Figure 7.5: Magnified images of bright spots. (a) Experimental image from a digital video camera. (b),(c) Synthetic images, with a Gaussian profile centered on a known true position, here with two different spot radii. In generating synthetic images, I first choose the true position randomly, and then calculate the intensity of each pixel using Eq. (7.5) so that it includes both signal and noise.

I prepare synthetic images that resemble an experimental image like Fig. 7.5(a). The synthetic images have a size of  $64 \times 64$  pixels, with one bright spot per image. These images have three major attributes that I compute: the spot's true position, the spatial profile of the signal, and the noise.

First, the bright spot's true position is located near the image center, but displaced in the  $x$  and  $y$  directions by a fraction of a pixel. This is done using random numbers with a uniform distribution (between 0 and 1) so that the true positions are random and uniformly-distributed relative to pixel edges. Using these random positions avoids any sampling bias.

Second, like other authors [129, 150], I model the signal's spatial profile as a

Gaussian

$$I_{sig}(x, y) = I_{peak} \exp \left[ -\frac{(x - x_{true})^2 + (y - y_{true})^2}{r_{spot}^2} \right], \quad (7.3)$$

characterized by the spot radius  $r_{spot}$  and the peak intensity  $I_{peak}$ . (This Gaussian is intended to approximate the actual spatial profile, which depends on factors such as the particle size, the camera's gamma, and lens defocusing.) To imitate the collection of light onto a square pixel, I integrate this smooth profile over each pixel's area. This yields the value  $I_{sig\ k}$  of the signal in pixel  $k$ ,

$$I_{sig\ k} = \int_{x=k_x-0.5}^{k_x+0.5} \int_{y=k_y-0.5}^{k_y+0.5} I_{sig}(x, y) dx dy, \quad (7.4)$$

where  $k_x$  and  $k_y$  are the coordinates of pixel  $k$ . Equation (7.4) combined with Eq. (7.3) can be evaluated efficiently using the error function *erf*. (After this step, each bright spot has the same total signal intensity  $\sum I_{sig\ k}$ , which was typically 37707 corresponding to the brightest spot in the experimental image Fig. 7.1(a). In the experiment, not every bright spot has the same total signal intensity because some particles are levitated slightly above or below the brightest part of the horizontal laser sheet.)

Third, I calculate a noise value  $I_{noise\ k}$  which is different for each pixel  $k$ . To simulate the experiment,  $I_{noise\ k}$  is chosen as a random intensity from the noise distribution of my digital camera, Fig. 7.2, which is centered at an average intensity  $I_{bg} = 384$ . Finally, the intensity  $I_k$  in each pixel is calculated as the sum of the intensities of the signal and noise or a saturation value  $I_{sat}$ , whichever is smaller,

$$I_k = \text{Min}[(I_{sig\ k} + I_{noise\ k}), I_{sat}]. \quad (7.5)$$

I use  $I_{sat} = 2^{14} - 1$  to simulate the saturation intensity of a real camera with 14-bit resolution. Finally, I round  $I_k$  to an integer because cameras produce integer values for the intensity of each pixel. The result of this calculation is a TIFF image like Fig. 7.5(b) or 7.5(c).

Here I only consider bright spots that are circular, as in Eq. (7.3). Although I do not simulate them here, I note that non-circular bright spots can be analyzed using the moment method, and they do occur in some experiments. Elliptical particles arise when using analog video cameras with a limited horizontal resolution, or when particles move rapidly during the exposure time. The latter effect can be diminished by rastering a laser beam rather than dispersing it into a constant sheet. Defocusing a lens can result in non-circular spots, as in Sec. 7.7.

#### 7.4.2 Errors in calculated particle positions

In this chapter, I am mainly interested in errors in calculated particle positions. In addition to errors in particle position, the experimenter may also be concerned with errors in velocities and other quantities computed from particle positions, as discussed in the Appendix B.

To characterize the error in calculated particle positions, I use two diagnostics. First, I calculate sub-pixel maps, as described in Sec. 7.2. Examining these sub-pixel maps qualitatively will reveal pixel locking, which is one source of error. Second, I characterize the total error, including both random errors and pixel locking, as the root-mean-square (rms) difference of true and calculated positions, i.e., the rms error

$$\left[ \frac{1}{N} \sum_{m=1}^N (x_{m,calc} - x_{m,true})^2 + (y_{m,calc} - y_{m,true})^2 \right]^{\frac{1}{2}}, \quad (7.6)$$

where  $m$  and  $N$  are the index and total number, respectively, of bright spots. While I can calculate the total error using Eq. (7.6), I cannot separately calculate the contributions from random errors and pixel locking.

To achieve good statistics, I prepared over 370 000 synthetic images, each with one bright spot. I used  $N = 5000$  when calculating the rms error, and  $N = 100\,000$  when calculating sub-pixel maps. All of these images have different random

true positions for their bright spots, and the noise in each pixel is different in all images.

### 7.4.3 Parameters

To find a procedure for calculating position with minimal total error, I will test three different codes, and I will vary parameters corresponding to software and hardware adjustments that an experimenter can make. I will now list these adjustments. The experimenter can choose to focus the camera lens sharply, or defocus it to make the bright spots in the image appear larger and fill more pixels. As a second parameter, the experimenter can adjust the image intensity by varying the camera aperture, exposure time or illumination brightness. After recording images with the camera, the experimenter will then use software. Here, I test three moment method codes, as explained in Sec. 7.3. After choosing a code, the experimenter can usually adjust two parameters in that code: the threshold used in the first step, and the baseline (if any) that is subtracted in the second step, as in Eq. (7.2).

Thus, I am motivated to analyze the impact of the following four parameters that the experimenter must choose: focus, intensity, threshold, and baseline. I do this by varying the values of  $r_{spot}$  (keeping the total signal intensity  $\sum I_{sig\ k}$  as constant, as explained later),  $I_{peak}$ ,  $I_{th}$ , and  $I_{base}$ , respectively. I will vary each of these four parameters in Sec. 7.5. I will also compare results from the three different codes. The outcome of this analysis will be a practical procedure, presented in Sec. 7.6, that the experimenter can use to minimize errors in calculated positions.

## 7.5 Results

### 7.5.1 Threshold

The first parameter I vary is the threshold. The experimenter will first choose a coarse range of threshold so that it is not so low that noise is wrongly identified as particles and not so high that fainter particles are overlooked. Then, within this coarse range, a fine adjustment can be made to reduce error. Here, I consider the fine adjustment.

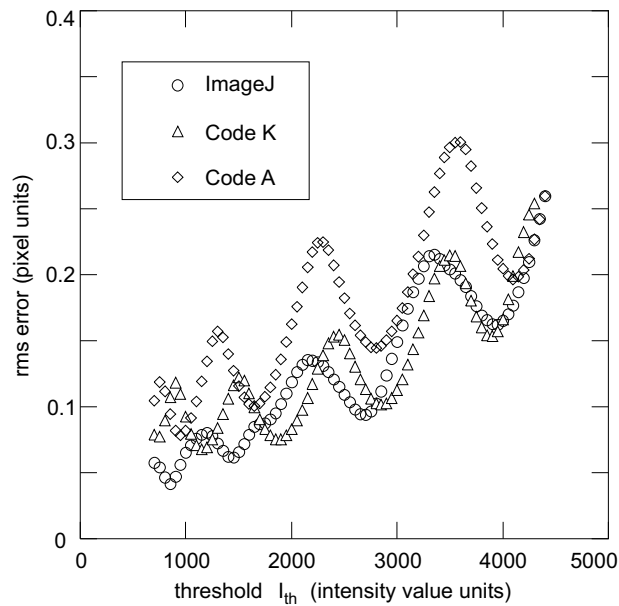


Figure 7.6: The rms error of calculated positions as a function of the threshold  $I_{th}$ . In general, errors increase with threshold, and superimposed on this increase is an oscillation. The rms errors are always calculated as in Eq. (7.6) using  $N = 5000$ . (Here,  $r_{spot} = 1.5$  pixel units,  $I_{peak} = 5334$  intensity value units, corresponding to a total signal intensity  $\sum I_{sig\ k} = 37\ 707$ . Also,  $I_{base} = 0$ .)

My results in Fig. 7.6 show that the total error generally increases with threshold, and it also depends on the choice of a code. I calculate the total error as the rms error, using  $N = 5000$  images and Eq. (7.6). Recall that the total error includes

both random and pixel-locking errors. The total error generally increases with the threshold because raising the threshold can eliminate pixels that have useful signal.

threshold	boundaries (for three true positions)		
	TP1 (32.41, 32.16)	TP2 (32.40, 32.47)	TP3 (32.00, 32.01)
800			
1000			
1200			
1400			

Figure 7.7: Cause of oscillations. Boundaries, selected in the first step of ImageJ, enclose fewer pixels as the threshold is increased. Removing one pixel from the boundary causes a discrete jump in the calculated particle position in Eq. (7.2). As the threshold increases, there is a sequence of jumps, as the boundary becomes smaller, one pixel at a time. These jumps, in aggregate for many particles, lead to oscillations in the rms error as the threshold is varied, a phenomenon I term the boundary effect. The three columns correspond to three different true positions.

The total error exhibits not only a general increase with threshold, but also an oscillation. This is seen in Fig. 7.6, where there are several oscillations superimposed on the general trend. I cannot dismiss these oscillations as mere statistical fluctuations because I achieved good statistics by using 5000 particle positions. To identify the cause of these oscillations, I tested how the boundaries that are selected in the first step depend on the threshold. The result of this test is shown in Fig. 7.7 as a table of the boundaries selected by ImageJ. When the threshold is increased slightly so that the boundary shrinks by one pixel, there is a discrete jump in the calculated particle position. As the threshold increases, there is a sequence of jumps,

as the boundary becomes smaller, one pixel at a time. These jumps, in aggregate for many particles, lead to oscillations in the rms error as the threshold is varied, which is the phenomenon I term the “boundary effect”.

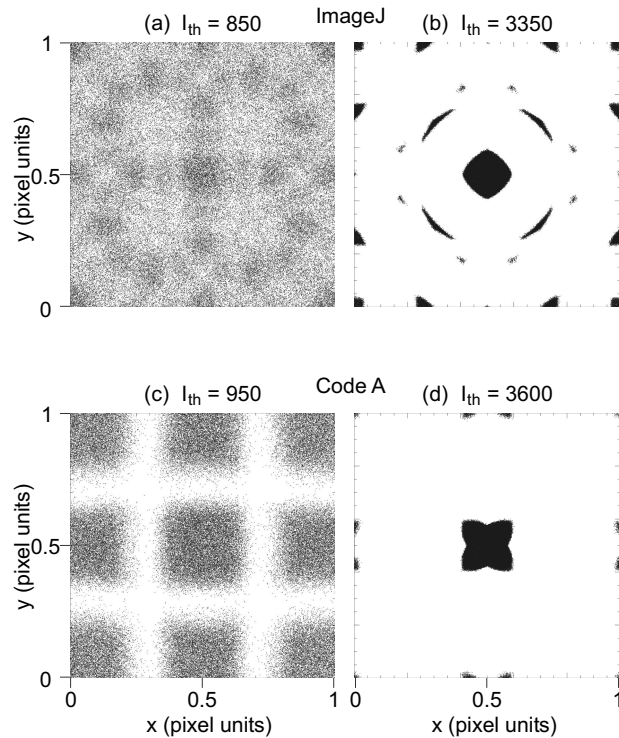


Figure 7.8: Sub-pixel maps for  $N = 100\,000$  randomly distributed true positions. The signature of pixel locking is generally more severe for higher thresholds. (Here,  $r_{spot} = 1.5$ ,  $I_{peak} = 5334$ , and  $I_{base} = 0$ .)

To identify the role of pixel locking in the total error, I examine sub-pixel maps in Fig. 7.8, which reveal the importance of the threshold. For ImageJ, I provide sub-pixel maps, Fig. 7.8(a) and 7.8(b), that correspond to the two thresholds that yielded the minimum and maximum rms errors, respectively, in Fig. 7.6. I note that the signature of pixel locking is weaker, i.e., the sub-pixel map is more uniform, for the case of the low threshold, Fig. 7.8(a), that yields the lowest total error. Conversely,

the signature of pixel locking is stronger, i.e., the sub-pixel map has strongly non-uniform features, for the higher threshold, Fig. 7.8(b). In general, reducing the threshold will reduce pixel locking. Other codes exhibit the same trend, but with a different appearance for the sub-pixel maps, as in Fig. 7.8(c) and 7.8(d).

### 7.5.2 Spot radius

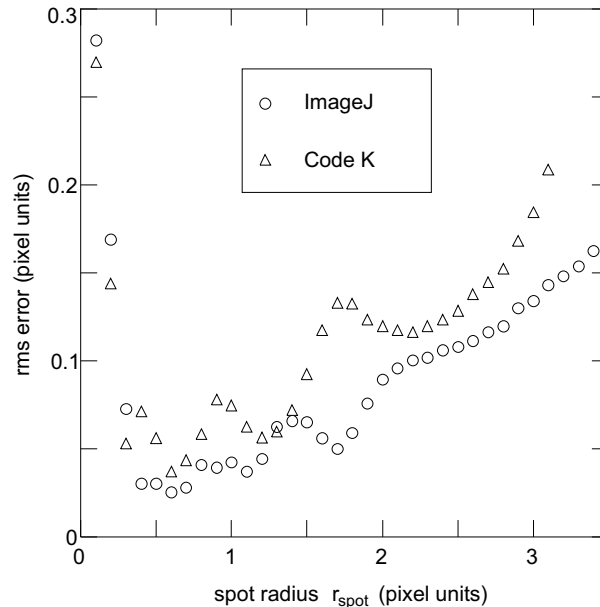


Figure 7.9: Simulation of slight lens defocusing. The optimal range of spot size lies between two other ranges: for very small  $r_{spot}$ , errors worsen due to pixel saturation; for very large  $r_{spot}$ , they worsen due to random errors. For my parameters, these two ranges are for  $r_{spot} < 0.8$  and  $r_{spot} > 2.0$ , respectively. Oscillations in the optimal range arise from a boundary effect. (Here,  $I_{th} = 1000$ ,  $I_{base} = 0$ , and  $\sum I_{sig\ k} = 37\,707$ .)

To simulate an experimenter's slight defocusing of a camera lens, I varied the spot radius  $r_{spot}$  in Fig. 7.9. I used the Gaussian profile of Eq. (7.3), keeping the spot's total signal intensity ( $\sum I_{sig\ k}$  summed over all pixels) constant. In this way I mimic an experiment where a particle scatters the same finite number of photons

into a camera lens regardless of how the lens is focused. (I did not simulate the ring-shaped bright spot that can occur for extreme defocusing.) Defocusing can happen when an experimenter purposefully chooses to defocus the lens for example to avoid saturating pixels; in other cases, defocusing is not intentional but instead simply unavoidable because particles are at different depths, as for example in colloidal suspensions [130] and 3D dusty plasma suspensions [145].

Defocusing a lens during the experiment can actually be desirable. By distributing the signal over a larger number of pixels, the impact of a single pixel in the calculation of the particle's position is less, so that pixel locking becomes weaker. On the other hand, defocusing can reduce the signal in each pixel, so that the signal-to-noise ratio (SNR) in each pixel becomes worse. In other words, there can be a trade-off: defocusing can improve pixel locking at the expense of making random errors worse. In my results below I investigate this effect.

I should mention that when discussing defocusing, I always refer to the experimenter's adjustment to the hardware when recording an image. Unlike some other methods [129], here I do not blur an image in software after it has been recorded by the hardware.

The result in Fig. 7.9 reveals three ranges of the spot radius, where the second range is the most desirable. In the first range, with small spot radii ( $r_{spot} < 0.8$ ), the total error diminishes with radius because the spot includes a saturated pixel. Saturated pixels are undesirable because they introduce wrong information for intensity into Eq. (7.2). In the second range, with slightly larger spot radii ( $0.8 \leq r_{spot} \leq 2.0$ ), the total error is smallest. In the third range, with large spot radii ( $r_{spot} > 2.0$ ), the total error generally increases with  $r_{spot}$  because the trade-off results in the undesirable outcome of the worsened SNR in each pixel having a stronger effect than the improved pixel locking due to defocusing. The optimal spot radius is somewhere

in the second range, which for my parameters is approximately 0.8 - 2.0. I should emphasize, however, that this range will vary depending on the experiment due to different cameras (with different noise levels, sensitivities and saturation levels), particle size, illumination, and working distance between particles and lens. If the camera had a higher noise level, the errors in this third range would be larger and the experimenter would be unable to use much defocusing. On the other hand, if the illumination were brighter, then the entire curve in Fig. 7.9 would shift toward larger spot radii and the experimenter would be able to use more defocusing.

In Fig. 7.9 I also note an oscillation, superimposed on the general trend, for  $0.8 \leq r_{spot} \leq 2.0$ . I attribute this oscillation, which was observed previously in experiments by Käding and Melzer [145], to a boundary effect similar to the one described above.

### 7.5.3 Intensity

To simulate adjusting the illumination brightness, the exposure time, or the camera aperture, I varied  $I_{peak}$  in Fig. 7.10. As a result, the total signal intensity  $\sum I_{sig\ k}$  is varied, while  $r_{spot}$  is kept constant. I note that ImageJ yields the smallest total error.

The trend that would be expected for random errors only is a downward slope as the intensity is increased, due to an improving SNR in each pixel. This trend is indeed observed Fig. 7.10, but only for some of the data, as indicated by solid curves. The opposite trend is also observed in Fig. 7.10, as indicated by dashed curves; since this trend is opposite to what is expected for random errors only, I attribute it to pixel locking. I term this particular effect of pixel locking the “pedestal effect.”

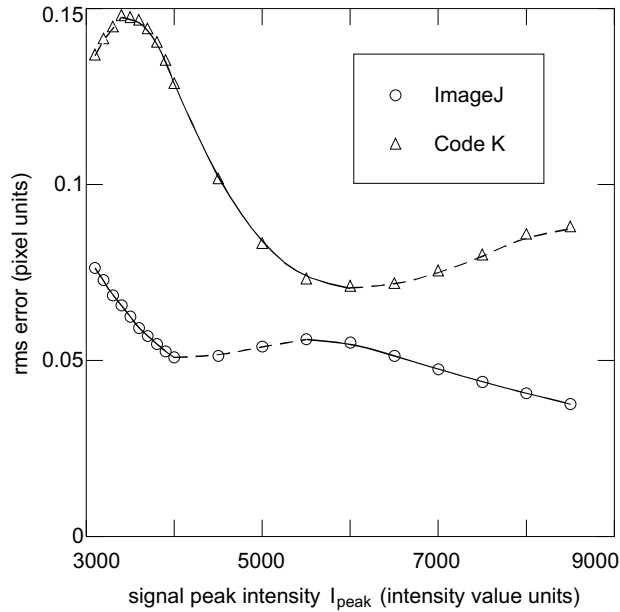


Figure 7.10: The rms error as the intensity is varied, to simulate adjusting the illumination brightness, the exposure time or the camera aperture. The main trend is that the error decreases with increasing intensity due to an improved signal-to-noise ratio (SNR), as indicated by solid curves; the opposite trend, indicated by dashed curves, is attributed to a pixel-locking effect that I term the pedestal effect. (Here,  $r_{spot} = 1.5$ ,  $I_{th} = 740$ , and  $I_{base} = 0$ .)

#### 7.5.4 Baseline

The pedestal effect is the result of a non-optimal choice of the baseline. To illustrate this effect, in Fig. 7.11 I have sketched the cross section of a bright spot. The portion of this cross section that lies within the boundary, defined by the threshold, is shown shaded. This portion is divided in Fig. 7.11 into two parts, above and below the threshold. I term the part below the threshold the “pedestal,” Fig. 7.11. The contribution of the pedestal to the moment in Eq. (7.2) can be large, or small, depending on whether  $I_{base}$  is small or large, respectively. In the extreme case of a very large pedestal that dominates the calculation of the particle position, the calculated particle position will often fall near a pixel edge or midpoint, as it does in the case of a centroid, thereby contributing to severe pixel locking. I

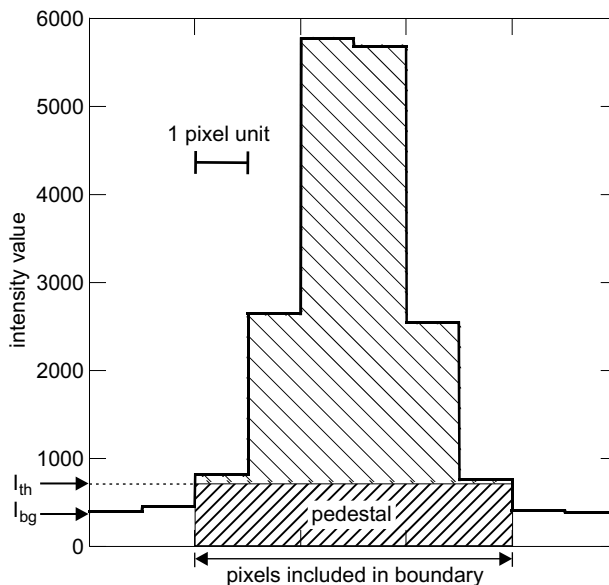


Figure 7.11: Cross section of a bright spot, illustrating the “pedestal.” Pixels brighter than the threshold identify the boundary for ImageJ in the first step. In the second step, both shaded portions contribute to the calculated particle position if  $I_{base} = 0$ , i.e., if no baseline is subtracted in Eq. (7.2). The lower shaded portion, marked “pedestal,” can heavily influence the calculated particle position. The pedestal can be reduced by choosing  $I_{base} = I_{bg}$ , or eliminated altogether by choosing  $I_{base} = I_{th}$ .

term this tendency toward severe pixel locking the “pedestal effect.” Below, I will determine the best choice of  $I_{base}$  in order to reduce the pedestal effect and the pixel-locking errors that it introduces to the calculated particle positions.

To test the effect of the baseline that is chosen, in Fig. 7.12 I present the total error, calculated as the rms error, for three different baseline values. From Fig. 7.12, I see that the total error is reduced by using a larger baseline value. The best choice is  $I_{base} = I_{th}$ , because this results in the smallest total error. It also minimizes pixel locking; the downward slope in Fig. 7.12 indicates that random errors dominate.

Thus, I conclude that in the second step, when using Eq. (7.2), the baseline should be chosen to be the same as the threshold that was used in the first step. This can be done most simply by subtracting the same threshold for every pixel

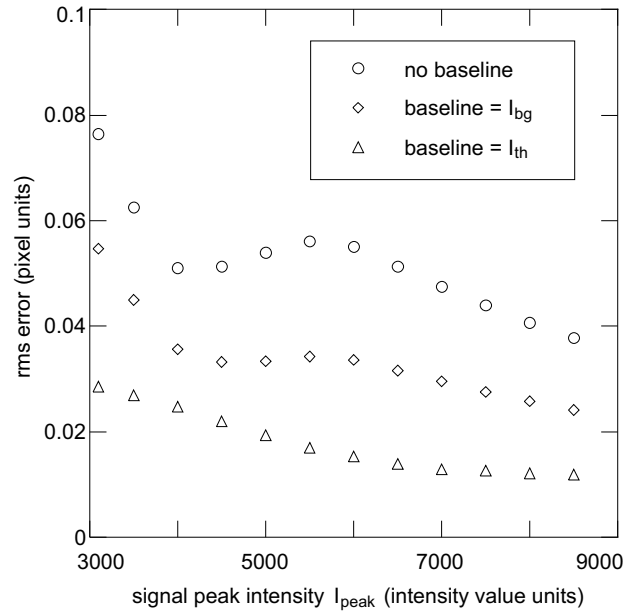


Figure 7.12: Test of different baselines. The best choice to minimize rms error is subtracting a baseline equal to the threshold  $I_{th}$  in Eq. (7.2). (I used ImageJ, and  $r_{spot} = 1.5$ ,  $I_{th} = 740$ , and  $I_{bg} = 384$ .)

in the image. Alternatively, a different baseline level  $I_{base\ k}$  for each pixel could be subtracted in Eq. (7.2), to account for a different background level for each pixel. The latter method is useful because it allows the experimenter to eliminate optical reflections due to room lights, for example. The experimenter can calculate all the  $I_{base\ k}$  baseline values for the pixels as follows. First, the experimenter will use the camera to record a “dark-field” image, with the illumination turned off so that particles are not visible. To improve the statistics, the experimenter can record a series of dark-field images and average them, pixel-by-pixel, to reduce the effect of random noise. This will yield an intensity  $I_{dark\ k}$  for each pixel. Second, the baseline for each pixel will be calculated as

$$I_{base\ k} = I_{dark\ k} + (I_{th} - I_{bg}). \quad (7.7)$$

Here,  $I_{bg}$  can be calculated as the average of  $I_{dark\ k}$  for pixels in the image.

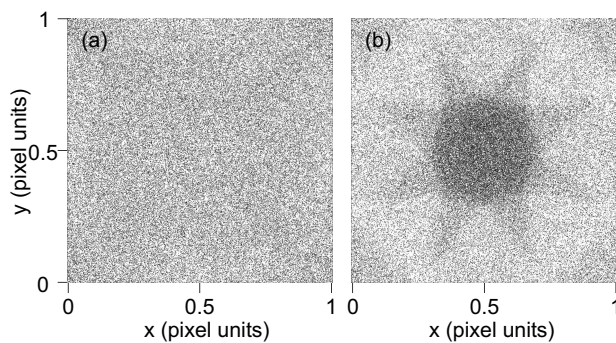


Figure 7.13: Sub-pixel maps, using a baseline  $I_{base} = I_{th}$  for two different thresholds (a)  $I_{th} = 1150$  and (b)  $I_{th} = 2950$ . Comparing these panels shows that the signature of pixel locking can be virtually eliminated, as in (a), by making the best choice of threshold as well as choosing  $I_{base} = I_{th}$ . (Here, I used the same 100 000 images as in Fig. 7.8.)

With an optimal choice of both threshold and baseline, one can achieve a sub-pixel map that shows no evidence of pixel locking, as seen in Fig. 7.13(a). This map was prepared using ImageJ, with a baseline equal to the threshold. This choice of a baseline minimizes the total error, as I learned above. The reason that choosing  $I_{base} = I_{th}$  minimizes the total error is now clear: it greatly reduces pixel locking, so that mainly errors from random noise remain. To further demonstrate the usefulness of choosing a baseline equal to the threshold, compare Fig. 7.8(a) to Fig. 7.13(a). The former figure, which was prepared similarly except with no baseline subtraction, reveals some pixel locking, while the latter does not.

An experimenter, when attempting to choose optimal parameters, will be unable to calculate the rms error, as I have done in Fig. 7.12, for example. This is because the true positions of particles are generally unknown. The experimenter can, however, calculate sub-pixel maps, such as Fig. 7.13, because these require only calculated positions. Comparing Fig. 7.13(a) and 7.13(b), which were both calculated with  $I_{base} = I_{th}$ , but with a different  $I_{th}$ , I see that the signature of pixel locking depends on the threshold.

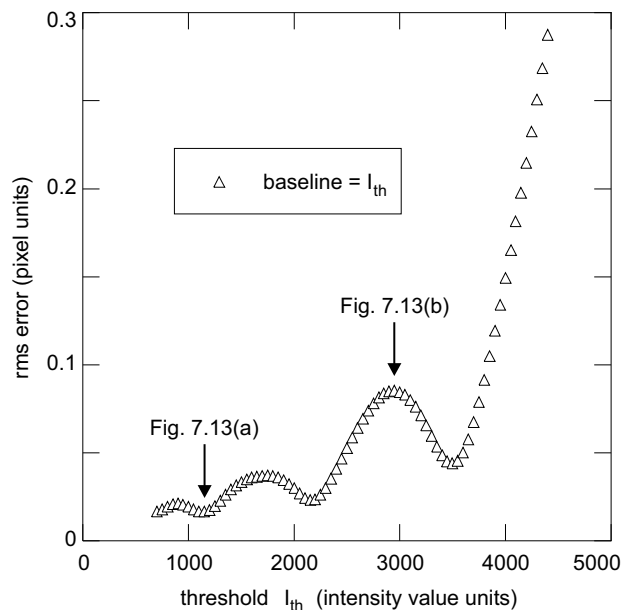


Figure 7.14: Total error, using a baseline  $I_{base} = I_{th}$ . Comparing to Fig. 7.6 where  $I_{base} = 0$ , errors have been reduced. The lowest rms error that can be achieved with these images is 0.017, using the same optimal choice of parameters as in Fig. 7.13(a). (I used the same 5000 images as in Fig. 7.6. Here and in Fig. 7.13, I used ImageJ.)

I now find my best result by varying the threshold, in Fig. 7.14, to minimize the rms error. The threshold is the last parameter to choose, assuming that the experimenter has already: (1) established the illumination level, (2) chosen a camera with a given noise level, (3) defocused the camera lens to avoid saturating pixels, and (4) planned to use a baseline  $I_{base} = I_{th}$ . Noting that the rms error in Fig. 7.14 has several minima, I identify an optimal threshold by choosing the lowest minimum. This yields my best result, an rms error of 0.017. These same parameters also virtually eliminate the signature of pixel locking in Fig. 7.13(a). An experimenter can identify an optimal  $I_{th}$  similarly, but without calculating the rms error, by examining sub-pixel maps for various values of  $I_{th}$ , and among the maps with weak pixel-locking signatures, choosing the one with the lowest value of  $I_{th}$ .

## 7.6 Practical procedure

I present here a practical procedure for using the moment method that minimizes the total error, including both random errors and pixel locking. This practical procedure includes first the use of hardware to record images and then the use of software to analyze them. My software uses the moment method with baseline subtraction as I tested above; there are also other well-tested analysis methods that experimenters may wish to consider [129, 130].

For the hardware that produces the image, one will choose a camera and make adjustments to the intensity and lens focusing. Choosing a camera with low noise will not only reduce random errors; it will also allow the use of a lower threshold which can improve pixel locking. In using the camera, the optimal choices of intensity and lens defocusing must be considered together. The intensity can be varied, for example, by adjusting the camera aperture, exposure time, or illumination level. To achieve a high SNR in each pixel, I adjust the intensity upward as high as possible without saturating pixels. Another way to improve SNR is pixel binning, which also increase frame rate, but at the expense of spatial resolution [151]. If additional intensity is available but pixels are saturated, the experimenter can defocus the lens to avoid saturating the brightest pixels. Defocusing the lens helps reduce pixel locking, but it can increase random errors by reducing the SNR in each pixel; therefore, defocusing beyond a certain point actually worsens the total error. The optimal lens defocusing will depend on parameters such as intensity, camera noise level, and number of camera bits, which vary from one experiment to another. For the parameters I simulated (see Fig. 7.9) I found that the optimal spot radius was in the range 0.8 - 2.0, measured as the Gaussian half-width. For other parameters, I can offer this general guidance: the optimal lens defocusing will be determined by the need to achieve an adequate SNR in each pixel. Noisier cameras or weaker

illumination will require less defocusing, while low-noise cameras and brighter illumination will allow more defocusing. The lens should generally be defocused at least enough to avoid saturating pixels.

For the image analysis software, there are usually three important choices. First, I prefer a code that has as its first step the selection of a boundary that includes only contiguous pixels above a threshold. The freely available ImageJ code selects such a boundary. Second, if the boundary is selected as described above in the first step, then in the second step, using Eq. (7.2), the baseline should be chosen equal to the threshold, in order to reduce pixel locking. This can be done either by subtracting the same baseline value from every pixel in a single step, or by using Eq. (7.7) with dark-field images if the experimenter wishes to remove the effect of optical reflections for example. Third, the threshold should be chosen in a two-part process. To start, the experimenter should count the number of particles that are identified, and then choose a coarse range as explained in Sec. 7.5.1. Next, within this coarse range, sub-pixel maps should be calculated for various thresholds. In order to reduce both random and pixel-locking errors, the user should choose the lowest threshold that has a weak signature of pixel locking.

The moment method can achieve very low errors in particle position measurement when it is used optimally. For the case I simulated, an rms error as small as 0.017 is achievable by making optimal choices in the software. Even smaller errors could be attained if the intensity were brighter or the camera had less noise.

## 7.7 Experimental demonstration

To demonstrate the practical procedure above, I used it in an experiment. The results presented above, based on synthetic images, indicate that both total errors and pixel locking will be reduced if I follow the practical procedure. Using experimental images, one can detect the signature of pixel locking using sub-pixel

maps. I describe next the hardware and software components of my experimental test.

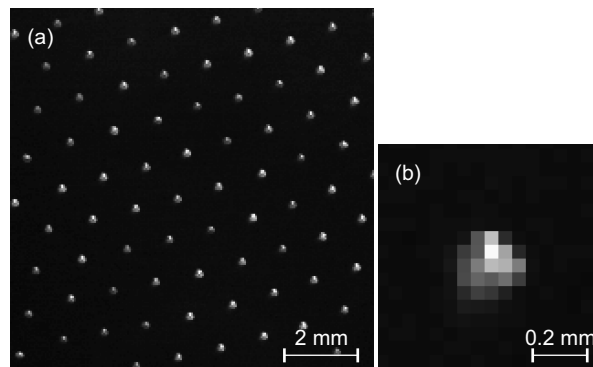


Figure 7.15: Experimental bit-map images of a monolayer suspension of microspheres in a dusty plasma. Here, (a) is 1/12 of the original image and (b) is a magnified view. A bright spot fills about  $5 \times 5$  pixels. Compared to Fig. 7.1(a), the hardware was improved by slight lens defocusing.

For the hardware, the experiment was similar to the one for Fig. 7.1(a), including using the same 14-bit camera, except that I improved the experimental method by slightly defocusing the lens. A cropped portion of the  $800 \times 600$  pixels image Fig. 7.15(a) and a magnified view Fig. 7.15(b) show that a bright spot fills more pixels than in Fig. 7.1(b) where the lens was sharply focused. Due to defocusing, the spots are slightly noncircular. Additionally, I binned  $2 \times 2$  pixels. As a result of these changes, the total intensity of a bright spot is typically 39 240, as compared to 21 000 (with a maximum of 37 707) for Fig. 7.1(a), and the noise peak is shifted to a lower intensity. A further possible improvement in the hardware is using a more powerful laser, and I plan to do that in future experiments.

For the software, I used ImageJ to identify particles from 100 experimental images. I excluded any identified particles that filled only one single pixel. First, I chose a coarse range for the threshold by counting the number of identified particles

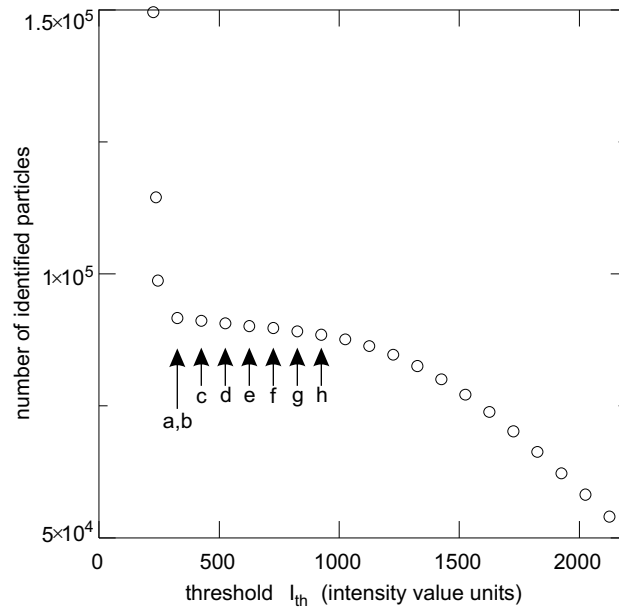


Figure 7.16: Choosing the coarse range of threshold using experimental images. Counting the particles identified in 100 images, I choose the nearly flat portion  $325 \leq I_{th} \leq 925$  as the coarse range. Outside this coarse range, many false particles appear at lower  $I_{th}$  due to noise, while many true particles are missed at higher  $I_{th}$ . Labels a-h identify thresholds used in Fig. 7.17.

as a function of the threshold, Fig. 7.16. I looked for a nearly flat portion, which is from 325 to 925 here, and I chose that as the coarse range. Next, I calculated particle positions using Eq. (7.2), along with Eq. (7.7) to calculate  $I_{base\ k}$  using an average of 2000 dark-field images. I repeated these calculations of particle positions for various thresholds, each time preparing a sub-pixel map. Finally, I will examine these sub-pixel maps to choose the lowest threshold that has a weak signature of pixel locking.

In Fig. 7.17, I present the sub-pixel map that results from following my practical procedure in panel (a). Examining this sub-pixel map, I see that it has no obvious signature of pixel locking when viewed in its entirety. To search for signatures, I zoom into the lower left corner, Fig. 7.17(b)-(h). There, I can identify an artifact of pixel locking: a concentration of calculated positions on pixel edges. My

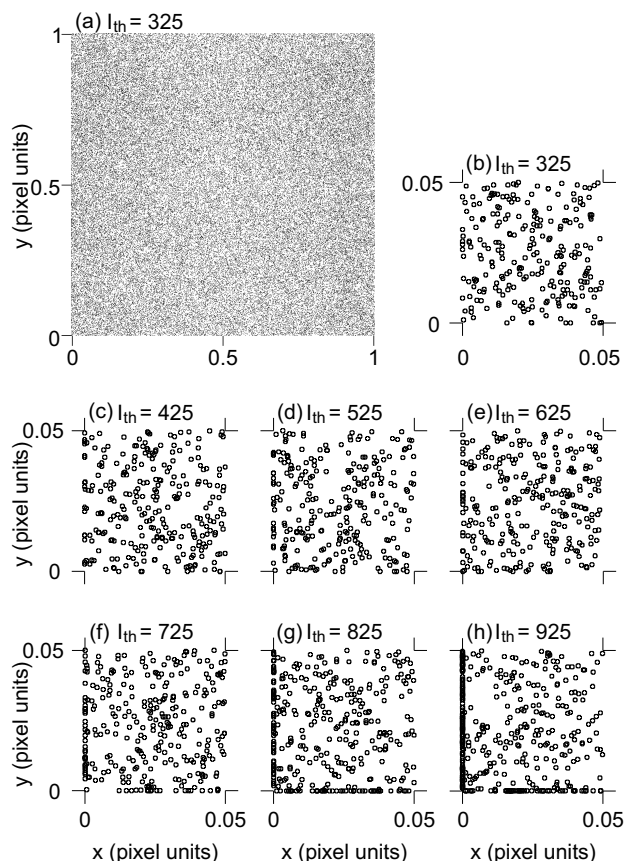


Figure 7.17: Experimental sub-pixel maps for different thresholds within the coarse range. Here, (a) is an entire map, and (b)-(h) show the lower left corner. I choose the lowest  $I_{th}$  with a weak signature of pixel locking, 325. The signature is stronger for  $I_{th} \geq 525$ , with a concentration of calculated positions on pixel edges. Vastly better than Fig. 7.3(c), there is no obvious signature of pixel locking for  $I_{th} < 525$ . (Here, I used ImageJ with  $I_{base\ k}$  calculated from Eq. (7.7) and a dark-field image.)

practical procedure requires choosing the lowest threshold with a weak signature of pixel locking. For my results in Fig. 7.17, thresholds in the range 325 - 425 have no identifiable signature, leading us to choose 325.

I conclude that the signature of pixel locking is vastly improved by using my practical procedure. This conclusion is based on a comparison of the sub-pixel maps in Fig. 7.17(a) and Fig. 7.3(c). The latter was prepared for a similar experiment

but a different camera, illumination, and analysis method. The signature of pixel locking is profound in Fig. 7.3(c), but it is virtually undetectable in Fig. 7.17(a)-(c).

## CHAPTER 8 CONCLUSION

In this thesis I presented three experiments with dusty plasmas (Chapters 3-5) and one simulation (Chapter 6) to study microscopic dynamics of strongly-coupled plasmas. In the experiments, I used direct imaging by video microscopy, and laser manipulation, to study dynamics at the level of discrete particles. Additionally, I reported an improved image analysis method (Chapter 7) for the accurate measurement of particle positions in experiments.

The experiment with suddenly-applied heating (Chapter 3) demonstrated the phenomenon of solid superheating in a strongly-coupled plasma for the first time. This result suggests that future investigations could be carried out to search for solid superheating in other strongly-coupled plasmas, like laser-cooled ions [10] and the crust of neutron stars [8]. This also serves as the first experimental demonstration that solid superheating can be studied experimentally at the level of discrete particles. Additionally, I found a lack of liquid supercooling behavior in my 2D strongly-coupled dusty plasma.

The experiment with suddenly-applied shear (Chapter 4) is the first study of the spatial and temporal development of shear-induced melting. I discovered that coherent longitudinal waves were excited in the shear flow. Applying shear suddenly led to melting in two stages separated by a distinctive transition. After defects saturated within narrow flow regions, they spread wider with a melting front that propagated at about the transverse sound speed.

The experiment with steady-state heating (Chapter 5) yielded the first laboratory quantification of viscoelasticity of a strongly-coupled plasma. I found that  $\eta(k)$  diminished with increasing  $k$ , indicating that viscous behavior is gradually replaced by elastic behavior as the scale length is reduced. This diminishment can

be modeled as  $\propto (1 + \alpha k^2)^{-1}$ . These results required that I generalized a method of calculating  $\eta(k)$  by including the friction in the Navier-Stokes equation. To confirm the interpretation of the experimental results, I also performed a simulation of particle motion and used the same analysis method.

The simulations (Chapter 6) demonstrated that the self-intermediate scattering function (self-ISF), which is widely used in other physical fields, is also used for strongly-coupled plasmas. The self-ISF is a dynamical measure of random motion. It allows a characterization of relaxation of random motion. For my particle simulation, I found that the relaxation of a 2D liquid-state dusty plasma is a stretched exponential. A scaling of the relaxation time with the length scale was found, and this scaling was shown to be useful for distinguishing normal and anomalous diffusion. Friction was found to have little effect on relaxation except for high levels of frictional dissipation, where the effect was a retardation of relaxation. While previous investigators identified the solid-liquid melting transition using measures of structure, I demonstrate that the self-ISF, which is a dynamical measure, is also a sensitive indicator.

An improved image analysis method (Chapter 7) was developed. I made a systematic study of the moment method of measuring particle positions by using synthetic images to gain an understanding of error sources: pixel-locking error and random error. This study led me to recommend a practical procedure that I verified to reduce errors as much as possible.

**APPENDIX A**  
**DERIVATION OF WAVENUMBER-DEPENDENT VISOCOSITY**  
 $\eta(K)$

Here I present a derivation of Eq. 5.2 in Chapter 5. This derivation is a generalization Hu's derivation, Eq. (7) in [62]. My generalization takes into account a second phase. In general, a two-phase liquid has two substances which have separate equations of motion, and these two equations of motion are coupled together. Here I focus primarily on one phase (which in my experiment consists of charged microspheres) and I include in its equation of motion a frictional term that represents coupling to the other phase (which is a rarefied gas in my experiment).

The equation of motion for a single phase is the Navier-Stokes equation, Eq. (2.5.18) of [152],

$$\frac{\partial}{\partial t} \mathbf{j}(\mathbf{r}, t) + \frac{1}{\rho} \nabla p(\mathbf{r}, t) - \frac{\eta}{\rho} \nabla^2 \mathbf{j}(\mathbf{r}, t) - \frac{1}{\rho} (\eta_B + \frac{1}{3} \eta) \nabla \nabla \cdot \mathbf{j}(\mathbf{r}, t) = 0. \quad (\text{A.1})$$

I only consider the transverse current, which satisfies

$$\nabla \cdot \mathbf{j}(\mathbf{r}, t) = 0. \quad (\text{A.2})$$

As shown in Eq. (2.5.22) of [152], Eq. A.1 above will be reduced to

$$\frac{\partial}{\partial t} \mathbf{j}(\mathbf{r}, t) - \frac{\eta}{\rho} \nabla^2 \mathbf{j}(\mathbf{r}, t) = 0. \quad (\text{A.3})$$

The coupling to the second phase (which is gas friction, in my experiment), is modeled by adding a friction term to Eq. A.3 above, so that it becomes

$$\frac{\partial}{\partial t} \mathbf{j}(\mathbf{r}, t) - \frac{\eta}{\rho} \nabla^2 \mathbf{j}(\mathbf{r}, t) + \nu_f \mathbf{j}(\mathbf{r}, t) = 0. \quad (\text{A.4})$$

Fourier transformation yields a corresponding equation in  $\mathbf{k}$  space:

$$\frac{\partial}{\partial t} \tilde{\mathbf{j}}(\mathbf{k}, t) + \frac{\eta}{\rho} k^2 \tilde{\mathbf{j}}(\mathbf{k}, t) + \nu_f \tilde{\mathbf{j}}(\mathbf{k}, t) = 0. \quad (\text{A.5})$$

The general solution for Eq. A.5 is

$$\tilde{\mathbf{j}}(\mathbf{k}, t) = \tilde{\mathbf{j}}(\mathbf{k}, 0) \exp\left[-\left(\frac{\eta}{\rho} k^2 + \nu_f\right)t\right]. \quad (\text{A.6})$$

Using this to find the transverse current autocorrelation function (TCAF) yields

$$C_T(\mathbf{k}, t) = C_T(\mathbf{k}, 0) \exp\left[-\left(\frac{\eta}{\rho} k^2 + \nu_f\right)t\right]. \quad (\text{A.7})$$

Following the procedure of [62], the Fourier transformation of TCAF is

$$C_T(\mathbf{k}, \omega) = \int_0^{+\infty} C_T(\mathbf{k}, t) \exp(-i\omega t) dt. \quad (\text{A.8})$$

Then, the area under the normalized TCAF is

$$\Phi = \frac{C_T(\mathbf{k}, \omega = 0)}{C_T(\mathbf{k}, t = 0)} = \int_0^{+\infty} \exp\left[-\left(\frac{\eta}{\rho} k^2 + \nu_f\right)t\right] dt = \left(\frac{\eta}{\rho} k^2 + \nu_f\right)^{-1}. \quad (\text{A.9})$$

Finally, the wavenumber-dependent viscosity  $\eta(k)$  can be calculated from

$$\frac{\eta(k)}{\rho} = \left(\frac{1}{\Phi} - \nu_f\right)/k^2. \quad (\text{A.10})$$

This result is Eq. 5.2 in Chapter 5.

## APPENDIX B ERRORS IN OTHER QUANTITIES

Errors in the calculated particle positions can introduce errors in other quantities that are calculated from the positions. In PTV, velocities are calculated as  $v = (x_2 - x_1)/\Delta t$ , as discussed in Sec. 7.1. Pixel locking can affect the velocity calculation greatly in experiments. For example, if pixel locking is so severe that most calculated positions are located only at pixel centers, then almost all particle velocities calculated in PTV will be quantized as an integer number of pixel widths per frame. These errors in calculating velocities can propagate to other calculations. Velocity distribution functions  $f(v)$  can be badly affected, with noticeable peaks [82] that are signatures of pixel locking. However, I have found that wave spectra and velocity correlation functions are not affected so badly.

While it is beyond the scope of this thesis to completely characterize the errors in  $v$  or  $f(v)$ , I can discuss the contributions to the total error in  $v$ . For PTV, the rms error,  $\delta v = \overline{((\delta x_1^2 + \delta x_2^2 - 2\delta x_1\delta x_2)/\Delta t^2)}^{\frac{1}{2}}$ , has two contributions,  $\overline{(\delta x_1^2 + \delta x_2^2)}/\Delta t^2$  arising from the errors in position, and  $(-2\overline{\delta x_1\delta x_2})/\Delta t^2$  arising from correlations in the two errors. If the calculated position had random errors only, the correlation  $\overline{\delta x_1\delta x_2}$  would be zero and the rms error in  $v$  would be minimized when the rms error in  $x$  is minimized. However, pixel-locking errors can have correlations, which will vary depending on the velocities, and these will affect  $\delta v$  in a way that is difficult to predict.

Aside from these quantities, which are calculated from velocities, experimenters often calculate other quantities from the position itself. The mean-square displacement (MSD), which is used to measure diffusion, is calculated from position. Particle position errors can cause the MSD to be exaggerated significantly at small times when the displacement is small, but not at large times when the displacement

is large [132]. Another use of particle positions is the study of structure [74, 153]. While I have not analyzed the sensitivity of structural analysis methods to particle position errors, I expect that calculations that are sensitive to small changes in interparticle distances, such as Voronoi maps for detecting defects, will be more affected than correlation functions that use data over a wide range of distances.

## REFERENCES

- [1] F. F. Chen, *Plasma Physics and Controlled Fusion*, 2nd ed. (Springer, New York, 2006).
- [2] R. L. Merlino and J. A. Goree, *Phys. Today* **57**(7), 32 (2004).
- [3] H. Thomas, G. E. Morfill, V. Demmel, J. Goree, B. Feuerbacher, and D. Möhlmann, *Phys. Rev. Lett.* **73**, 652 (1994).
- [4] J. H. Chu and L. I, *Phys. Rev. Lett.* **72**, 4009 (1994).
- [5] Y. Hayashi and K. Tachibana, *Jpn. J. Appl. Phys.* **33**, L804 (1994).
- [6] H. Ikezi, *Phys. Fluids* **29**, 1764 (1986).
- [7] S. Ichimaru, *Rev. Mod. Phys.* **54**, 1017 (1982).
- [8] C. J. Horowitz, D. K. Berry, and E. F. Brown, *Phys. Rev. E* **75**, 066101 (2007).
- [9] M. S. Murillo, *Phys. Plasmas* **11**, 2964 (2004).
- [10] M. J. Jensen *et al.*, *Phys. Rev. Lett.* **94**, 025001 (2005).
- [11] G. E. Morfill and A. V. Ivlev, *Rev. Mod. Phys.* **81**, 1353 (2009).
- [12] P. Gould and E. Eyler, *Phys. World* **14**, 19 (2001).
- [13] U. Konopka, G. E. Morfill, and L. Ratke, *Phys. Rev. Lett.* **84**, 891 (2000).
- [14] B. Liu, J. Goree, V. Nosenko, and L. Boufendi, *Phys. Plasmas* **10**, 9 (2003).
- [15] C. C. Grimes and G. Adams, *Phys. Rev. Lett.* **42**, 795 (1979).
- [16] P. L. Gammel *et al.*, *Phys. Rev. Lett.* **59**, 2592 (1987).
- [17] H. König *et al.*, *Eur. Phys. J. E* **18**, 287 (2005).
- [18] P. M. Reis, R. A. Ingale, and M. D. Shattuck, *Phys. Rev. Lett.* **96**, 258001 (2006).

- [19] H. M. Thomas and G. E. Morfill, *Nature (London)* **379**, 806 (1996).
- [20] A. Melzer, A. Homann, and A. Piel, *Phys. Rev. E* **53**, 2757 (1996).
- [21] U. Konopka, D. Samsonov, A. V. Ivlev, J. Goree, V. Steinberg, and G. E. Morfill, *Phys. Rev. E* **61**, 1890 (2000).
- [22] D. Samsonov *et al.*, *Phys. Rev. Lett.* **92**, 255004 (2004).
- [23] C. A. Knapek *et al.*, *Phys. Rev. Lett.* **98**, 015004 (2007).
- [24] O. Arp, D. Block, A. Piel, and A. Melzer, *Phys. Rev. Lett.* **93**, 165004 (2004).
- [25] A. Melzer, S. Nunomura, D. Samsonov, Z. W. Ma, and J. Goree, *Phys. Rev. E* **62**, 4162 (2000).
- [26] S. Nunomura, D. Samsonov, and J. Goree, *Phys. Rev. Lett.* **84**, 5141 (2000).
- [27] S. Nunomura *et al.*, *Phys. Rev. Lett.* **89**, 035001 (2002).
- [28] W. T. Juan and L. I, *Phys. Rev. Lett.* **80**, 3037 (1998).
- [29] V. E. Fortov *et al.*, *Phys. Rev. E* **75**, 026403 (2007).
- [30] V. Nosenko *et al.*, *Phys. Rev. Lett.* **100**, 025003 (2008).
- [31] B. Liu and J. Goree, *Phys. Rev. Lett.* **100**, 055003 (2008).
- [32] R. A. Quinn and J. Goree, *Phys. Rev. E* **64**, 051404 (2001).
- [33] X. M. Bai and M. Li, *J. Chem. Phys.* **123**, 151102 (2005).
- [34] J. G. Dash, *Rev. Mod. Phys.* **71**, 1737 (1999).
- [35] J. W. Herman and H. E. Elsayed-Ali, *Phys. Rev. Lett.* **69**, 1228 (1992).
- [36] H. Iglev *et al.*, *Nature* **439**, 183 (2006).
- [37] L. Gråbæk *et al.*, *Phys. Rev. B* **45**, 2628 (1992).
- [38] L. Zhang *et al.*, *Phys. Rev. Lett.* **85**, 1484 (2000).
- [39] M. Rubin-Zuzic *et al.*, *Nature Phys.* **2**, 181 (2006).

- [40] B. J. Ackerson and N. A. Clark, Phys. Rev. Lett. **46**, 123 (1981).
- [41] S. Ramaswamy and S. R. Renn, Phys. Rev. Lett. **56**, 945 (1986).
- [42] T. Weider, M. A. Glaser, H. J. M. Hanley, and N. A. Clark, Phys. Rev. B **47**, 5622 (1993).
- [43] S. Butler and P. Harrowell, Nature **415**, 1008 (2002).
- [44] J. Delhommelle, Phys. Rev. B **69**, 144117 (2004).
- [45] R. Messina and H. Löwen, Phys. Rev. E **73**, 011405 (2006).
- [46] C. Eisenmann, C. Kim, J. Mattsson and D. A. Weitz, Phys. Rev. Lett. **104**, 035502 (2010).
- [47] L. Wilen and R. Giannetta, Japanese J. Appl. Phys. Supplement **26-3**, 2105 (1987).
- [48] A. D. Gopal and D. J. Durian, J. Colloid Interface Sci. **213**, 169 (1999).
- [49] D. A. Weitz, Science **323**, 214 (2009).
- [50] V. Nosenko and J. Goree, Phys. Rev. Lett. **93**, 155004 (2004).
- [51] R. Lakes, *Viscoelastic Materials*, 1st ed. (Cambridge University Press, Cambridge, 2009).
- [52] V. Nosenko, J. Goree, and A. Piel, Phys. Rev. Lett. **97**, 115001 (2006).
- [53] P. K. Kaw and A. Sen, Phys. Plasmas **5**, 3552 (1998).
- [54] M. S. Murillo, Phys. Plasmas **7**, 33 (2000).
- [55] S. Ratynskaia *et al.*, Phys. Rev. Lett. **96**, 105010 (2006).
- [56] C. L. Chan and L. I, Phys. Rev. Lett. **98**, 105002 (2007).
- [57] T. G. Mason and D. A. Weitz, Phys. Rev. Lett. **75**, 2770 (1995);
- [58] W. E. Alley and B. Alder, Phys. Rev. A **27**, 3158 (1983).
- [59] U. Balucani, R. Vallauri, and T. Gaskell, Phys. Rev. A **35**, 4263 (1987).

- [60] B. J. Palmer, Phys. Rev. E **49**, 359 (1994).
- [61] U. Balucani, J. P. Brodholt, P. Jedlovszky, and R. Vallauri, Phys. Rev. E **62**, 2971 (2000).
- [62] Z. Hu and C. J. Margulis, J. Phys. Chem. B **111**, 4705 (2007).
- [63] P. N. Pusey, in *Liquids, Freezing and The Glass Transition*, edited by J. P. Hansen, D. Levesque, and J. Zinn-Justin (Elsevier, Amsterdam, 1991), Chap. 10.
- [64] O. Dauchot, G. Marty, and G. Biroli, Phys. Rev. Lett. **95**, 265701 (2005).
- [65] P. M. Reis, R. A. Ingale, and M. D. Shattuck, Phys. Rev. Lett. **98**, 188301 (2007).
- [66] A. Meyer, Phys. Rev. B **81**, 012102 (2010).
- [67] W. Kob and J.-L. Barrat, Phys. Rev. Lett. **78**, 4581 (1997).
- [68] T. Abete *et al.*, Phys. Rev. Lett. **98**, 088301 (2007).
- [69] P.J. Hargis, Jr. *et al.*, Rev. Sci. Instrum. **65**, 140 (1994).
- [70] J.B. Pieper, J. Goree, and R.A. Quinn, J. Vac. Sci. Technol. A **14**(2), 519 (1996).
- [71] D.R. Nicholson, *Introduction to Plasma Theory* (John Wiley & Sons, New York, 1983).
- [72] I. V. Schweigert, V. A. Schweigert, and F. M. Peeters, Phys. Rev. Lett. **82**, 5293 (1999).
- [73] P. Hartmann *et al.*, Phys. Rev. E **72**, 026409 (2005).
- [74] R. A. Quinn, C. Cui, J. Goree, J. B. Pieper, H. Thomas, and G. E. Morfill, Phys. Rev. E **53**, R2049 (1996).
- [75] G. J. Kalman, P. Hartmann, Z. Donkó, and M. Rosenberg, Phys. Rev. Lett. **92**, 065001 (2004).
- [76] B. Liu *et al.*, Phys. Plasmas **16**, 083703 (2009).
- [77] J. P. Hansen and I. R. McDonald, *The Theory of Simple Liquids*, 2nd ed. (Elsevier Academic Press, Amsterdam, 1986).

- [78] R. S. Smith and B. D. Kay, *Nature* **398**, 788 (1999).
- [79] M. D. Ediger, C. A. Angell, and S. R. Nagel, *J. Phys. Chem.* **100**, 13200 (1996).
- [80] Z. L. Xiao *et al.*, *Phys. Rev. Lett.* **92**, 227004 (2004).
- [81] E. R. Weeks *et al.*, *Science* **287**, 627 (2000).
- [82] V. Nosenko, J. Goree, and A. Piel, *Phys. Plasmas* **13**, 032106 (2006).
- [83] C. J. Olson *et al.*, *Phys. Rev. B* **67**, 184523 (2003).
- [84] M. Bayer *et al.*, *Phys. Rev. E* **76**, 011508 (2007).
- [85] R. W. Cahn, *Nature* **323**, 668 (1986).
- [86] Y. Feng, J. Goree and B. Liu, *Phys. Rev. Lett.* **100**, 205007 (2008).
- [87] Y. Feng, B. Liu, and J. Goree, *Phys. Rev. E* **78**, 026415 (2008).
- [88] T. B. Mitchell *et al.*, *Phys. Plasmas* **6**, 1751 (1999).
- [89] C. A. Murray, W. O. Sprenger, and R. A. Wenk, *Phys. Rev. B* **42**, 688 (1990).
- [90] C. Reichhardt and C. J. O. Reichhardt, *Phys. Rev. E* **77**, 041401 (2008).
- [91] W.-Y. Woon and L. I, *Phys. Rev. Lett.* **92**, 065003 (2004).
- [92] T. E. Sheridan, *Phys. Plasmas* **15**, 103702 (2008).
- [93] A. V. Ivlev, U. Konopka, G. Morfill, and G. Joyce, *Phys. Rev. E* **68**, 026405 (2003).
- [94] S. Nunomura, S. Zhdanov, D. Samsonov, and G. Morfill, *Phys. Rev. Lett.* **94**, 045001 (2005).
- [95] L.-J. Hou and A. Piel, *J. Phys. A: Math. Theor.* **42**, 214025 (2009).
- [96] Z. Donkó, J. Goree, and P. Hartmann, *Phys. Rev. E* **81**, 056404 (2010).
- [97] Z. Donkó, P. Hartmann, G. J. Kalman, *Phys. Rev. E* **69**, 065401(R) (2004).
- [98] B. Liu and J. Goree, *Phys. Rev. Lett.* **94**, 185002 (2005).

- [99] Z. Donkó, J. Goree, P. Hartmann, and K. Kutasi, *Phys. Rev. Lett.* **96**, 145003 (2006).
- [100] R. F. Berg, M. R. Moldover, and G. A. Zimmerli, *Phys. Rev. E* **60**, 4079 (1999).
- [101] O. S. Vaulina *et al.*, *Phys. Lett. A* **372**, 1096 (2008).
- [102] M. Wolter and A. Melzer, *Phys. Rev. E* **71**, 036414 (2005).
- [103] Y. Feng, J. Goree, and B. Liu, *Rev. Sci. Instrum.* **78**, 053704 (2007).
- [104] L. J. Hou, A. Piel, and P. K. Shukla, *Phys. Rev. Lett.* **102**, 085002 (2009).
- [105] O. S. Vaulina *et al.*, *Phys. Rev. Lett.* **103**, 035003 (2009).
- [106] T. Ott and M. Bonitz, *Phys. Rev. Lett.* **103**, 195001 (2009).
- [107] D. Samsonov *et al.*, *Phys. Rev. Lett.* **83**, 3649 (1999).
- [108] C.-W. Io and L. I, *Phys. Rev. E* **80**, 036401 (2009).
- [109] B. Liu, J. Goree, and Y. Feng, *Phys. Rev. E* **78**, 046403 (2008).
- [110] B. Liu and J. Goree, *Phys. Rev. E* **75**, 016405 (2007).
- [111] Z. Donkó, J. Goree, P. Hartmann, and B. Liu, *Phys. Rev. E* **79**, 026401 (2009).
- [112] W. van Megen and P. N. Pusey, *Phys. Rev. A* **43**, 5429 (1991).
- [113] M. C. Bellissent-Funel, S. Longeville, J. M. Zanotti, and S. H. Chen, *Phys. Rev. Lett.* **85**, 3644 (2000).
- [114] S. Srivastava *et al.*, *Phys. Rev. E* **79**, 021408 (2009).
- [115] X. Lu *et al.*, *Phys. Rev. Lett.* **100**, 045701 (2008).
- [116] S. Kambayashi and Y. Hiwatari, *J. Phys. Soc. Jpn.* **56**, 2788 (1987).
- [117] W. van Megen, T. C. Mortensen, S. R. Williams, and J. Müller, *Phys. Rev. E* **58**, 6073 (1998).
- [118] H. Ohta and S. Hamaguchi, *Phys. Plasmas* **7**, 4506 (2000).

- [119] K. Y. Sanbonmatsu and M. S. Murillo, *Phys. Rev. Lett.* **86**, 1215 (2001).
- [120] H. Löwen, *J. Phys. Condens. Matter* **4**, 10105 (1992).
- [121] R. K. Pathria, *Statistical Mechanics* (Pergamon Press, Oxford, 1972).
- [122] W. F. van Gunsteren and H. J. C. Berendsen, *Mol. Phys.* **45**, 637 (1982).
- [123] D. R. Reichman and P. Charbonneau, *J. Stat. Mech.: Theory Exp.* (2005), P05013.
- [124] B. R. A. Nijboer and A. Rahman, *Physica (Amsterdam)* **32**, 415 (1966).
- [125] R. Kurita and E. R. Weeks, arXiv:0910.2628 (2009).
- [126] T. Kawasaki, T. Araki, and H. Tanaka, *Phys. Rev. Lett.* **99**, 215701 (2007).
- [127] D. Samsonov, J. Goree, H. M. Thomas, and G. E. Morfill, *Phys. Rev. E* **61**, 5557 (2000).
- [128] Y. Ivanov and A. Melzer, *Rev. Sci. Instrum.* **78**, 033506 (2007).
- [129] J. C. Crocker and D. G. Grier, *J. Colloid Interf. Sci.* **179**, 298 (1996).
- [130] M. Kvarnström and C. A. Glasbey, *Biometrical J.* **49**, 300 (2007).
- [131] K. -A. Chang and P. L. -F. Liu, *Phys. Fluids* **10**, 327 (1998).
- [132] C. Selle, F. Ruckerl, D. S. Martin, M. B. Forstner, and J. A. Käs, *Phys. Chem. Chem. Phys.* **6**, 5535 (2004).
- [133] M. Shimizu and M. Okutomi, *Int. J. Comput. Vision* **63**, 207 (2005).
- [134] F. A. Jenkins and H. E. White, *Fundamentals of Optics*, 3rd ed. (Mcgraw-Hill, New York, 1957), p. 302.
- [135] F. Melandsø, Å. Bjerkmo, G. Morfill, H. Thomas, and M. Zuzic, *Phys. Plasmas* **7**, 4368 (2000).
- [136] W. S. Rasband, computer code ImageJ version 1.34, U. S. National Institutes of Health, Bethesda, Maryland, 2006 (<http://rsb.info.nih.gov/ij/>). The “center of mass” is displaced 1/2 pixel in both directions, as compared to our definition.

- [137] M. Gai, D. Carollo, M. Delbò, M. G. Lattanzi, G. Massone, F. Bertinetto, G. Mana, and S. Cesare, *Astron. Astrophys.* **367**, 362 (2001).
- [138] J. Westerweel, *Meas. Sci. Technol.* **8**, 1379 (1997).
- [139] C. E. Willert and M. Gharib, *Exp. Fluids* **10**, 181 (1991).
- [140] A. K. Prasad, R. J. Adrian, C. C. Landreth, and P. W. Offutt, *Exp. Fluids* **13**, 105 (1992).
- [141] L. Gui and S. T. Wereley, *Exp. Fluids* **32**, 506 (2002).
- [142] K. T. Christensen, *Exp. Fluids* **36**, 484 (2004).
- [143] K. P. Angele and B. Muhammad-Klingmann, *Exp. Fluids* **38**, 341 (2005).
- [144] H. Nobach and M. Honkanen, *Exp. Fluids* **38**, 511 (2005).
- [145] S. Käding and A. Melzer, *Phys. Plasmas* **13**, 090701 (2006).
- [146] A. Stein, A. Huertas, and L. Matthies, *IEEE International Conference on Robotics and Automation* (IEEE, New York, 2006), p. 914.
- [147] D. Nehab, S. Rusinkiewicz, and J. Davis, *Tenth IEEE International Conference on Computer Vision* (IEEE, New York, 2005), p. 557.
- [148] O. Arp, computer code DETECT\_PARTICLES\_2D.M, IEAP, Christian-Albrechts-Universität, D-24098 Kiel, Germany, 2006.
- [149] U. Konopka, computer code SPIT, Max-Planck-Institut für extraterrestrische Physik, D-85741 Garching, Germany, 2005.
- [150] H. Huang, D. Dabiri, and M. Gharib, *Meas. Sci. Technol.* **8**, 1427 (1997).
- [151] Z. M. Zhou, B. Pain, and E. R. Fossum, *IEEE T. Electron Dev.* **44**, 1764 (1997).
- [152] J. P. Boon and S. Yip, *Molecular Hydrodynamics*, 1st ed. (Mcgraw-Hill, New York, 1980).
- [153] C. A. Knapek, A. V. Ivlev, B. A. Klumov, G. E. Morfill, and D. Samsonov, *Phys. Rev. Lett.* **98**, 015001 (2007).